Title
Catalytic materials and systems for chemical and fuel production via electrochemical CO2 reduction in aqueous media

Author
Lum, Yanwei

Publication Date
2018

Peer reviewed|Thesis/dissertation

Catalytic materials and systems for chemical and fuel production via electrochemical CO_2 reduction in aqueous media

By

Yanwei Lum

A dissertation submitted in partial satisfaction of the

Requirements for the degree of

Doctor of Philosophy

in

Engineering – Materials Science and Engineering

in the

Graduate Division

of the

University of California, Berkeley

Committee in charge:

Professor Joel W Ager Co-Chair

Professor Fiona M Doyle Co-Chair

Professor Kristin A. Persson

Professor Bryan D. McCloskey

Spring 2018

Abstract

Design of catalytic materials for commodity chemical and fuel production via electrochemical CO_2 reduction in aqueous media

by

Yanwei Lum

Doctor of Philosophy in Materials Science and Engineering

University of California, Berkeley

Professor Joel W. Ager Co-Chair

Professor Fiona M. Doyle Co-Chair

Electrochemical reduction of CO_2 (CO_2R) to chemical fuels and feedstock via the use of renewable electrical energy is a potential way to mitigate rising atmospheric CO_2 emissions. The ultimate goal of this research field is the ability to develop catalysts capable of converting CO_2 selectively and efficiently into specific products. Of all the possible products from CO_2R, products with 2 or more carbons (C_{2+} products) such as ethylene and oxygenates (e.g. ethanol) are highly desirable as they are already used as fuels in the existing energy infrastructure or as chemical feedstock in industry. Therefore in this thesis, I explore various catalytic materials to facilitate CO_2R to generate these products.

Initially, I was excited by reports in the literature on the use of heteroatom doped carbon materials as catalytic materials. For example, it was claimed that these materials could convert CO_2 selectively to CO, formate or even to methane. These materials typically consist of a carbon structure doped with ~1-5% of heteroatoms such as nitrogen, sulfur, phosphorous or even boron. Synthesis of these materials is simple; they usually involve high temperature annealing of a carbon material (e.g. graphene) with a source containing the heteroatom of choice. However, I discovered that these materials can carry various levels of metallic impurities depending on their preparation method. Therefore, the true catalytic activity of these carbon materials can be obscured by these catalytically active impurities. In Chapter 2, I therefore investigate the role of metallic impurities present in different carbon materials during CO_2R.

Next, I investigated nanostructured catalysts for CO_2R. These catalysts are prepared by electrochemical oxidation and reduction cycling of Cu foil assisted by halide anions in the solution. These halide anions serve to promote the oxidation process of Cu to create Cu_2O and subsequent reduction back to metallic Cu^0 results in a nanostructured surface. These catalysts have been shown to be more selective towards C_{2+} products (especially ethylene) compared to flat, polycrystalline Cu. In Chapter 3, I thus examine the effect of different halide anions on the nanostructuring process and its resultant catalytic activity for CO_2R.

In the literature, oxide-derived Cu catalysts have been shown to be promising catalysts to facilitate the reduction of CO_2 to C_{2+} products. Typically, these catalysts are synthesized by oxidation of Cu to Cu_2O and/or CuO and subsequent reduction back to Cu^0. Also, the cation in the electrolyte used

for CO_2 reduction used in the has been shown to be very important in determining the C_{2+} selectivity of Cu catalysts. In particular, a larger cation such as Cs^+ promotes a higher C_{2+} selectivity compared to K^+. An interesting question is whether oxide-derived Cu catalysts could be combined with Cs^+ to yield very high C_{2+} selectivity. In Chapter 4, I prepare oxide-derived catalysts via 4 different means according to previous reports and I study their catalytic activity for CO_2R in aqueous electrolyte containing either K^+ or Cs^+. I show that a very high faradaic efficiency for formation of C_{2+} products (~70%) can be achieved by optimizing the roughness factor of these catalysts with Cs^+ containing electrolyte.

It has been proposed by various researchers that oxides in oxide-derived Cu catalysts are stable despite the highly reducing conditions applied during CO_2 reduction. Therefore, a large amount of residual oxides remain in the catalyst and these have been proposed to be the reason for high C_{2+} selectivity for oxide-derived Cu catalysts. In chapter 5, I investigated whether oxides are truly stable during CO_2 reduction. I fabricated ^{18}O labeled catalysts and used secondary ion mass spectrometry to determine the ^{18}O content before and after CO_2 reduction. I found that <1% of the original ^{18}O content remains after CO_2 reduction, showing that residual oxides are unstable, as thermodynamically predicted.

The previous chapters all describe catalysts which have ill-defined structures. I therefore sought to obtain greater control over the dimensions and composition of my catalysts and I turned to photolithography to fabricate model catalysts. In Chapter 6, I describe a device which I named the "AuCu device" to investigate a process termed as "CO crossover" in CO_2R. CO spillover occurs when a CO producing catalyst produces CO from CO_2 and this can then crossover onto Cu sites. This result in an increased production of C_{2+} oxygenates at the expense of ethylene. The AuCu device which I fabricated consists of interdigitated lines of Au and Cu on an insulating SiO_2 substrate. In this device, Au serves to produce CO and the Cu serves to reduce this CO as well as externally supplied CO_2 to further reduced products. The lines are designed to be electronically isolated and as such can be independently actuated. Such a system is therefore ideal to study the CO crossover effect.

Additionally, in chapter 6, I describe another catalyst system, which was also fabricated via photolithography. This system, consisting of Cu dots or lines patterned onto a Ag substrate is designed to take full advantage of the CO crossover effect to achieve a high selectivity to oxygenates. Exposed Ag sites serve to produce CO and thus by varying the areal coverage of Cu dots/lines, systematic control of CO spillover can be exercised. This allows me to tune the ratio of oxygenates to ethylene from 0.59 to 2.39. In the best system, an oxygenate selectivity of >40% can be achieved.

In conclusion, I investigated a variety of catalyst systems for CO_2R for my graduate studies. My thoughts and future outlook are summarized in Chapter 7. I outline the main challenges in this field and my thoughts on how selectivity and catalyst activity might be improved. I also emphasize the importance of efforts to understand the mechanism of CO_2 reduction.

This dissertation is dedicated to my grandmother, who passed away in July 2014

Table of Contents

Acknowledgements

Firstly, I would like to express my sincere gratitude to my advisor, Professor Joel W. Ager for the opportunity to work at the Joint Center for Artificial Photosynthesis (JCAP) for my PhD work. Joel has been an amazing and incredibly supportive advisor who was always around to provide a listening ear and wise counsel. Words cannot describe how invaluable his presence has been for my PhD career, without whom I might never have become the scientist I am today. His cheerful and carefree way of looking after his group members will definitely serve as a model for me in the future should I have a research group of my own.

Next, I would like to thank Professor Fiona M. Doyle who took me in during my first year as a PhD student and has provided valuable advice throughout. I particularly remember the time when I was preparing for my Qualifying Examinations and she went through my presentation slide by slide until they were in an "acceptable" condition. This was in spite of her demanding schedule as Dean of the Graduate Division.

Thanks must also be given to Professor William A. Goddard III and his postdoc Tao Cheng from Caltech. Our weekly online video meetings were stimulating and highly collaborative.

Professor Alexis T. Bell has also given me much valuable insights during our weekly CO_2 reduction meetings. I have learnt much about the world of catalysis from this very experienced and knowledgeable scientist.

I was incredibly lucky to serve as a GSI for Professor Mark D. Asta for Phase transformations, a subject that I loved very much as an undergraduate. His passion and dedication he has for educating the next generation of material scientists is admirable and I hope I will be to emulate at least a fraction of him, should I ever have the privilege of being in a similar position in the future.

My research might not have been possible if not for the fellow graduate students and post docs throughout my various stages of my PhD at JCAP. I am especially grateful to Peter Lobaccaro and Youngkook Kwon who were essentially my mentors during the early stages of my PhD. I would also like to thank Ezra Clark, Meenesh Singh, Le Chen, Wenjun Liu and Gurudayal for their valuable insights and discussions in understanding the world of electrochemical CO_2 reduction. I would also like to thank Mark Hettick and Kevin Chen (EMAT) for their assistance and advice on research matters. Gratitude must also be given to Professor Mark D. Asta, Professor Kristin A. Persson and Professor Bryan D. McCloskey for taking the time to serve on my Qualifying Examination Committee.

My friends here have been a good source of distraction from research and I would like to thank them for being part of my life at Berkeley. Shuren Lin, Mika Tei, Zhi Wei Tay, Shaun Lim, Han Ee Ong, Wei Cheng Ng, Kyle Tom, Edy Cardona, Iqbal Utama and Hnin Yin Nyein Nyein.

Much gratitude must be given to my funding agency – A*STAR in Singapore for their financial support of my undergraduate and graduate education. The opportunity to be educated abroad has opened my doors for me indeed. I will definitely do my best to contribute back to Singapore in whatever way I can.

Most importantly, I would like to thank my family and my fiancée, Wan Ru. My parents have supported my unwaveringly throughout my life, without whom I might have never decided to

embark on a research career in the first place. They must have had a hard time bringing me and my brother up given our playful personalities. Thanks must be given to my brother Yansheng, who has never forgotten to take my share of the red packets during Chinese New Year. My fiancée Wan Ru has been very supportive of me during my PhD career, to which I have been most grateful.

Finally, I also want to mention my grandmother who unfortunately passed away during the first year of my PhD. I am at least glad that I was able to return to Singapore to see her during the last moments of her life.

Chapter 1: Introduction

1.1 Motivation

The past few decades have seen global CO_2 levels rising at alarming rates. This has been a result of human activities such as the burning of fossil fuels to feed our energy hungry society. In September 2016, the global CO_2 concentration officially exceeded the symbolic 400 ppm mark and has been predicted to rise even further in years to come. Increasing emission of CO_2 has led to a steady rise in global temperatures due to a phenomenon known as the greenhouse effect. When the earth is heated up by the sun, the heat energy can be dissipated by emission of infrared radiation. However greenhouse gases, of which CO_2 is the main culprit, have to ability to trap infrared radiation, which impedes the earth from cooling down.

In the foreseeable near future, there is no feasible way of weaning mankind entirely off fossil fuels. Part of the reason for this is that fossil fuels are comparatively low cost and practically, these fuels have one of the highest energy densities. Efforts are underway to harness our sources of renewable energy such as solar, wind and hydrothermal. Solar energy in particular is very attractive because energy from the sun is nearly limitless. As a comparison, the sun provides the earth almost 23,000 TWy per year, while world energy consumption is around 16 TWy per year (Figure 1.1).

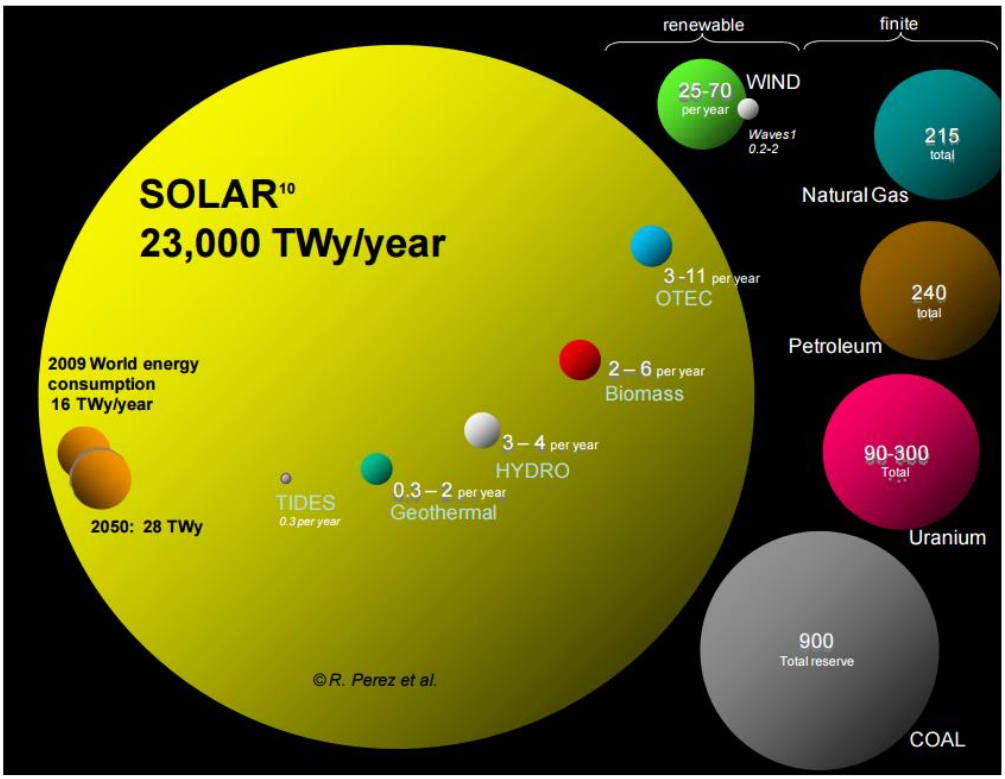

Figure 1.1: Energy (TWy) from various renewable resources as well as known energy reserves of our planet. Image is adapted from Perez et al[1].

A promising strategy to both secure the energy future of mankind as well as mitigate rising CO_2 emissions is electrochemical CO_2 reduction (CO_2R). In this process, CO_2 can be converted electrochemically into useful fuels and/or commodity chemicals powered by electricity from renewable sources such as solar energy harvested using photovoltaic systems. Development of this technology is also attractive because renewable energy, which is often intermittent, can be stored in the form of chemical fuels which are already employed in our existing energy infrastructure (e.g. ethanol). Figure 1.2 shows a schematic of how CO_2R could be employed in the future. Such a scheme is effectively carbon neutral as CO_2 is continuously recycled in a loop.

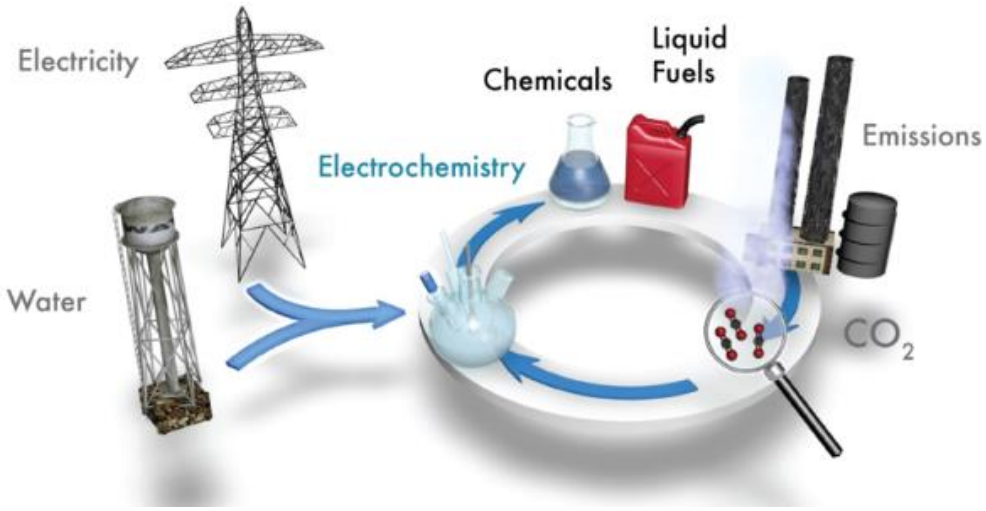

Figure 1.2: Schematic of how CO_2R will recycle CO_2 emissions into useful commodity chemicals and liquid fuels using renewable electricity. Such a process helps mitigate CO_2 emissions and allows us to store renewable energy in forms that are already used in our current energy infrastructure. Image is adapted from Jaramillo and co-workers[2].

1.2 Fundamentals and challenges of CO_2R

Much of the pioneering work of CO_2R was carried out by Hori and co-workers from Chiba University in Japan. He was the first to demonstrate the use of metallic copper as a cathode for facilitating the electrochemical reduction of carbon dioxide to hydrocarbons and oxygenates[3]. Since then, much progress has been made in this field and this section attempts to summarize the fundamentals as well as the grand challenges of this field.

1.2.1 Survey of catalysts for CO_2R

The grand challenge of this field is the ability to design and create catalysts which are both efficient and selective for CO_2R. This means that catalysts should facilitate CO_2R at low overpotentials with high activity. Furthermore as we will go over in more detail later, CO_2R can result in a wide range of different products generated and it is therefore important to design catalysts that are selective to one product, for ease of separation. So far, a wide range of metallic catalysts have been tested for CO_2R and Figure 1.3 summarizes some of these results.

	Electrode	Potential vs. SHE V	Current density mA cm^{-2}	Faradaic efficiency, %							
				CH_4	C_2H_4	EtOH[a]	PrOH[b]	CO	$HCOO^-$	H_2	Total
I	Pb	−1.63	5.0	0.0	0.0	0.0	0.0	0.0	97.4	5.0	102.4
	Hg	−1.51	0.5	0.0	0.0	0.0	0.0	0.0	99.5	0.0	99.5
	Tl	−1.60	5.0	0.0	0.0	0.0	0.0	0.0	95.1	6.2	101.3
	In	−1.55	5.0	0.0	0.0	0.0	0.0	2.1	94.9	3.3	100.3
	Sn	−1.48	5.0	0.0	0.0	0.0	0.0	7.1	88.4	4.6	100.1
	Cd	−1.63	5.0	1.3	0.0	0.0	0.0	13.9	78.4	9.4	103.0
	Bi[c]	−1.56	1.2	-	-	-	-	-	77	-	-
II	Au	−1.14	5.0	0.0	0.0	0.0	0.0	87.1	0.7	10.2	98.0
	Ag	−1.37	5.0	0.0	0.0	0.0	0.0	81.5	0.8	12.4	94.6
	Zn	−1.54	5.0	0.0	0.0	0.0	0.0	79.4	6.1	9.9	95.4
	Pd	−1.20	5.0	2.9	0.0	0.0	0.0	28.3	2.8	26.2	60.2
	Ga	−1.24	5.0	0.0	0.0	0.0	0.0	23.2	0.0	79.0	102.0
III	Ni	−1.48	5.0	1.8	0.1	0.0	0.0	0.0	1.4	88.9	92.4[e]
	Fe	−0.91	5.0	0.0	0.0	0.0	0.0	0.0	0.0	94.8	94.8
	Pt	−1.07	5.0	0.0	0.0	0.0	0.0	0.0	0.1	95.7	95.8
	Ti	−1.60	5.0	0.0	0.0	0.0	0.0	tr.	0.0	99.7	99.7
IV	Cu	−1.44	5.0	33.3	25.5	5.7	3.0	1.3	9.4	20.5	103.5[d]

Table 1.1 Faradaic efficiencies for formation of various products using various metallic electrodes for CO_2R. All electrolytes used were 0.1 M $KHCO_3$. Metals are grouped according to the products they predominantly make. Image is adapted from Hori et al[4].

Based on Table 1.1, there are essentially 4 groups that metallic electrodes can be classified under according to the products they predominantly make by reduction of CO_2. Group I consists of metals such as Pb and Sn that make formate, Group II consists of metals such as Au and Ag that make CO and Group III consists of metals that have little interaction with CO_2 and therefore only generate hydrogen via water reduction. Group IV has only has one member, which is Cu and is the most interesting due to its unique ability to directly generate a significant amount of hydrocarbons and oxygenates from CO_2. Equations presenting some of the possible electrochemical reactions for CO_2R are shown below.

$$CO_2 + H_2O + 2e^- = HCOO^- + OH^- \quad \text{(eqn 1.1)}$$
$$CO_2 + H_2O + 2e^- = CO + 2OH^- \quad \text{(eqn 1.2)}$$
$$CO_2 + 6H_2O + 8e^- = CH_4 + 8OH^- \quad \text{(eqn 1.3)}$$
$$2CO_2 + 8H_2O + 12e^- = C_2H_4 + 12OH^- \quad \text{(eqn 1.4)}$$
$$2CO_2 + 9H_2O + 12e^- = C_2H_5OH + OH^- \quad \text{(eqn 1.5)}$$

1.2.2 Electrochemical equilibria in electrolyte

Typically, an aqueous bicarbonate buffer solution is employed to study CO_2R. When the solution is saturated with CO_2, a chemical equilibrium between 3 species namely aqueous dissolved CO_2, HCO_3^- and CO_3^{2-} is formed[4].

$$CO_2\,(aq) + H_2O\,(l) = HCO_3^-\,(aq) + H^+\,(aq) \quad \text{(eqn 1.6)}$$
$$pH = pK_{a1} + \log[HCO_3^-] - \log[CO_2],\ pK_{a1} = 6.35 \quad \text{(eqn 1.7)}$$

$$HCO_3^- (aq) = CO_3^{2-} (aq) + H^+ (aq) \quad \text{(eqn 1.8)}$$

$$pH = pK_{a2} + \log \{[CO_3^{2-}]/[HCO_3^-]\},\ pK_{a2} = 10.33 \quad \text{(eqn 1.9)}$$

These equilibria ensure that the pH of a buffer solution is fixed by the concentration of the salt used. For example, a CO_2 saturated 0.1 M $KHCO_3$ solution should have a pH of 6.8.

When CO_2R is performed on an electrode, water molecules are consumed and OH^- is generated at the electrode (equations 1.1 to 1.5). The OH^- is then neutralized by bicarbonate anions:

$$OH^- (aq) + HCO_3^- (aq) = CO_3^{2-} (aq) + H_2O (l) \quad \text{(eqn 1.10)}$$

Therefore for CO_2R, we might predict that performing this reaction at a high rate might lead to severe depletion of dissolved CO_2 because conversion of bicarbonate to carbonate results in driving equation 6 towards the forward reaction. This would mean that CO_2R would be severely limited by mass transport of CO_2. In reality however, the conversion of dissolved CO_2 to bicarbonate is slow which causes the pH at the surface of the electrode to rapidly rise above the bulk pH. The CO_2 concentration at the surface is therefore higher than equilibrium, which helps sustain CO_2R[4]. However if an extremely high current density is applied, severe depletion of CO_2 will occur which will lead to loss of selectivity towards product formation and increased hydrogen evolution.

1.2.3 A look at CO producing catalysts for CO_2R (Au/Ag/Zn)

Metals classified under Group II in Figure 1.3 produce predominantly CO during CO_2R, according to equation (2). Among these metals, Au/Ag/Zn are particularly active for converting CO_2 to CO. Jaramillo and co-workers studied a series of transition metals including these 3 metals for CO_2R and the results are summarized in Figure 1.4.

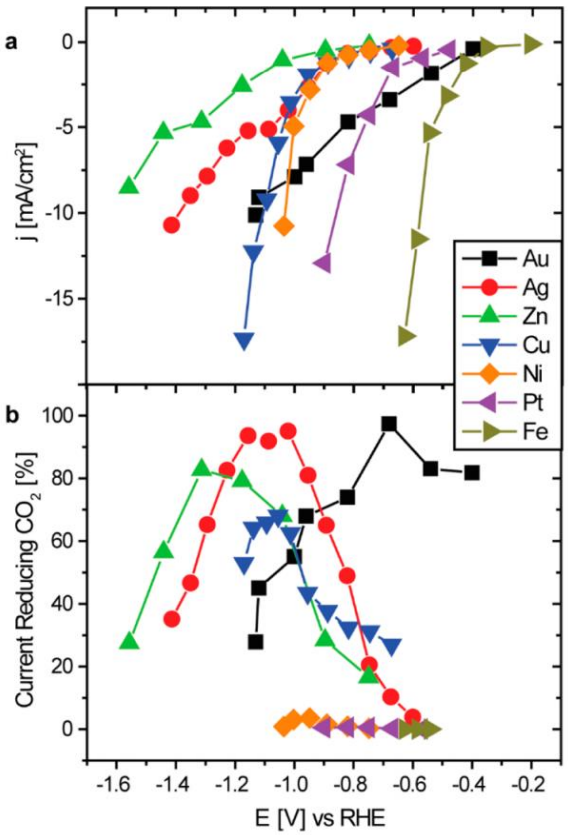

Figure 1.3 (a) Total current density and (b) percentage of current reducing CO_2 for different transition metals. Image is adapted from Jaramillo and co-workers[2].

As seen from Figure 1.4, gold produces CO with the lowest overpotential requirements, reaching >90% faradaic efficiency at ~0.65 V vs RHE, with a current density of ~4 mA cm^{-2}. Ag reaches >90% faradaic efficiency at ~-1.0 V vs RHE at a current density of ~-4 mA cm^{-2}. Finally, Zn requires the highest overpotential for CO production, requiring ~-1.3V vs RHE to reach >90% faradaic efficiency at a current density of ~-4 mA cm^{-2}. A reaction schematic proposed by Smith and co-workers is shown in Figure 1.5 below[5].

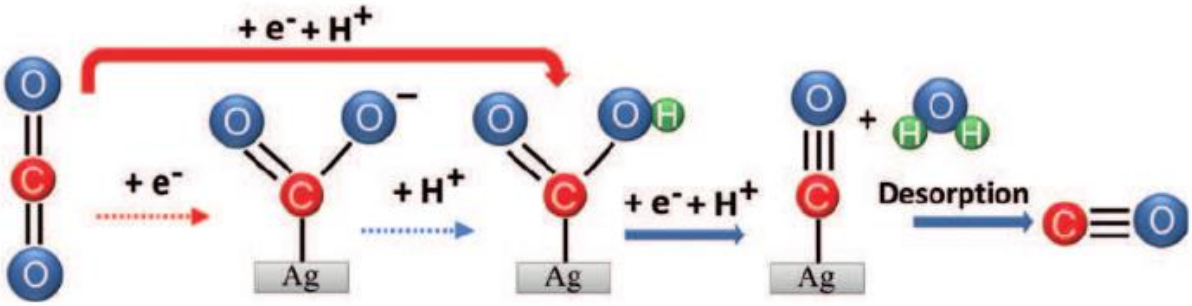

Figure 1.4 Reaction pathways for the reduction of CO_2 to CO on Ag. Image is adapted from Smith and co-workers[5].

In this schematic, the first electron transfer is proton decoupled and the electron transfer step occurs before the proton transfer. The final step is a proton coupled electron transfer, producing CO which then desorbs from the surface since the CO binding energy on silver is weak. In particular for Au/Ag/Zn which produces predominantly CO, it is known that CO binds weakly on these surfaces[2] and therefore desorption is facile, generating CO(g).

1.2.4 A closer look at Cu catalysts for CO_2R

As mentioned in section 1.2.1, Cu is unique in its ability to generate a significant amount of hydrocarbons and oxygenates from CO_2 (~70%). It is therefore the most intensely studied catalyst in the field of CO_2R. Jaramillo and co-workers performed an in-depth study of polycrystalline Cu, benchmarking the products across a broad range of applied potentials, measuring all possible gas products via gas chromatography and liquid products via highly sensitive NMR techniques[6]. This was a significant contribution to the field as they identified a total of 16 different products, significantly more than any previous study allowing for new insights into possible CO_2 reaction pathways and mechanisms. Figure 1.6 presents all 16 possible CO_2R products generated by Cu that were detected.

Product	# e⁻	E	Product	# e⁻	E
Formate	2	−0.02	Acetaldehyde	10	0.05
Carbon monoxide	2	−0.10	Ethanol	12	0.09
Methanol	6	0.03	Ethylene	12	0.08
Glyoxal	6	−0.16	Hydroxyacetone	14	0.46
Methane	8	0.17	Acetone	16	−0.14
Acetate	8	−0.26	Allyl alcohol	16	0.11
Glycolaldehyde	8	−0.03	Propionaldehyde	16	0.14
Ethylene glycol	10	0.20	1-Propanol	18	0.21

Figure 1.5 All 16 possible products from CO_2R on Cu, together with the number of electrons as well as the standard reduction potential vs RHE at pH 6.8. Image is adapted from Jaramillo and co-workers[6].

Careful experiments were carried out at each potential and the faradaic efficiencies for formation of all products are summarized in Figure 1.7.

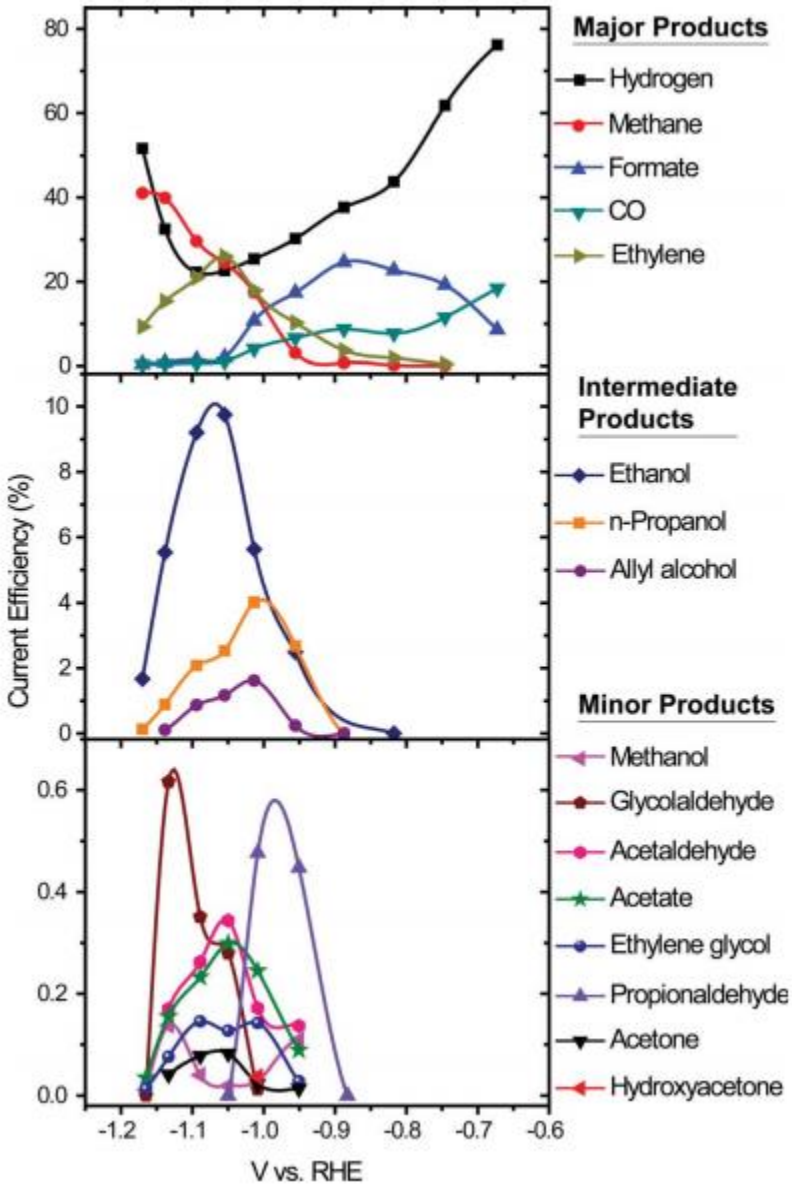

Figure 1.6 Faradaic efficiencies as a function of potential for all 16 possible products formed by Cu during CO_2R. Products are grouped according to major, intermediate and minor for convenience. Image is adapted from Jaramillo and co-workers[6].

As seen from the data presented, reaction pathways for CO_2R on Cu are complex indeed since 16 different products can be formed, most requiring multi-step electron transfers. Reaction pathways for the major products have been proposed. Figure 1.8 below shows reaction pathways for the major products as proposed by Koper and co-workers on Cu for CO_2R[7].

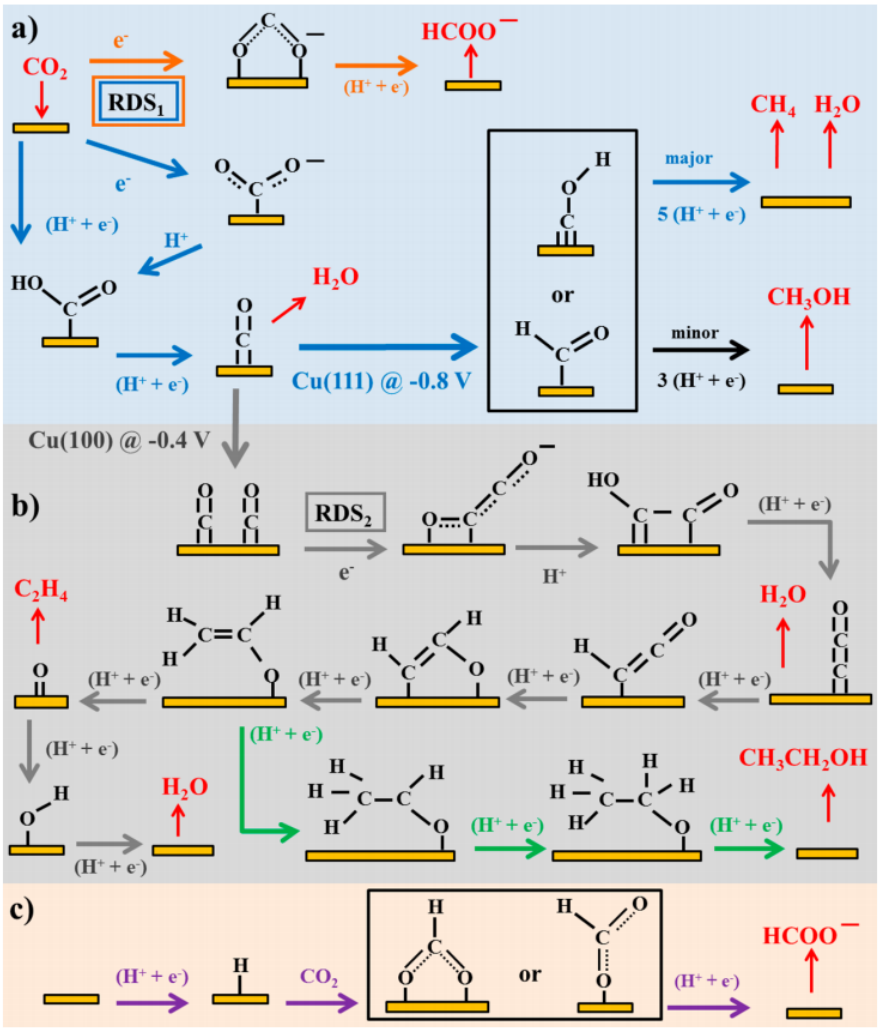

Figure 1.7 Proposed reaction pathways for CO_2R on Cu for the major products, which include: formate, CO, methane, ethylene and ethanol. Image is adapted from Koper and co-workers[7].

As seen from Figure 1.8, Cu is similar to the CO producing metals (Au/Ag/Zn) in that it is able to produce CO from CO_2. In this case however, Cu is unique in that it has a slightly stronger CO binding energy, which enables it to further reduce CO. CO can be protonated to form either *COH or *CHO, which can then lead to either methane or methanol (minor product). CO can also go down a dimerization pathway leading to C_2 products, of which ethylene and ethanol are the observed major products.

Based on copper's unique ability to generate a large number of valuable commodity chemicals and fuels, it is clear why there is such a significant interest in studying and optimizing it. The main problems with copper based catalysts are that large overpotentials (~1 V) are required to drive CO_2R at appreciable rates and with high selectivity to hydrocarbons and oxygenates. Selectivity is also an issue as copper does not show high selectivity towards any particular product and usually

generates a mix of hydrocarbons and oxygenates. Therefore, this dissertation attempts to provide some answers to these 2 grand challenges in the CO_2 reduction field.

1.3 Dissertation outline

In Chapter 2, carbon based catalysts will be examined for CO_2 reduction and it was found that trace amounts of impurities in these materials can dominate their catalytic activity. Chapter 3 discusses the nanostructuring process of copper via halide assisted electrochemical oxidation and reduction processes and its effects on CO_2R activity. For cchapter 4, the various oxide-derived copper catalysts are investigated and optimized for producing C_{2+} products. In chapter 5, experiments are done to understand the true stability of residual oxides in oxide-derived Cu catalysts. In chapter 6, a novel interdigitated electrochemical device consisting of alternating Au and Cu lines was developed to utilize "CO crossover" to enable higher selectivity towards oxygenates compared to hydrocarbons. Finally, chapter 7 deals with the future outlook of the field. In particular, I discuss my thoughts on the main challenges in the field and how they may be addressed.

Chapter 2: Carbon-based materials as catalysts for CO_2R

2.1 Introduction

Carbon-based materials are attractive candidates for use as catalysts for electrochemical reactions. Typically these carbon materials are doped with heteroatoms which include but are not limited to nitrogen, sulfur, phosphorous and boron. Introduction of nitrogen into the carbon structure for example, has been proposed to result in a positive charge on an adjacent carbon atom, which is the active site for catalysis. For example, there are numerous reports on the use of these doped materials to catalyze hydrogen evolution (HER), oxygen evolution (OER) and oxygen reduction (ORR). Recently, this has been extended to CO_2R and several reports have been published describing this.

Meyer and co-workers developed nitrogen-doped carbon nanotubes which were able to exhibit 87% selectivity for formation of formate at -1.8 V vs SCE. Nitrogen doping was achieved via ammonia plasma and subsequently, a polyethylenimine overlayer was added to function as a co-catalyst. Strasser and co-workers developed metal-doped nitrogenated carbons which exhibited increased CO selectivity and partial current density compared to polycrystalline Au at low overpotentials. Further, it was found that certain combinations of metal dopants resulted in methane formation from CO_2 due to the synergistic effects of the carbon structure and the nitrogen/metal dopants. Very recently, Ajayan and co-workers synthesized nanometre-size N-doped graphene quantum dots, which showed very comparable selectivity and activity towards the formation of C_2 and C_3 products compared to copper nanoparticle catalysts.

Inspired by these promising reports, I attempted to perform heteroatom doping of sulfur and nitrogen into a graphene structure as a catalyst for CO_2R. Preliminary tests showed that this catalyst was able to generate methane from CO_2. However, when testing the starting material (undoped graphene), methane formation was observed as well.

Intrigued by this, a literature search revealed that there have been reports which show that these carbon materials can possess large amounts of metallic impurities that can dominate their electrocatalytic activities. For example, carbon nanotubes are often grown with Fe/Ni catalyst precursors. Fe/Ni particles can therefore reside within these carbon nanotubes and contribute significantly towards their observed electrocatalytic activities. I therefore sought to characterize and quantify the various metallic impurities present in different carbon materials and determine their effects on their electrocatalytic activity for CO_2R.

2.2 Nitrogen and sulfur co-doped graphene for CO_2R

Nitrogen and sulfur co-doped carbon materials have been shown to be interesting catalysts for the oxygen reduction reaction due to synergistic effects of the nitrogen/sulfur dopants with the carbon structure. Here I synthesized nitrogen and sulfur co-doped graphene (NSG) and investigated its electrocatalytic activity for CO_2R.

2.2.1 Experimental

Materials

Graphene oxide (sheets) was purchased from ACS Material, LLC. Sodium carbonate (≥99.9999% metals basis), Nafion® solution (10 wt.% dispersion in water) and ethanol (absolute ≥99.5%) were purchased from Sigma Aldrich. Glassy carbon plate (type 2, 2 mm thick) was purchased from Alfa Aesar. Water-based Alumina fine polishing suspension (0.05 μm) and polishing cloth (Alpha-A, 8") were purchased from Ted Pella, Inc. Carbon dioxide (99.995%), nitrogen (99.999%), helium (99.999%) and hydrogen (99.999%) were purchased from Praxair. Hydrogen, helium, nitrogen, carbon dioxide gas purifiers were purchased from Valco Instruments Co. Inc. All chemicals were used without further purification. Electrolyte solutions were prepared with 18.2 MΩ deionized water from a Millipore system.

Synthesis of nitrogen sulfur co-doped graphene (NSG)

Synthesis of NSG was performed according to the procedure by Wang and co-workers. Briefly, 200 mg of graphene oxide and 1600 mg and thiourea were dispersed in ethanol and sonicated for 1 hour for homogeneity. The ethanol was then removed via rotary evaporation and the residue was then annealed at 800 °C for 2 hours in N_2 atmosphere in a tube furnace. The furnace was then left to cool to room temperature before removing the sample.

Electrochemical testing

Electrochemical measurements were carried out using a Biologic SP-300 potentiostat. Ambient pressure CO_2 electrolysis was carried out in a custom-made gas-tight electrochemical cell made of polycarbonate and fitted with Buna-N o-rings. The configuration of the electrochemical cell is such that the working electrode sits parallel with respect to the counter electrode (platinum foil) to ensure a uniform potential distribution across the surface. The geometric surface area for both of the electrodes is 1 cm^2. A Selemion AMV anion exchange membrane was used to separate the anodic and cathodic compartments. Each of the compartments in this cell contains a small volume of electrolyte (0.5 ml each) to concentrate liquid products and therefore increase detection limits. The headspace of the cathodic compartment was approximately 0.3 ml.

Before conducting CO_2 electrolysis, the electrolyte in the cathodic compartments was purged with CO_2 for at least 15 min. During electrolysis, CO_2 was constantly bubbled through the electrolyte at a flow rate of 5 sccm to prevent depletion of CO_2 in the electrolyte and to allow continuous analysis of gaseous products via a gas chromatograph. The flow rate of CO_2 was controlled with a mass flow controller (Alicat Scientific) and the gas was first humidified with water by passing it through a bubbler to minimize evaporation of electrolyte. For all experiments, platinum foil was used as the counter electrode and Ag/AgCl electrode (leak free series) from Innovative Instruments, Inc was used as the reference. Data was converted to the RHE reference scale using the equation:

$$E\ (vs.\mathrm{RHE}) = E\ (vs.\mathrm{Ag/AgCl}) + 0.197\,V + 0.591\,pH,$$

where the pH was 6.8. To ensure the accuracy of the reference electrodes, calibration was done with a homemade reversible hydrogen electrode.

Product analysis

For gas product analysis, a gas chromatograph (SRI instruments) equipped with a packed HaySep D column and a packed MolSieve 5A column was used. For detection of gas products, a flame

ionization detector (FID) with a methanizer was used to detect hydrocarbons (CO, CH_4, C_2H_4 and C_2H_6) with helium as the carrier gas. A thermal conductivity detector (TCD) was used to detect hydrogen with nitrogen as the carrier gas. Calibration of the gas chromatograph was done using calibration gas from Praxair (UN 1956) with 0.1% CO, 0.099% ethane, 0.099% ethylene, 0.1% hydrogen, 0.1% ethane balanced in helium. Additional calibration points were achieved by dilution of the calibration gas with appropriate flow rates of helium gas. To further calibrate the hydrogen peak, calibration gas from Praxair (UN 1956) containing 500 ppm of hydrogen and balance as nitrogen was used. After passing through the cell, the CO_2 was allowed to flow directly into the gas sampling loop of the GC for online gaseous product analysis, which was carried out every 30 minutes. For all experiments, electrolysis was allowed to proceed for 2 hours with gas analysis done at the 25, 55, 85 and 115 minutes.

The liquid products were collected from the cathode and anode chambers after electrolysis and analyzed by High-Performance Liquid Chromatography (HPLC) on UltiMate 3000 from Thermo Scientific. Vials with the collected samples were placed in an autosampler holder and 10 µL of sample was injected into the column. The column used was an Aminex HPX 87-H (Bio-Rad) and diluted sulfuric acid (1 mM) was used as the eluent. The temperature of the column was maintained at 60 °C in a column oven, and the separated compounds were detected with a refractive index detector (RID). The expected products of CO_2R were analyzed as well by HPLC to produce a standard calibration curve at 60°C (i.e. formate, acetate, ethylene glycol, ethanol, and n-propanol).

Sample preparation

1 mg of NSG was first dispersed into 1 ml of ethanol and sonicated for 30 mins for homogeneity. 5 µl of Nafion solution was added to this mixture and further sonicated for 10 minutes. Glassy carbon plates were prepared by soaking in 1.0 M HNO_3 solution for 10 minutes followed by polishing with water-based alumina fine polishing suspension. The NSG mixture was then casted onto a glassy carbon plate using a spin coater at 1000 rpm. This was then used as the working electrode for bulk CO_2 reduction electrolysis.

2.2.2 Results and Discussion

Faradaic Efficiency plots

In CO_2 reduction literature, data is commonly reported in the form of faradaic efficiency plots. This represents the fraction of total charge passed during bulk electrolysis responsible for the production of each particular product. For example, if 1 out of 10 electrons passed through the electrochemical system went to generating methane, then the faradaic efficiency towards methane would be 10%. Figure 2.1 below shows the faradaic efficiency plot obtained when NSG was tested for CO_2 reduction at a potential of -1.3V vs RHE.

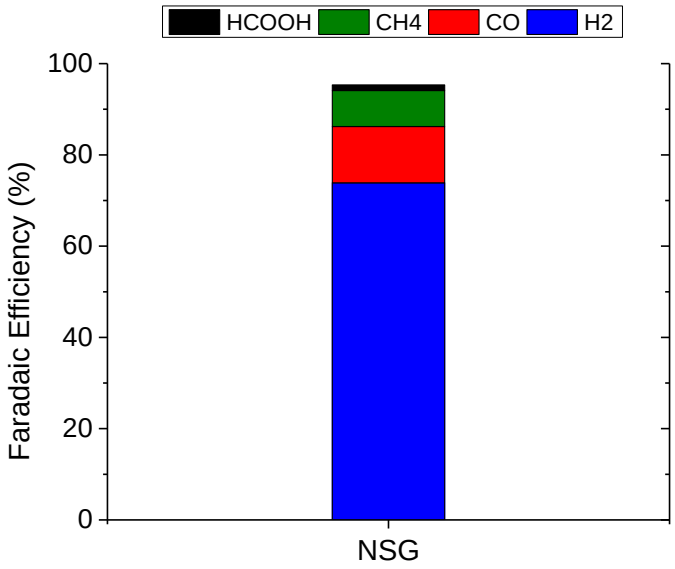

Figure 2.1 Faradaic efficiency plot for CO_2 reduction with NSG at -1.3V vs RHE in 0.1M $NaHCO_3$. Products observed at hydrogen, carbon monoxide, methane and formate.

Under the testing conditions, NSG was able to produce predominantly hydrogen. Intriguingly, some of the current passed went to methane, carbon monoxide and formate as well. If the results were true, it would be interesting because this would be one of the first few demonstrations of a metal free and copper free catalyst for CO_2 reduction capable of producing some amount of hydrocarbons (methane).

2.3 Effect of metallic impurities in carbon materials in CO_2R

2.3.1 Introduction

In order to properly ascribe the CO_2 reduction activity of NSG to the nitrogen and sulfur dopants, it is necessary to perform a few critical control experiments. Firstly, the undoped material (no sulfur and nitrogen) would have to be tested. Secondly the concentration of metallic impurities in the undoped material would have to be determined as well to ensure that the system is truly 'metal-free'. Here, we present a comprehensive study of the analysis of the concentration of metallic impurities in carbon materials and its effects on CO_2R. We test graphene oxide, carbon nanotubes as well as graphite materials. Also, the effect of having trace amounts of Cu contaminants in the electrolyte is investigated as well.

It is notable that several investigators have found carbon-based materials to be active for the CO_2R even in the absence of added metal. For example, Kumar *et al*. have reported that nitrogen doped carbon nanofibers produce CO with high selectivity at an overpotential of 0.17 V,[8] and Nakata *et al.* have noted that boron-doped diamond electrocatalysts produce formaldehyde with a Faradaic efficiency of up to 74% .[9] Very recently, Zhang *et al*.[10] and Wu *et al*.[11] have reported that nitrogen-

doped carbon nanotubes can produce formic acid and CO, respectively, with Faradaic efficiencies of over 80%. These reports are surprising since metal-free carbon materials would be expected to have little activity for the electrocatalytic reduction of CO_2.[8,10,12] Therefore, the question arises as to whether or not the carbon-based materials used in these studies contain metal impurities. This issue becomes all the more pertinent in the light of recent work showing that trace metal impurities present on carbon supports can substantially influence their electrochemical activity.[13] For example, it has been shown that much of the apparent activity of carbon nanotubes for hydrazine oxidation is actually due to metal impurities.[14] Moreover, the metal impurities can persist in carbon nanotubes despite efforts to remove them via dissolution in strong acid and rinsing.[15,16] While in the case of nanotubes, it could be thought that the metal contaminants are on the interior of the tubes, graphene supports have also been reported to have detectable levels of metal contaminants.[17–19] Notably, it has been found that copper is a major impurity of graphene oxide materials.[17,19] Consequently, it becomes important to understand the role that impurities such as Fe, Ni, and Cu might have on the activity of carbon supports for the CO_2R, a subject which to the best our knowledge has not been previously investigated.

2.3.2 Experimental

Materials

Graphene oxide (sheets), sodium carbonate (≥99.9999% metals basis), potassium chloride (99.999% metals basis), Cu acetylacetonate (99.99%), oleylamine (70%), nafion® solution (10 wt.% dispersion in water) and ethanol (absolute ≥99.5%) were purchased from Sigma Aldrich. Graphene oxide was also purchased from ACS Materials LLC and Graphene Supermarket. Reduced graphene oxide was purchased from Sigma Aldrich. Potassium ferricyanide (≥99%) was purchased from Fisher Chemical. Glassy carbon plate (type 2, 2 mm thick), glassy carbon rod (type 2, 5 mm diameter), graphite powder (≥99.9999% metals basis) and Cu (II) sulfate hydrate (≥99.999% metals basis) were purchased from Alfa Aesar. Multi-walled carbon nanotubes (20-30 nm diameter, 0.5-2 μm length, >95% purity) were purchased from Nanostructured & Amorphous Materials, Inc. P-type silicon (boron-doped) was purchased from Silicon Quest International. Water-based Alumina fine polishing suspension (0.05 μm) and polishing cloth (Alpha-A, 8") were purchased from Ted Pella, Inc. ACS reagent grade nitric acid was purchased from EMD millipore. High purity nitric acid (Aristar® Ultra) was purchased from BDH chemicals. Carbon dioxide (99.995%), nitrogen (99.999%), helium (99.999%) and hydrogen (99.999%) were purchased from Praxair. Hydrogen, helium, nitrogen, carbon dioxide gas purifiers were purchased from Valco Instruments Co. Inc. All chemicals were used without further purification. Electrolyte solutions were prepared with 18.2 MΩ deionized water from a Millipore system.

Preparation of Cu nanoparticles

Cu nanoparticles were synthesized by the thermal decomposition of Cu acetylacetonate ($Cu(acac)_2$) in oleylamine following Uk Son *et al.*[20] In brief, 10 mL of oleylamine was heated to 130°C in a 50 mL three neck flask equipped with a condenser and stirrer bar under nitrogen for 30 minutes and then cooled to room temperature. Next, 100 mg of $Cu(acac)_2$ was added to the oleylamine. The solution was slowly heated to 230°C and kept at this temperature for 6 hours, producing a red-

coloured colloidal solution. After cooling to room temperature, the colloidal solution was transferred to a mixture of toluene and ethanol, after which the colour of the solution changed to green, indicating that Cu nanoparticles were oxidized to Cu oxide. Cu nanoparticles were collected by centrifuging at 8000 rpm for 20 min and decanting the solvent. The nanoparticles were then resuspended in toluene and ethanol and recollected by centrifuging and finally dried under vacuum overnight.

Nitric acid washing procedure

For this procedure, 10 ml of concentrated nitric acid was added to a small amount of each of the carbon materials (~20 mg) in a centrifuge tube. To ensure sufficient dispersion of the materials, the mixture was shaken vigorously and then sonicated for 3 hours. The resulting dispersion was then filtered and the filtrate was collected for inductively coupled plasma mass spectrometry (ICP-MS) analysis. The carbon materials left behind as residue were then rinsed briefly with more acid and finally with deionized water until the pH of the filtrate became neutral. The carbon materials were then dried under vacuum overnight. The same procedure was used for both washing with ACS grade and high purity nitric acid.

ICP-MS analysis

For ICP-MS analysis, samples were first diluted with 2% ultrapure nitric acid and then analyzed on an Elan DRC II ICP-MS (Perkin Elmer) with a PFA nebulizer and spray chamber at 1500 W RF power. Generally, the most abundant isotopes of analytes were chosen during analysis. In addition, ammonia and oxygen were used as reaction gases to remove interferences for Cr and Fe analysis. Elements that were evaluated include Mn, Fe, Ni, Cu, Cr, Co, Ag, Cd and Pb.

Materials characterization

The morphology of the carbon materials coated on glassy carbon before and after Cu deposition was characterized using a FEI Quanta 200 FEG SEM.

Electrode preparation

The glassy carbon plate was first cut into 2.2 cm by 2.2 cm dimensions and cleaned by sonicating in acetone, followed by isopropanol and finally with deionized water. The glassy carbon plate was then mechanically polished using an alumina suspension up to 0.05 µm on polishing cloth. To remove any possible metallic impurities, the glassy carbon plates were soaked in 1 M high purity nitric acid for 2 hours and rinsed with deionized water. Before every experiment, only the nitric acid treatment and mechanical polishing were carried out on the glassy carbon.

Carbon materials were first prepared by dispersing them in ethanol. 1 ml of ethanol and 5 µl of Nafion® binder solution were added for every 1 mg of material. Nafion acts only as a binder for mechanical integrity and is not expected to have a major effect on the activity of the carbon materials under electrolysis conditions. The resulting mixture was then sonicated for 30 minutes to ensure adequate dispersion. For electrochemical testing, 30 µl of the mixture was drop-cast onto a glassy carbon plate and spin-coating at 1000 rpm was carried out to ensure evenness. An additional 30 µl mixture was coated on top of the initial layer followed by a final layer using 20 µl. Therefore in total, 80 µl of mixture was effectively deposited onto the glassy carbon substrates. To take into account the losses from spin-coating, separate electrodes were prepared by drop-

casting the carbon materials onto glassy carbon, which were then allowed to dry (see SI). Cu nanoparticles were drop-cast and spin-coated onto a glassy carbon plate with a suspension containing 71.4 µg of Cu in 1 ml of ethanol using an identical method. To take into account losses of material during spin-coating, 3 samples were made using this procedure and subsequently each of them were soaked into 1 M nitric acid to dissolve the Cu nanoparticles. The resultant solution was then analyzed using ICP-MS to determine the Cu concentration, which then can be directly correlated to the actual mass loading of Cu on the glassy carbon plate. It was determined that on average, 3.35 µg out of the 5.71 µg of Cu nanoparticles were successfully deposited each time. For electrolysis, only 1 cm^2 of the glassy carbon substrate is exposed to electrolyte. Therefore, assuming an even dispersion of nanoparticles, it was determined that 0.692 µg of Cu nanoparticles is present in 1 cm^2. To obtain a lower loading of nanoparticles, the same Cu nanoparticle suspension was diluted by a factor of 2 with ethanol to obtain 0.346 µg of Cu on GC (in 1 cm^2).

Preparation of electrolytes

To make 0.1 M $NaHCO_3$ solution, a 0.05 M Na_2CO_3 solution was bubbled for 1 hour with CO_2. To confirm that all the carbonate present is converted to bicarbonate, the pH to make sure it reaches a value of 6.8.[21] Pre-electrolysis of the electrolyte was also carried out to remove any metallic contaminants that might be present.[4] For this procedure, platinum gauze was used as the working electrode in a 2 electrode configuration and a cathodic potential of -2 V was applied for 24 hours. Another piece of platinum gauze was used as the counter electrode. Before electrolysis, the electrolyte was bubbled with CO_2 until the pH of the solution reached a value of 6.8 to ensure that the solution was CO_2 saturated.[6] To prepare Cu spiked electrolytes, appropriate amounts of Cu (II) sulfate hydrate were added to make 0.1 M $NaHCO_3$ solutions with Cu concentrations of 0.01, 0.1, 1 and 2 ppm.

Electrochemical measurements and product analysis

Details on these are identical to that reported in section 2.2.1.

2.3.3 Results and Discussion

A method was developed for leaching metallic impurities from the carbon material and then analyzing the leachate with inductively coupled plasma mass spectrometry (ICP-MS), a technique which has detection limits in the parts per trillion range. Fixed amount of PG, CNT, and GO and were sonicated separately for 3 h in ultra-high purity concentrated nitric acid. The materials were then filtered, and the filtrate was analyzed using ICP-MS. The amount (in ppm by mass) of each impurity removed from the carbon support can be easily calculated from its concentration in the filtrate. The results shown in Table 2.1 demonstrate that significant quantities of the first row transition metals Mn, Fe, Ni, and Cu are present in GO, PG, and CNT. To assess the effectiveness of the first nitric acid wash in removing impurities, a second nitric acid wash was carried out. As shown in Table 2.1, much lower impurity levels were found in the second wash relative to the first wash. We should note that prior work with acid washing has shown that is difficult to remove all impurities from carbon materials, especially CNTs, due to intercalation of the metals within the graphitic structure or sheathing within graphene sheets.[15,17,18] Although it is difficult to rule out

such a scenario from occurring here, we believe the procedure used here provides a reliable estimate of the type and concentration of impurities in the as-received carbon materials.

Table 2.1 Calculated impurity concentrations in ppm/w of metallic impurities in the as-received carbon materials based on extraction with ultrapure nitric acid and ICP-MS analysis.

Sample	Calculated impurity concentrations (ppm/w)			
	Mn	Fe	Ni	Cu
PG	N.D	3.71	N.D	0.01
PG wash 2	N.D	N.D	0.992	N.D
GO	3600	50.8	3.46	119
GO wash 2	182	2.32	1.00	1.09
CNT	10.7	84.9	1150	3.00
CNT wash 2	N.D	3.94	60.2	N.D
PG, high purity graphite; GO, graphene oxide, CNT, carbon nanotubes. N.D: Not Detected				

Table 1 demonstrates that GO contains the highest level of impurities – Mn, ~3800 ppm; Cu, ~ 120 ppm; Fe, ~53 ppm; and Ni, ~4 ppm. CNT contains lower levels of impurities – Ni, ~1200 ppm; Fe, ~ 90 ppm; Mn, ~11 ppm; and Cu, 3 ppm. The cleanest material is PG, which contains only ~ 4 ppm of Fe and 0.01 ppm of Cu.

CO_2R activity of unmodified materials

CO_2R was performed at a cathodic potential of -1.3 V (vs. RHE) for 2 h in 0.1M $NaHCO_3$. The product distributions and current densities for each sample are summarized in Figure 2.2. The GC electrode shows low activity and produces mainly H_2 and a very small amount of CO and HCOOH. PG dispersed on GC is somewhat more active but the distribution of products is similar to that seen for GC alone. GO dispersed on GC produces methane with a faradaic efficiency (FE) of 4.3%. CNT dispersed on GC has the highest current density, 3.2 mA cm^{-2}, and a FE of nearly 100% for H_2.

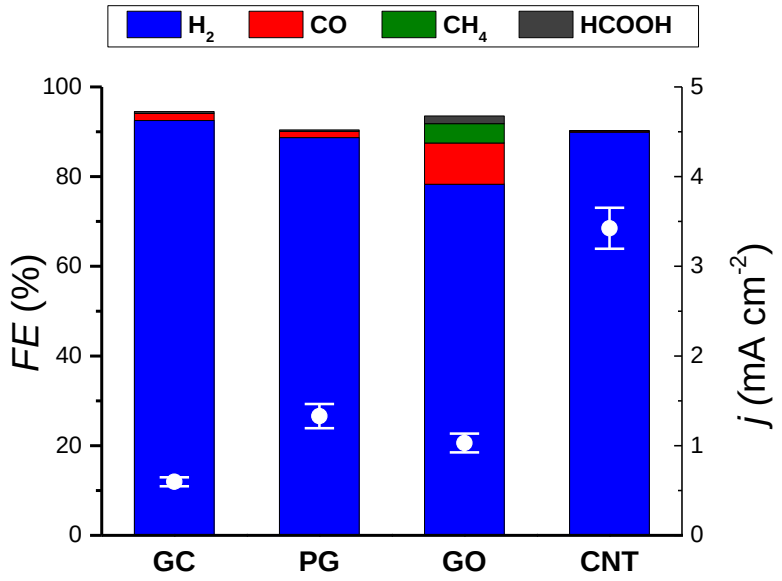

Figure 2.2 Faradaic efficiencies (FE, shown as bars, left hand axis) and current densities (open white circles with error bars, right hand axis) of a glassy carbon electrode (GC) and as-received carbon supports dispersed on glassy carbon electrodes: high purity graphite (PG), graphene oxide (GO), and carbon nanotubes (CNT). Electrolysis was carried out at -1.3V vs RHE for 2 hours in 0.1M $NaHCO_3$ solution.

The activity of GO/GC for methane production strongly implies that the formation of methane is due to the small amounts of Cu present as impurities in GO. The CNT/GC sample exhibited the highest current density and nearly 100% selectivity for H_2 production. The high activity of this sample is likely due to presence of nickel impurities, since Ni is known to be an active catalyst for the hydrogen evolution reaction (HER).[22,23] GC and PG/GC show high FEs for hydrogen but lower current densities than that observed for CNT/GC. The low activity of these samples is very likely due to their low level of contamination by metallic impurities.

GO also contains other metal impurities, in particular Mn and Fe. Under CO_2R conditions, Fe is known to produce H_2 with > 90% Faradaic efficiency[2,4] and similarly for Mn.[12,24] These impurities likely compete with Cu, which explains why, in addition to methane, GO/GC produces ~80% hydrogen. Also, GO/GC was observed to produce a significant amount of CO, while both GC and PG/GC produce a small amount of CO.

CO_2R activity of materials washed with high purity nitric acid

The CO_2R activities of PG/GC, GO/GC, and CNT/GC determined after washing in ultrapure nitric acid are shown in Figure 2.3. The methane formation observed for the as-received GO/GC is clearly eliminated by the washing procedure. Concomitantly, the current density for all three carbon samples decreased to 1 mA cm^{-2} or lower. For GO/GC, we attribute the elimination of methane formation to the removal of the Cu impurities in the GO. The data in Table 1 show that after two washings, the Cu concentration in GO is reduced by an order of magnitude. After

washing, PG/GC, CNT/GC and GO/GC generate predominantly hydrogen together with a small amount of CO and HCOOH. The observed formation of CO and HCOOH might be due to the intrinsic electrocatalytic property of the carbon materials, which might have been previously concealed due to the presence of metallic impurities. It is also possible that the nitric acid treatment might have induced certain defects into the carbon structure, which might be active for CO and HCOOH generation.

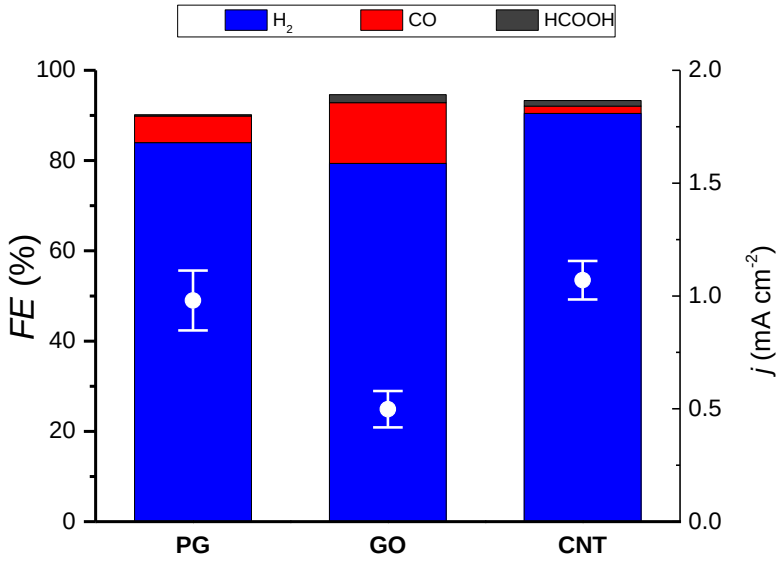

Figure 2.3 Faradaic efficiencies (FE, shown as bars, left hand axis) and current densities (open white circles with error bars, right hand axis) high purity nitric acid washed carbon supports dispersed on glassy carbon electrode. Treatment with high purity nitric acid removes any methane formation. Electrolysis was carried out at -1.3V vs RHE for 2 hours in 0.1M $NaHCO_3$ solution.

Electrocatalytic activity as a function of Cu content

The results presented above indicate that the formation of methane during the CO_2R from as-received GO/GC can be attributed to the presence of Cu impurities in the GO. While the Cu content of this catalyst is only ~120ppm, its mass activity for methane production at an applied voltage of -1.3 V vs RHE is very high, 54.67 mmol g^{-1} s^{-1}. This observation suggests that very low loadings of Cu on carbon supports may exhibit high activities. To explore this idea, Cu was intentionally added in ppm quantities (0.01 ppm to 2 ppm) to the sodium bicarbonate electrolyte. Then CO_2R experiments were carried out with the acid-washed GO/GC and as-received PG/GC. CNT/GC was not tested due to difficulties in completely removing metallic impurities from CNTs. Experiments were also conducted with Cu electrodeposited on GC and with Cu nanoparticles dispersed on GC.

The deposition of Cu onto the carbon supports at an applied potential of – 1.3 V vs RHE is expected as the standard potential for reduction of Cu^{2+} to Cu^0 is +0.34V vs RHE.[25] The maximum amount of Cu that can be deposited is determined from concentration of copper in the electrolyte and the volume of electrolyte used (0.5 ml) (Table 2.2). For ease of reading GC, GO/GC, and PG/GC

tested in electrolyte containing 0.1 ppm copper will be termed Cu(0.1)GC, Cu(0.1)GO/GC, and Cu(0.1)PG/GC. Similar notation is used to identify samples produced from electrolyte solutions containing lower and higher concentrations of Cu^{2+}.

Table 2.2 Comparison of the mass activity per unit mass of Cu to methane formation of graphene supported Cu versus Cu nanoparticles on glassy carbon. Cu was loaded onto the GO electrode by electrodeposition from electrolytes spiked with Cu at the indicated concentrations (see text).

Sample / Electrolyte	Partial current density to methane ($mA\ cm^{-2}$)	Total amount of Cu (μg)	Methane Activity ($mmol\ g^{-1}\ s^{-1}$)	Particle size (nm)
GO as received/GC	0.0452	$1.07x10^{-3*}$	54.67	-
Cu(0.01)GO cleaned/GC	0.005	$1.93\ x10^{-3}$	3.50	-
Cu(0.1)GO cleaned/GC	0.201	$4.23\ x10^{-2}$	6.17	-
Cu(1)GO cleaned/GC	1.453	$3.63\ x10^{-1}$	5.18	-
Cu(2)GO cleaned/GC	2.005	$6.51\ x10^{-1}$	3.99	8.6
Cu(0.1)PG/GC	0.197	$4.23\ x10^{-2}$	6.04	-
Cu(1)PG/GC	1.001	$3.63\ x10^{-1}$	3.58	-
Cu(2)PG/GC	2.258	$7.30\ x10^{-1}$	4.00	27.0
Cu(0.1)GC	0.030	$4.23\ x10^{-2}$	0.919	-
Cu(1)GC	0.121	$3.63\ x10^{-1}$	0.433	-
Cu(2)GC	0.479	$6.39\ x10^{-1}$	0.97	31.2
Cu NPs/GC	0.287	$3.46\ x10^{-1\#}$	1.08	12.0
Cu NPs/GC	0.756	$6.92\ x10^{-1\#}$	1.42	12.0

*already present as an impurity in as-received GO

#mass of Cu nanoparticles loaded on 1 cm^2 of glassy carbon

SEM images of the morphology of the carbon materials were taken before and after CO_2R for two hours with 2 ppm of copper initially in the electrolyte (Figure 2.4). These images show that during the CO_2R experiment copper is electrodeposited as nanoparticles. The average size of the copper nanoparticles are 8.6 nm, 27.0 nm, and 31.2 nm for Cu(2)GO/GC, Cu(2)PG/GC and Cu(2)GC, respectively. The surface of the GO/GC shows no evidence of Cu nanoparticles. TEM inspection of Cu(0.1)GO/GC taken after CO_2R did show Cu nanoparticles.

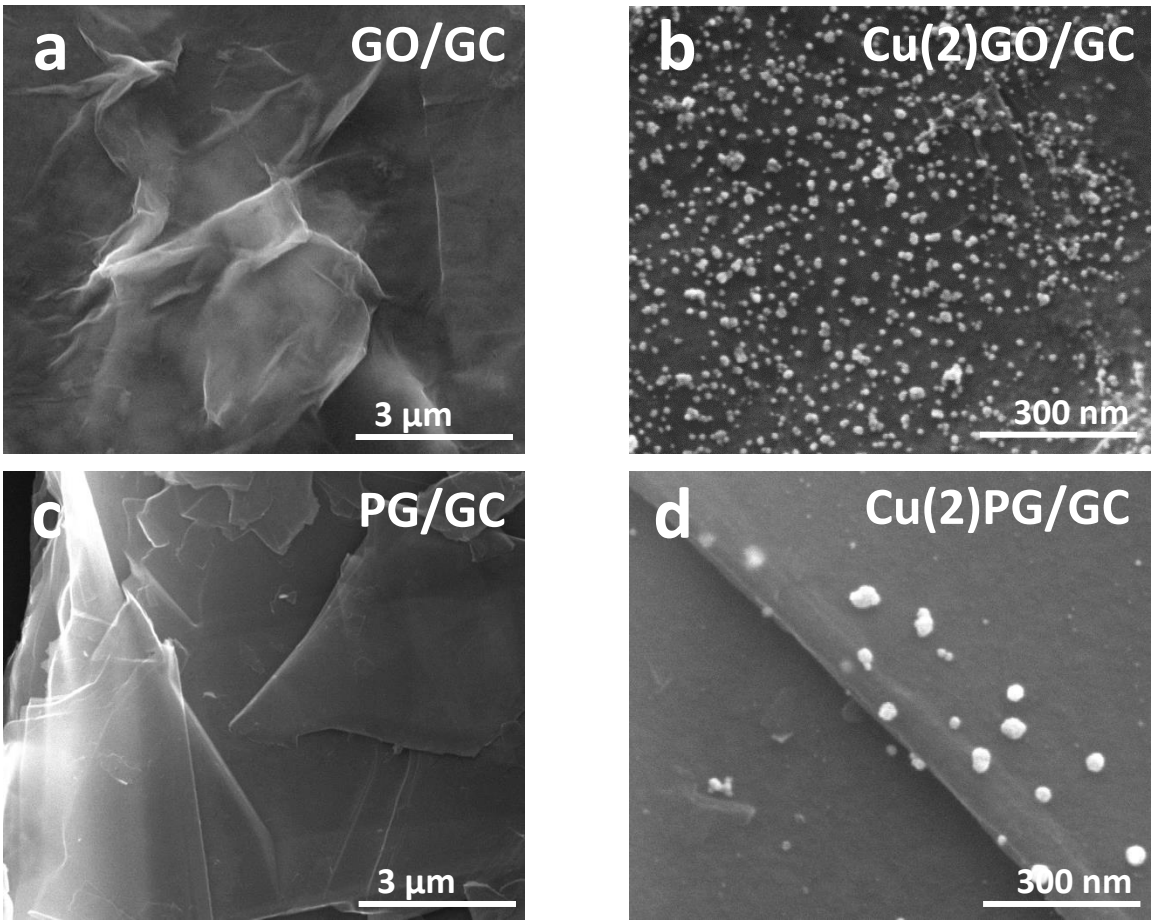

Figure 2.4 SEM images of GO (a) and PG (c) deposited on glassy carbon. (b) and (d) are higher magnification images after Cu electrodeposition from an electrolyte containing 2 ppm of Cu and 2 hours of operation at -1.3 V vs. RHE in CO_2 saturated electrolyte. The bright spots are Cu nanoparticles (NPs) with an average size of 8.6 nm on GO (b), and 27.0 nm on PG (d).

The catalytic CO_2R activity of these carbon materials with deposited Cu was tested. Figure 2.5 shows the product distributions and the measured current densities for CO_2 reduction conducted over Cu(X)GO/GC and Cu(X)PG/GC in electrolytes containing different initial concentrations of Cu, where X is the initial concentration of Cu in the spiked electrolyte. It is apparent that with increasing copper concentration in the electrolyte both the current densities and the FEs for methane increase for all both PG and GO. For both Cu(1)GO/GC and Cu(1)PG/GC, the FE for methane reaches about 40%. This FE is comparable to values reported for copper foil, although

the Cu foil has a higher current density;[4,6] for Cu(2)GO/GC, the current density is ~4.6 mA cm^{-2}, which is a factor of 2-3 lower than that for a Cu foil (~10 mA cm^{-2}) at similar applied potentials.[4,6] The highest selectivity for methane formation is observed on Cu(2)PG/GC and Cu(2)GO/GC. This is particularly interesting in a direct comparison with GC at identical copper loadings shows much lower activity on the Cu on GC. For example, the FE for methane only reaches 12.9% for Cu(2)GC compared to 43.6% for Cu(2)GO/GC or 38.8% for Cu(2)PG/GC.

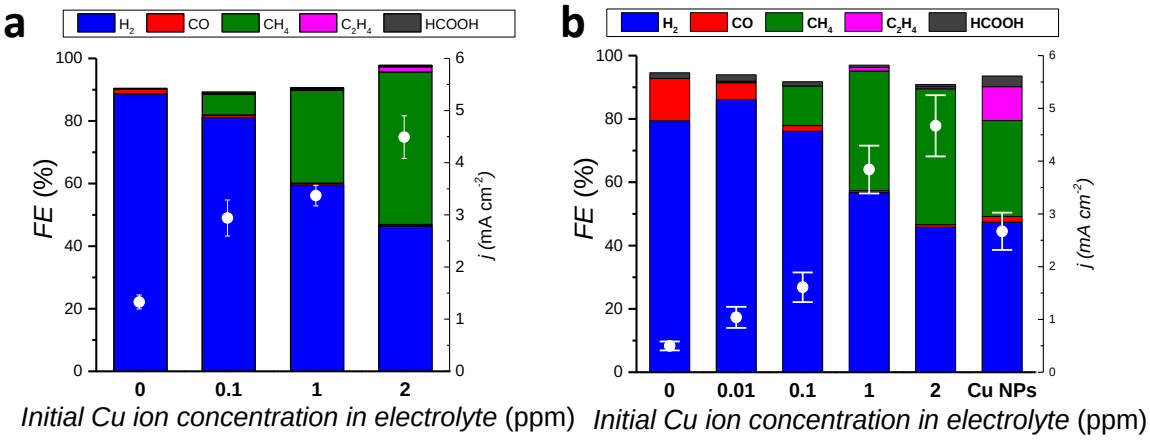

Figure 2.5 Faradaic efficiencies (FE, shown as bars, left hand axis) and current densities (open white circles with error bars, right hand axis) (a) cleaned graphene oxide (GO) with the indicated concentrations of Cu ion initially "spiked" in the electrolyte and Cu nanoparticles (Cu NPs, 9.69 µg loading) loaded on GC and (b) as-received PG with various concentrations of Cu initially "spiked" in the electrolyte. Electrolysis was carried out at -1.3V vs RHE in 0.1M $NaHCO_3$ solution for 2 h.

To further explore each samples specific activity to methane, the mass activity of Cu in Cu(X)GO/GC, Cu(X)PG/GC, and Cu(X)GC was calculated at an applied voltage of – 1.3 V (Table 2.2). The activity of Cu NPs deposited on GC was also calculated at the same voltage for comparison. For further comparison the methane mass activity for as-received GO/GC due to the Cu impurity was calculated in Table 2.2. The methane activity per unit mass of Cu of uncleaned GO/GC is as much as two orders of magnitude higher than that of any other sample examined. Cu electrodeposited onto acid-washed GO supported on GC (Cu(X)GO/GC) is comparable to that of Cu(X)PG/GC. While some differences in the methane activity per gram of Cu are observed with Cu loading, these variations are not systematic. In all cases the activity of these samples is about an order of magnitude lower than that for uncleaned GO/GC. An additional observation is that the activity of Cu electrodeposited onto GC is ~ 4-5 times lower than that of Cu(X)GO/GC or Cu(X)PG/GC.

It is interesting to consider why Cu electrodeposited on GO/GC and PG/GC exhibits significantly higher methane activity per gram of Cu than Cu electrodeposited on GC or premade Cu NP dispersed on GC. Some insights into this question can be drawn from a theoretical investigation of the CO_2R occurring on copper nanoclusters (~0.9 nm in diameter) supported on graphene at

defect sites.[26,27] This work indicates that the activation energy for the protonation of adsorbed CO to form adsorbed CHO, the elementary step believed to be rate-limiting step for CH_4 formation, is ~ 30% of that for the same reaction occurring on a Cu (111) surface. This effect is attributed to greater orbital hybridization of the copper nanoparticles on graphene with the adsorbed CHO intermediate compared to Cu (111) surface, leading to greater stabilization of the intermediate. The authors also show that the energy barrier for HER on these graphene-supported copper nanoparticles is slightly higher than that determined for the HER occurring on a Cu (111) surface, indicating a slight suppression of HER. We, therefore, propose that the Cu impurities present on as-received GO may be segregated preferentially at defects on the GO planes and that Cu associated with such sites may be exceptionally active. By extension, we propose that electrodeposition of Cu onto acid-washed GO/GC or PG/GC places a significant fraction of the Cu onto defect sites present in either acid-washed GO or as-received PG. If this reasoning is correct, then the lower activity of Cu electrodeposited on GC may be a consequence of a lower level of defects on the GC than on GO or PG.

2.3.4 Conclusions

The studies performed here demonstrate that as-received carbon supports can contain significant concentrations of metallic impurities which are active for CO_2R. Of particular note is GO, for which the major metallic impurity is Cu. The presence of Cu in as-received GO explains why this material is active for the formation of methane during the electroreduction of CO_2. Nearly all of the catalytically relevant metallic impurities can be removed from GO by washing in ultrapure nitric acid. When this is done, the electrochemical activity for both GO and the other carbon supports tested here decreases and the activity for methane formation on GO disappears. Furthermore, Cu can be added back to the now clean carbon supports via electrochemical deposition. When this is done the activity for methane formation returns and increases with an increase in the amount of Cu deposited. The activity per mass of Cu is ~ 4-5 times higher when Cu is deposited onto GO or PC dispersed on GC as compared to Cu deposited onto GC. The higher electrochemical activity of Cu electrodeposited on to GO/GC or PG/GC is attributed to the preferential deposition of Cu NPs at defects present on the graphene layers of GO and PG. This effect is thought to be more extreme in the as-received GO/GC which shows the Cu highest mass activity for methane production. This work suggests that a highly active catalyst for methane formation via the CO_2R can be created by the introduction of defects into graphene layers, onto which Cu can then be electrodeposited and exhibit enhanced activity.

Chapter 3: CO_2 electroreduction with enhanced ethylene and ethanol selectivity via nanostructuring of polycrystalline copper

3.1 Introduction

The storage of energy in the form of chemical fuels via electrochemical reduction of carbon dioxide could be an attractive alternative to the use of fossil fuels.[4,28,29] To achieve high energy density, it is preferable that the fuel be a hydrocarbon, since any oxygen in the fuel reduces its energy density. Furthermore, products with oxygen (oxygenates) such as ethanol are highly soluble in water, which introduces an energy cost due to separation issues. Extensive research on electrochemical CO_2 reduction (CO_2R) conducted over the past three decades has shown that only metallic copper can facilitate the electrochemical reduction of CO_2 to hydrocarbons with high Faradaic efficiencies and reasonable current densities.[4,6,7] However, electrochemical reduction of CO_2 to hydrocarbons on copper requires overpotentials on the order of 1 V and produces a broad product spectrum without high selectivity to any particular product.[4,6] The published literature also shows that the distribution of products is highly dependent on the manner in which Cu has been pretreated. For example, *Kanan* and co-workers have shown that oxide-derived Cu nanoparticles are active at overpotentials of -0.25 to -0.5 V vs RHE for CO_2 electroreduction and can produce C_{2+}oxygenates.[30–32] In similar work, *Mul* and co-workers have shown that copper nanoparticles deposited on copper plates by electrodeposition of copper oxide films and subsequent electroreduction to copper exhibit an ethylene selectivity of 36% and an ethylene to methane ratio of ~30 at an applied potential of -1.2 V vs RHE.[33]

The major hydrocarbon products produced by the electrochemical reduction of CO_2 over Cu are methane and ethylene. Ethylene is an attractive product since it can be converted to liquid fuels by oligomerization.[34] Methane is not as valuable as ethylene and is readily available from natural gas.[35] Therefore, the design of a catalyst to produce ethylene in high selectivity is an attractive proposition. Recent work has shown that nanostructuring of polycrystalline copper by electrochemical cycling in the presence of Cl^- anions increases the selectivity to ethylene and suppress the selectivity to methane.[36,37] SEM characterization of such nanostructured surfaces shows that they are covered by a large number of cubes exposing Cu(100) facets. This could explain the increased selectivity since single crystal studies by *Hori* and coworkers have shown that Cu(100) surfaces exhibit a high selectivity to ethylene.[4] We note further that in a recent study of CO reduction,[38] a known intermediate of CO_2R,[4] it was found that the enhancement of ethylene formation on Cu cubes was most similar to that observed on the Cu (100) surface.

The formation of the cubic nanostructures has been attributed to the presence of Cl^- anions which results in CuCl formation under oxidizing conditions.[37] The CuCl precipitates as cubes on the surface.[37,39] The CuCl readily converts to CuO_x, which can be reduced to metallic Cu under reducing conditions. The objective of the present work is to examine the role of halide identity on the nanostructuring of Cu and the consequent effects on both the activity and selectivity of the restructured Cu for the electrochemical reduction of CO_2. Our results show that the use of halide anions (F^-, Cl^-, Br^- and I^-) to nanostructure polycrystalline copper results in a higher ethylene to methane ratio (C_2H_4/CH_4) and an increase in ethanol selectivity.

3.2 Experimental

Potassium carbonate (≥99.995% metals basis), potassium fluoride dihydrate (98%), potassium chloride (≥99.0%), potassium bromide (≥99.0%) and potassium iodide (≥99.0%) were purchased

from Sigma Aldrich. Phosphoric acid (85.0-87.0% assay) was purchased from J.T. Baker. Copper foil (0.1 mm thick, 99.9999% metals basis) was purchased from Alfa Aesar. Carbon dioxide (99.995%), Nitrogen (99.999%), Helium (99.999%) and Hydrogen (99.999%) were purchased from Praxair. Hydrogen, Helium, Nitrogen, Carbon dioxide gas purifiers were purchased from Valco Instruments Co. Inc. All chemicals were used without further purification. Electrolyte solutions were prepared with 18.2 MΩ deionized (DI) water from a Millipore system. 0.1 M $KHCO_3$ electrolyte solution was prepared by bubbling 0.05 M K_2CO_3 solution with CO_2 gas for at least 2 h or until a pH of 6.8 was achieved. Electrolyte solution containing 4 mM of halide anion was prepared by adding the appropriate mass of potassium halide salt to 0.1 M $KHCO_3$ solution.

Copper foil (99.9999%) was cut into electrodes of 2 cm by 2 cm squares and cleaned by sonicating for 30 min in acetone, followed by isopropanol and finally in deionized water. The electrodes were then electropolished in concentrated phosphoric acid at a potential of 2.0 V for 5 min with a copper foil counter electrode. Next, the electrodes were rinsed with DI water and dried with a stream of nitrogen. Nanostructuring of electropolished polycrystalline copper was carried out *in-situ* prior to carrying out the electroreduction of CO_2 in a 0.1 M $KHCO_3$ solution containing 4 mM of KCl. The electrolyte was first sparged with CO_2 until the pH reached 6.8. Prior to carrying out CO_2 reduction, each polycrystalline copper electrode was cycled between -1.1 V to 0.9 V (vs. RHE) at 20 mV s^{-1} for 3 cycles. The electrolyte was then removed and fresh 0.1 M $KHCO_3$ electrolyte without halide was added for CO_2 electroreduction. The morphology of the nanostructured and electropolished polycrystalline copper electrodes was examined using a FEI Quanta 200 FEG SEM.

Electrochemical measurements were carried out using a Biologic SP-300 potentiostat. Ambient pressure CO_2 electrolysis was carried out in a custom-made gas-tight electrochemical cell made of PEEK and fitted with Teflon coated gaskets (see figure 3.1). The configuration of the electrochemical cell is such that the working electrode is parallel with respect to the counter electrode (platinum foil) to ensure a uniform potential distribution across the surface. The separation between the cathode and anode is 2.5 cm. The geometric surface area for both of the electrodes is 1.13 cm^2. A Selemion AMV anion exchange membrane (110 μm thickness) was used to separate the anodic and cathodic compartments. Each of the compartments in this cell contains a small volume of electrolyte (1.8 ml each) to concentrate liquid products and therefore increase detection limits. The headspace of the cathodic compartment was approximately 3 ml. Before conducting CO_2 electrolysis, the electrolyte in the cathodic compartments was purged with CO_2 for at least 15 min. During electrolysis, CO_2 was bubbled through the electrolyte at a flow rate of 5 sccm in order to prevent CO_2 depletion. The flow rate of CO_2 was controlled with a mass flow controller (Alicat Scientific), and the gas was first humidified with water by passing it through a water-filled bubbler to minimize evaporation of electrolyte. For all experiments, platinum foil was used as the counter electrode and an Ag/AgCl electrode (leak free series) from Innovative Instruments, Inc was used as the reference. Data were converted to the RHE reference scale using the equation: $E_{vs.\ RHE} = E_{vs.\ Ag/AgCl} + 0.197\ V + 0.0591 \times pH\ (6.8)$. To ensure the accuracy of the reference electrodes, calibration was done with a homemade reversible hydrogen electrode. Prior to any electrolysis, the solution resistance was first determined using electrochemical impedance spectroscopy by scanning from 1 MHz to 10 Hz. For all reported CVs and electrolysis, measurements were made with the potentiostat set to compensate for 85% of the measured IR drop.

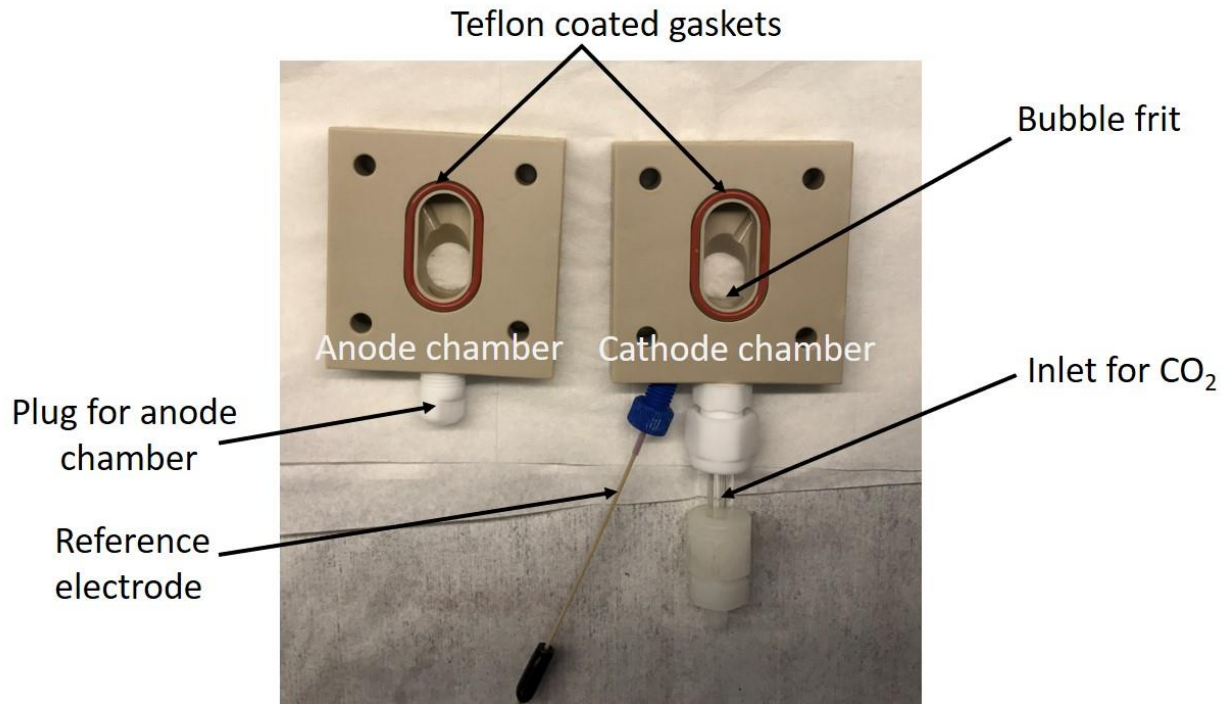

Figure 3.1 Picture of the custom-made electrochemical cell, showing the anode chamber (left) and the cathode chamber (right). A reference electrode can be inserted into the cathode chamber from the bottom as shown. An inlet for flowing CO_2 in the cathode chamber is also shown with a bubble frit at the end. The purpose of the frit is to generate small bubble of CO_2 in order to aid with gas dispersion.

Analysis of gaseous products was carried out with a gas chromatograph (SRI instruments) equipped with a packed HaySep D column and a packed MolSieve 5A column. A flame ionization detector (FID) with a methanizer was used to detect hydrocarbons (CO, CH_4, C_2H_4 and C_2H_6) with He as the carrier gas. A thermal conductivity detector (TCD) was used to detect hydrogen with nitrogen as the carrier gas. Calibration of the gas chromatograph was done using calibration gas from Praxair (UN 1956) with 0.1% CO, 0.099% ethane, 0.099% ethylene, 0.1% hydrogen, 0.1% methane and balance as helium. Additional calibration points were obtained by dilution of the calibration gas with appropriate flow rates of helium. Further calibration for hydrogen was done with a calibration mixture obtained from Praxair (UN 1956) containing 500 ppm of hydrogen in nitrogen. After passing through the cell, CO_2 flowed directly into the gas sampling loop of the gas chromatograph for online gaseous product analysis, which was carried out every 30 min. For all experiments, electrolysis was allowed to proceed for 1.5 h with gas analysis done at 10, 35, 60 and 85 min. Data obtained for all durations were averaged to obtain the Faradaic efficiencies of the various products. In the timeframe of our experiments, significant differences in the products observed during the course of the run were not observed.

The liquid products were collected from the cathode and anode chambers after electrolysis and analyzed by High-Performance Liquid Chromatography (HPLC) using a UltiMate 3000 from Thermo Scientific. Vials with the collected samples were placed in an autosampler holder and 10

μL of sample was injected into the column. An Aminex HPX 87-H column (Bio-Rad) was used together with diluted sulfuric acid (1 mM) as the eluent. The temperature of the column was maintained at 60°C in a column oven, and the separated compounds were detected with a refractive index detector (RID). The expected products of CO_2 reduction (CO_2R) were analyzed as well by HPLC to produce a standard calibration curve at 60°C (i.e. formate, acetate, ethylene glycol, ethanol, and n-propanol).

Combined Raman spectroscopy and electrochemical studies were carried out in an epoxy-free Teflon cell.[40] A 5 mm polycrystalline copper disc sheathed in Teflon was used as the working electrode. Before any experiment, the copper disc was first mechanically and subsequently electrochemically polished in concentrated phosphoric acid. All Raman experiments were carried out in CO_2 saturated 0.1 M $KHCO_3$ with 4 mM KCl. *In-situ* Raman spectra of the electrodes were recorded using a confocal Raman microscope (LabRam HR, Horiba Jobin Yvon). Further details concerning the procedure can be found in Reference 39. [40].

3.3 Results and discussion

For the purpose of this work, we utilize the method outlined by *Roberts et al.* to carry out electrochemical cycling of the copper electrode with different halides.[37] Figure 3.2 shows cyclic voltammograms (CVs) obtained during the electrochemical cycling of polycrystalline Cu from -1.1 V to 0.9 V (vs. RHE) in the presence of 4 mM of halide anion. The spikes in the current profiles are attributed to electrolyte convection due to the continuous flow of gas through the cell. The CVs show an increase in the oxidative current ($F^- > Cl^- > Br^- > I^-$) as the anion is changed. Concomitantly, the reduction peak areas increase in the same order according to the anion used.

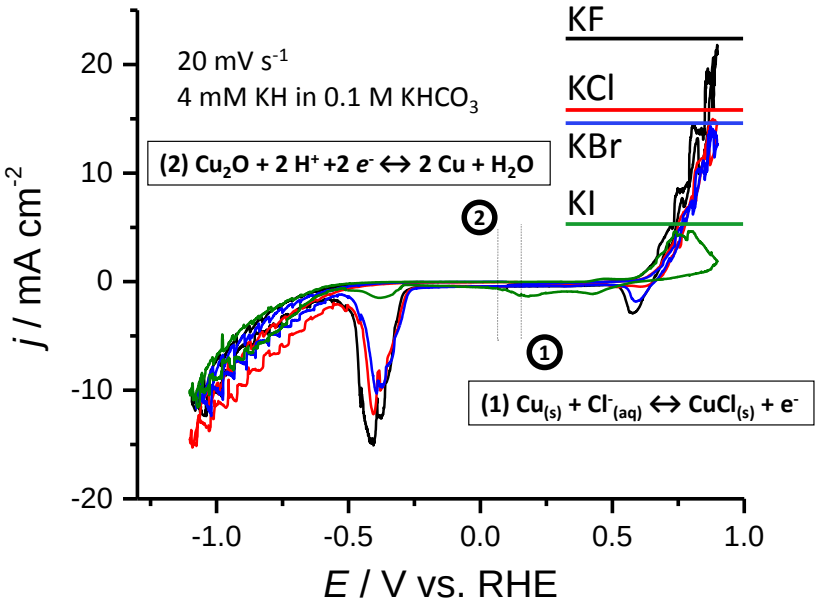

Figure 3.2 Cyclic voltammorgrams recorded during the electrochemical cycling of polycrystalline copper in the presence of different halide anions (4 mM) in the electrolyte (0.1 M $KHCO_3$ pH 6.8). For each sample was cycled three times. The green, blue, red and black lines represent the electrochemical cycling process in the presence of KI, KCl, KBr, and KF, respectively.

The product selectivity was determined at -1.0 V vs RHE by carrying out constant potential electrolysis for 1.5 h. A potential of -1.0 V was chosen because it has been shown previously that this is the potential at which the highest selectivity to ethylene can be achieved (a detailed investigation of the effect of potential is shown in the next chapter).[4,6] Figures 3.3a and 3.3d show the current densities and product distributions of electrodes cycled electrochemically in solutions containing different potassium halides as well as an uncycled electrode (no pretreatment). It can be seen that electrochemical cycling of the electrode between oxidizing and reducing voltage in KF, KCl and KBr results in an increase in current density observed during CO_2 reduction. For example, cycling in KCl resulted in a current density of 9.53 mA cm^{-2} as compared to that for polycrystalline copper (5.14 mA cm^{-2}). The geometric current densities of the different electrodes are in order: KCl>KF>KBr>KI, no pretreatment.

It is apparent that after electrochemical cycling, electrodes cycled in KF, KCl and KBr exhibit an enhanced Faradaic efficiency for production of ethylene (from 9.4% to ~15.2%) and ethanol (from 2.65% to ~ 7.6%) relative to polycrystalline copper at a potential of -1.0 V vs RHE (see Figure 3.2d). We note that the FE for production of ethylene and ethanol is poorer at -1.1 V after cycling with the halide and this is due to mass transport limitations of CO_2 which will be discussed in the next chapter. The Faradaic efficiency for production of methane is also reduced (from 4.55% to ~0.64%). Electrodes cycled with KI show an increased faradaic efficiency for these products, albeit with a smaller enhancement. Also, a smaller suppression of methane was observed due presumably to the fact that KI is unable to cause as much surface oxidation as the other anions. Electrochemical cycling with the other anions does not yield any significant difference in faradaic efficiency to ethylene and ethanol, although the use of KF does seem to yield a slightly better performance.

It is also interesting to note that the observation of ethanol as a primary product contrasts with previous studies, which only present evidence for formate anions in the liquid phase.[36,37,41] The ethanol selectivity was found to increase with the ethylene selectivity, due possibly to a common intermediate.[42] It was also observed that the propanol selectivity mirrors the ethanol selectivity, here again suggesting the possibility of a common intermediate with ethanol which is yet unknown.[6] It is also noted that electrochemical cycling of the electrode resulted in a lower selectivity towards hydrogen evolution.

Figure 3.3b and 3.3e illustrate the current densities and product distributions respectively as a function of applied potential for a KF-cycled electrode. As a comparison, the current densities and product distributions for polycrystalline copper are shown in figures 3.3c and 3.3f. It is clear from these results that the overpotential for ethylene formation on the KF-cycled electrode is lower than that found for the unreconstructed Cu electrode. Comparing figures 3.3e and 3.3f, it can be seen that the ethylene formation starts at -0.8 V for the cycled electrode whereas ethylene formation is only observed beginning at -0.9 V for the control electrode.

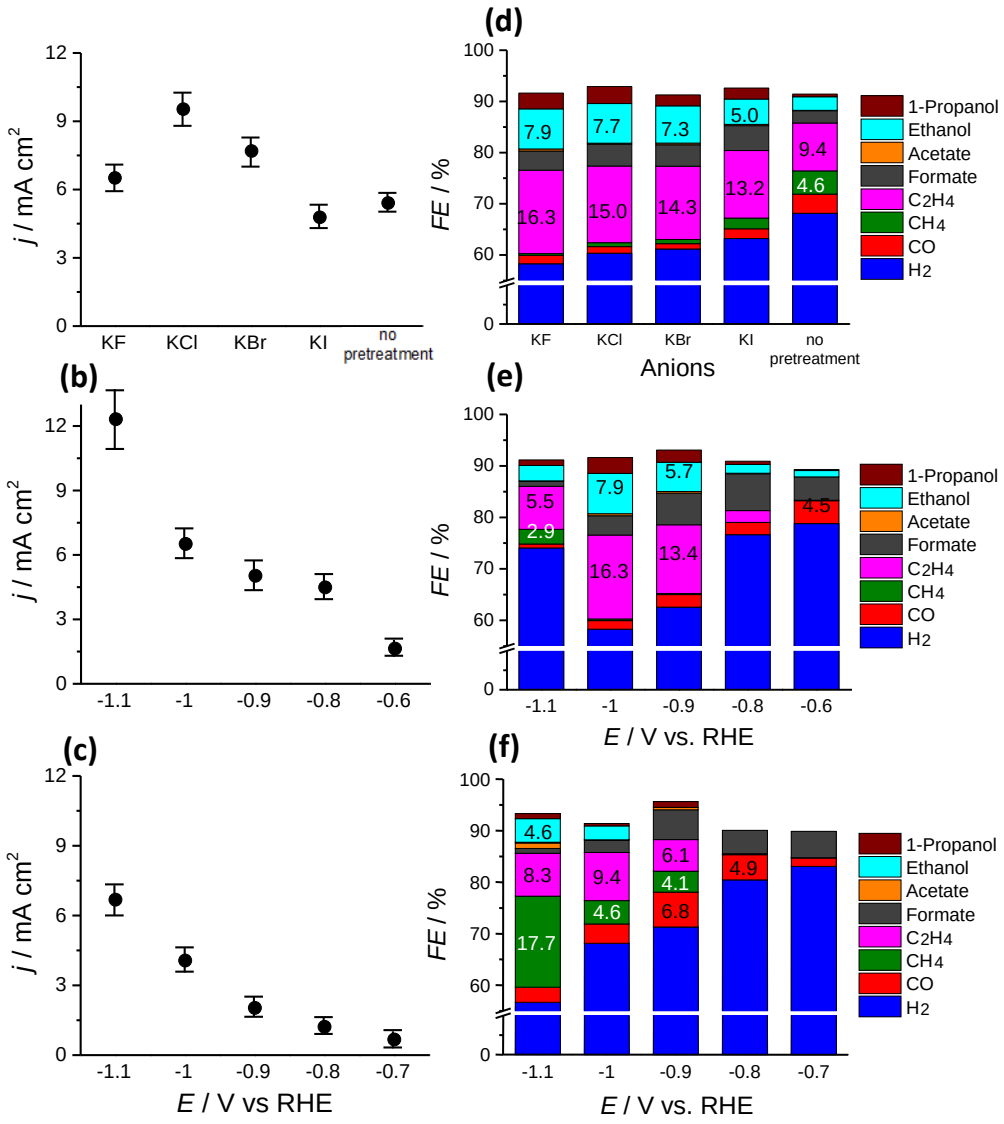

Figure 3.3. (a)-(c) Current densities and (d)-(f) corresponding product distributions of various nanostructured electrodes and polycrystalline copper. (a) and (d) are the current densities and product distributions as a function of halide anion at a fixed potential of -1.0 V vs RHE. (b) and (e) are the current densities and product distributions as a function of applied potential of a KF cycled electrode in 0.1 M $KHCO_3$. (c) and (f) are the current densities and product distributions obtained as a function of applied potential for polycrystalline Cu electrode in 0.1 M $KHCO_3$.

Even though the halide-containing electrolyte is removed before CO_2 reduction and replaced with a fresh electrolyte (without halide), it is unavoidable that trace amounts of halide remain. To determine if the presence of halide anions in the electrolyte has an effect on the product selectivity, electrolysis under identical conditions (-1 V vs RHE) was carried out with polycrystalline copper in 0.1 M $KHCO_3$ containing 4 mM of KF without prior electrochemical cycling (control). The results for this experiment are shown in Figure 3.4. For electrodes which have not been cycled (control), but with KF in the electrolyte, the presence of the halide anion does not significantly

change the current density (Fig. 3.4(a)) or the product distribution (Fig. 3.4(b)). Next, the maximum oxidizing potential during electrochemical cycling was decreased from 0.9 V to 0.8 V (vs RHE) to determine if that had an effect on the selectivity of the KF-cycled electrode. Use of this maximum oxidizing potential did not change the selectivity relative to that for polycrystalline Cu. At a maximum oxidizing potential of 0.9 V vs. RHE the number of cycles was increased from 3 to 5 in order to determine if additional cycling would affect the selectivity. When the number of cycles was increased to 5, the current density increased and the C_2H_4/CH_4 ratio decreased to 12.9. This indicates that there might be an optimal number of cycles for nanostructuring of polycrystalline copper.

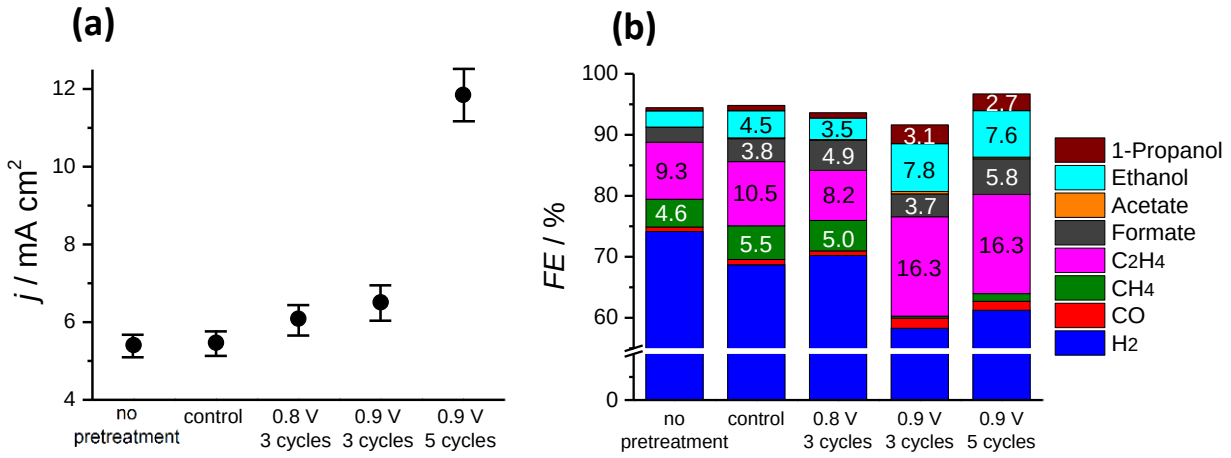

Figure 3.4. (a) Current densities and (b) product distributions obtained for different electrodes at an applied potential of -1.0 V vs RHE in 0.1 M $KHCO_3$. Electrodes were pretreated under different nanostructuring conditions, as annotated on the graphs. Cycled electrodes were prepared in the presence of 4 mM KF. For the 'control' case, cycling was not carried out; however 0.1 M $KHCO_3$ with 4 mM KF was still used as the electrolyte.

It is important to understand how the morphology and composition of the electrode surface changes during the electrochemical cycling process. It has been proposed previously that CuO_x formed during oxidation reduces back to metallic copper under a reducing potential.[37] However, it is unknown whether Cu_2O or CuO forms preferentially or if these oxides remain upon application of a negative potential. In situ Raman spectroscopy was used to track the changes in the composition of the Cu cathode and the morphological changes were observed by SEM. Raman spectra were acquired as the electrode was cycled from zero applied potential to 1.1 V vs RHE and then down to -0.6 V. These experiments were done in 0.1 M $KHCO_3$ electrolyte containing 4 mM KCl in order to enable comparison with similar studies reported earlier.[36,37] Linear sweep voltammetry was carried out on the copper working electrode to various oxidative potentials and then to negative potentials of -0.35 V and -0.6 V. A potential of -0.35 V and -0.6 V allows for partial and full reduction of CuO_x on the surface, respectively.[37] At each potential, Raman spectra were recorded and the morphology of the surface was characterized ex situ by SEM (Figure 3.5). At zero applied potential the Raman spectra of polycrystalline copper showed no obvious features between 100 cm^{-1} and 700 cm^{-1}. However, as the potential was increased past 0.7 V, peaks attributable to Cu_2O became visible at 148 cm^{-1} (infrared allowed mode), 220 cm^{-1} (second-order

Raman-allowed mode), 420 cm^{-1} (adsorbed OH^- species), 521 cm^{-1} (second-order overtone mode), and 634 cm^{-1} (infrared allowed mode)[43–45] Based on the voltammogram and the Raman spectra, the onset of Cu_2O formation is found to begin at around 0.7 V. Increasing the potential from 0.7 V to 0.9 V did not lead to the appearance of peaks for CuO leading to the conclusion that cycling to 0.9 V produces an oxide layer that contains predominantly Cu_2O.

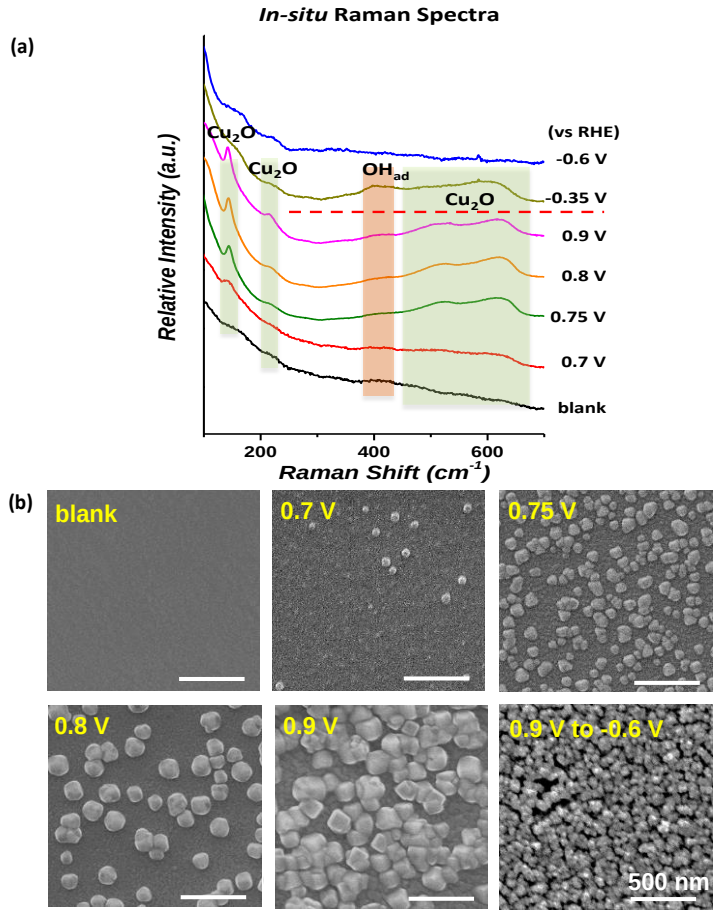

Figure 3.5. (a) *In-situ* Raman spectra of Cu foil during electrochemical cycling and (b) corresponding SEM images. This electrochemical cycling was carried out with 4mM of KCl in the electrolyte and corresponds to only 1 cycle.

When the potential was increased beyond 0.9 V, formation of CuO began to occur at 1.0 V, as confirmed by the appearance of Raman peaks at 290 cm^{-1} and 340 cm^{-1}, corresponding to the zone-centered optical phonon modes of CuO.[46,47] At the same time, the Raman peak at 148 cm^{-1} for Cu_2O diminished, which indicates that with increasing oxidation potential, CuO forms preferentially. We also note that at *ex situ* SEM images taken after oxidation of Cu at 1.0 V show an increased density of CuO_x nanocubes and evidence of cubes growing on top of each other. Further increasing the potential to 1.1 V resulted in an even higher density of CuO_x nanocubes. The nanocubes now form a very compact layer, although regions with distinct nanocubes can still be clearly observed. At high anodic potentials, 1.1 V, evidence for CuO could clearly be seen in

the Raman spectrum through the appearance of peaks at 290 and 340 cm^{-1}. Reducing the potential from 1.1 V or 0.9 V to -0.6 V resulted in reduction of the Cu_xO layer to metallic Cu as evidenced by the loss of the Raman peaks for CuO and Cu_2O. Therefore, it is clear that electrochemical cycling of the electrode results in the formation of metallic copper nanostructures. It is possible that these nanostructures have a large number of (100) facets which would explain the high selectivity to ethylene, as suggested by *Roberts et al*.[4,37] Another possibility could be that the nanostructuring process creates a large number of grain boundaries and defects, as have been proposed by *Kanan* and co-workers to explain an increase CO2RR activity upon reduction of previously oxidized Cu.[30–32,48,49]

Based on the observations from *in-situ* Raman spectroscopy, SEM observations of surface morphology changes and XPS measurements, we have evidence to support a proposed mechanism of the electrochemical nanostructuring process (see Figure 3.6), which was originally outlined by *Roberts et al.*[13] The presence of the chloride anions is known to promote the corrosion of metallic Cu to form CuCl (Eqn. 3.1).[50–52]

$$Cu_{(s)} + Cl^-_{(aq)} \leftrightarrow CuCl_{(s)} + e^- \quad E = +0.157 \text{ V (vs RHE)} \qquad \text{(Eqn 3.1)}$$

In CO_2-saturated 0.1 M bicarbonate system, the bulk pH is 6.8.[4] At this pH, the thermodynamically stable phase is Cu_2O rather than CuCl according to calculated Pourbaix diagrams.[50] Thus, any CuCl that formed on the electrode surface rapidly converts to Cu_2O according to Eqn. 3.2[50].

$$2\,CuCl_{(s)} + H_2O_{(l)} \rightarrow Cu_2O_{(s)} + 2\,H^+_{(aq)} + 2\,Cl^-_{(aq)} \quad pH > 5.30 \qquad \text{(Eqn 3.2)}$$

The precipitation of Cu_2O from a solution of pH greater than 4 is known to produce cubic structures.[37,39] Application of a negative potential, causes Cu_2O to reduce to metallic Cu according to Eqn. 3.3.[50]

$$Cu_2O_{(s)} + 2\,H^+_{(aq)} + 2\,e^- \leftrightarrow 2\,Cu_{(s)} + H_2O_{(l)} \quad E = 0.471 - 0.059\,pH \qquad \text{(Eqn 3.3)}$$

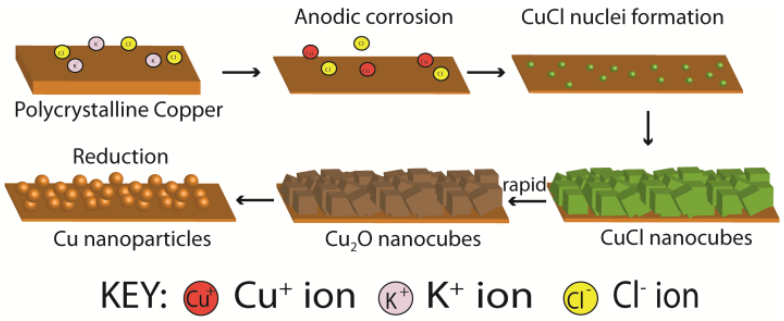

Figure 3.6. Plausible copper nanoparticle growth mechanism.

During electrochemical cycling (Figure 3.2), it was observed that the oxidation current was highest for F^- and lowest with I^-. This pattern can be attributed to differences in the solubilities of the copper halides. When an oxidative potential is applied to Cu in the presence of halide anions (X^-), Cu dissolves and forms CuX, which then precipitates to some extent onto the surface of Cu. However, depending on the identity of the halide anion, the solubility of CuX can vary considerably, which affects the precipitation step. The solubility decreases in the order CuF_2 > CuCl > CuBr > CuI. For example, evidence for dissolved CuCl has been reported, whereas no evidence for dissolved CuBr and CuI has been reported for similar conditions.[52] For the case of F^-, CuF_2 forms because of the inherent instability of CuF.[53–55] The precipitation of the halide and subsequent formation of CuO_x results in the inhibition of further dissolution of the Cu. Since CuF_2 is the most soluble salt, the largest oxidative current was therefore observed when the F^- halide anion was used. This would also mean that electrochemical oxidation with F^- would result in the largest amount of precipitate.

We also investigated the morphology of the CuO_x layer that forms with different halides. It was observed that with the exception of F^-, the CuO_x layer takes on a cubic morphology of similar particle size to that found for cycling in Cl^-. For F^-, rounded nanoparticles were obtained instead, each nanoparticle seemingly composed of numerous nanograins. The density of the CuO_x cubes on the surface are (in order of decreasing density) Cl^- > Br^- > I^- . Therefore, a higher oxidation current would result in a higher density of CuO_x cubes. When the CuO_x was reduced electrochemically, we observed that for all halides, only rounded Cu nanoparticles remained

The key changes upon nanostructuring are an increase in current density and an increased selectivity towards C_2 products. The increase in current density can be explained simply by an effective increase in electrochemical surface area. After nanostructuring the surface, the nanoparticles that cover the surface are expected to have a higher surface area than the previously flat polycrystalline copper surface. The increased C_2 selectivity on the other hand could be due to the exposure of a higher number of Cu(100) facets, which have been previously shown to be more selective for much such products.[1] Another factor could be the introduction of a large number of defects and grain boundaries during the nanostructuring process could serve as highly selective active sites for C_2 product formation as suggested by *Kanan* and co-workers.[49]

3.4 Conclusions

We have shown that the restructuring of polycrystalline Cu that occurs upon cycling from oxidizing to reducing potentials in a potassium halide solution is sensitive to the identity of the

halide anion. The degree of restructuring increases in the order $I^- < Br^- < Cl^- < F^-$, paralleling the increasing solubility of the corresponding copper halide salt. Evidence from Raman spectroscopy suggests that the restructuring of Cu begins with halide induced corrosion and deposition of the copper halide salt once the solubility of the salt is surpassed. The salt crystal then rapidly undergo hydrolysis to form Cu_2O and at higher potentials, CuO. The oxide crystals formed are cubic in shape and when reduced electrochemically results in the formation of irregular Cu nanoparticles (~ 20 nm in diameter) with rounded edges. Irrespective of the halide anion used during the restructuring of Cu, the Cu nanoparticle formed after restructuring exhibit somewhat higher overall electrochemical activity, a reduction in the Faradaic efficiency for H_2 formation and corresponding increase in the Faradaic efficiency for CO_2 reduction. Most notably, restructuring leads to significant suppression in the formation of methane and a corresponding increase in the formation of ethylene, consistent with much of the recent literature[36,37,41] Cycling of the electrode in the presence of chloride, bromide or fluoride anions results in a Faradaic efficiency for ethylene of ~15.2%, a factor of ~1.5 higher than that observed for polycrystalline copper (at -1.0 V vs RHE). Faradaic efficiency for ethanol is enhanced (from 2.65% to ~7.6%).

Chapter 4: Optimizing C-C Coupling on Oxide-derived Copper Catalysts for Electrochemical CO_2 Reduction

4.1 Introduction

Electrochemical reduction of CO_2 to fuels using renewable electrical energy (e.g., generated by solar radiation or wind) is a potential source of sustainable fuel for the future.[28,56] Pursuit of this option has led to considerable interest in discovering electrocatalysts that can promote electrochemical CO_2 reduction (CO_2R) efficiently and with high selectivity to targeted products.[4,57,58] The main bottleneck has been the catalyst itself, as one does not yet exist that can produce chemical fuels at low overpotential and with high selectivity.[2,6,58–60] Of the various metal-based catalysts studied for CO_2R, copper remains the only one capable of producing significant amounts of hydrocarbons and oxygenates.[4,6,57] However, the selectivity to any particular product is not especially high.[3] Clearly, improvements in CO_2R electrocatalysts are required for this process to be viable for producing renewable fuels. In particular, catalysts are desired for producing ethylene and ethanol, which can be readily converted to fuels.[35]

In recent years, a new class of Cu-based catalysts with higher activity, better C_{2+} selectivity and lower overpotential requirements for CO_2R has emerged.[31,32,36,37,49,61–65] These "oxide-derived" catalysts can be prepared via oxidation of Cu via thermal[31,32,49] or electrochemical[37,38] treatments or by exposure to an O_2 plasma.[64] The oxidized Cu is then reduced back to its metallic form. Kanan and coworkers have shown that growth of thick copper oxide layers by thermal oxidation followed by subsequent reduction produces an electrocatalyst that can promote CO_2R at overpotentials less than 0.4 V.[31] Interestingly, when the catalyst is utilized for CO reduction, it is able to generate C_2 and C_3 (C_{2+}) liquid products with up to 57% faradaic efficiency (FE) at an applied potential of only -0.3 V vs RHE.[32] Improved selectivities and lower onset potentials for C_{2+} products also have been reported for oxide-derived catalysts made by electrochemical processing and by chemical treatment of copper oxide nanowires.[31,32,36,37,49,61–65] Oxidation-reduction processing has also been applied to gold and silver, and decreases in the overpotential required for CO_2 reduction to CO have been reported by a number of groups.[30,66–69]

There are two important issues not addressed in previous studies of oxide-derived Cu catalysts. The first is the extent to which the performance of such catalysts is influenced by the manner of catalyst preparation and operation. Of particular interest in the latter context is the extent to which the pH and CO_2 concentration near the electrode affect product selectivity. To address these questions, catalysts prepared by different procedures must be tested under strictly identical conditions and in the same electrochemical cell.[70] The second issue is the identity of the electrolyte cation and its effect on catalyst activity and selectivity.[4,71–74] For example, Hori and coworkers have observed that the size of the alkaline metal cation (Li^+, Na^+, K^+ and Cs^+) influences the ratio of C_2/C_1 products formed on metallic Cu at a fixed current density of 5 mA cm^{-2}.[4,73] Use of Cs^+ as the electrolyte cation as compared to a Li^+ resulted in a higher selectivity to C_{2+} products, lower selectivity to hydrogen evolution (HER) and C_1 products, and a lower applied potential requirement for a fixed current density. Kenis and coworkers observed a similar effect for production of CO by CO_2R on Ag electrodes, finding larger cations yield a higher partial current densities to CO, a lower overpotential for a given current density, and a suppression of the HER.[72]

The present study was undertaken to address the questions posed above. Four representative oxide-derived (OD) copper catalysts were synthesized: "oxide-derived nanocrystalline copper" developed by Kanan and co-workers,[31,32,49] "Cu nanowire arrays" developed by Smith and co-workers,[61] "electrodeposited "copper (I) oxide films" developed by Yeo and co-workers[62] and "electrochemical oxidation-reduction cycled Cu" developed by Nilsson and co-workers.[37] The performance of these catalysts was examined in both $KHCO_3$ and $CsHCO_3$ electrolytes. The information gained from these investigations, combined with detailed structural characterization of the catalysts, allowed us identify how catalyst structure and the conditions chosen for CO_2R affect catalyst activity and C_{2+} product selectivity. These studies reveal that it is possible to achieve a FE as high as 70% for C_{2+} products. This result is achieved by operating the catalysts at current densities that enable attainment of a high electrolyte pH adjacent to the cathode without excessive lowering of the local concentration of CO_2 due to the reaction of CO_2 with OH^- anions to form HCO_3^- and CO_3^{2-} anions. We show that these conditions can be achieved because the kinetics of the reaction of CO_2 with OH^- anions is slow.[75]

4.2 Experimental

Materials: The highest purity reagents were procured wherever possible to mitigate the potential effect of impurities. Cesium carbonate (99.995% metals basis), potassium carbonate (99.995% metals basis), potassium chloride (≥99.9995% metals basis), ammonium persulfate (≥98.0%), sodium hydroxide (99.99% metals basis), lactic acid (≥ 85%), perchloric acid (60%), nitric acid (70%), hydrochloric acid (37%) and sulfuric acid (99.999% metals basis) were purchased from Sigma-Aldrich. Copper foil (0.1mm thick 99.9999% metals basis) and copper (II) sulfate hydrate (99.999% metals basis) were purchased from Alfa Aesar. Phosphoric acid (85.0-87.0% assay) was purchased from J.T. Baker. Gold seal plain microscope glass slides (75 x 25 x 1 mm) were purchased from Electron Microscopy Services. Copper slugs (99.999%) and titanium slugs (99.999%) for electron beam evaporation were purchased from Kurt J. Lesker Company. Selemion AMV anionic exchange membranes were purchased from Asahi Glass Co., Ltd. Nafion proton exchange membranes were purchased from Ion Power Inc. All chemicals were used without further purification. Carbon dioxide (99.995%), nitrogen (99.999%), argon (99.999%) and hydrogen (99.999%) were purchased from Praxair. Hydrogen, argon, nitrogen and carbon dioxide gas purifiers purchased from Valco Instruments Co. Inc were used on the gas feeds to the electrochemical cell and gas chromatograph. 18.2 MΩ deionized (DI) water was produced by a Millipore system.

Preparation of Cu foil: Preparation of Cu foil is similar to that reported in section 3.2.

Preparation of oxide-derived nanocrystalline copper (OD Cu): Preparation of OD Cu via the thermal annealing process was performed according to the procedure of Kanan and co-workers.[31,32,49] Copper foil was first electropolished in concentrated phosphoric acid as described above. The electropolished copper foil was then placed in a muffle furnace, which was heated from room temperature to 500 °C at a rate of 10 °C min^{-1} under an air atmosphere. The temperature was maintained at 500 °C for 1 h, which generated a thick oxide, containing both Cu_2O and CuO, on the surface of the foil. The copper foil was then allowed to gradually cool to room temperature. The copper oxide layer was then electrochemically reduced before electrolysis by applying a potential of -1.2 V vs Ag/AgCl in Ar sparged 0.1 M $KHCO_3$ (pH 8.3) until complete reduction had taken place (assumed to be when the current density reached a steady state).

Preparation of Cu nanowire arrays (OD NWs): Preparation of OD NWs was performed according to the procedure of Smith and co-workers.[61] Copper foil was first electropolished in concentrated phosphoric acid as described above. The copper foil was then soaked in an aqueous solution containing 0.133 M ammonium persulfate and 2.667 M sodium hydroxide to generate a $CuO/Cu(OH)_2$ nanowire array on the surface. Copper foils were soaked for varying times (75s, 150s, 300s and 600s), with a longer soaking time generating a denser and longer nanowire array. The copper foils were then rinsed copiously with DI water and dried with a stream of nitrogen. To obtain CuO nanowire arrays, the copper foils were placed in a muffle furnace, which was then heated from room temperature to 150 °C at a rate of 5 °C min^{-1} under an air atmosphere for 2 hours. The CuO nanowire arrays were then reduced electrochemically before electrolysis by applying a potential of -1.2 V vs Ag/AgCl until complete reduction had taken place (assumed to be when the current density reached a steady state).

Preparation of electrochemically cycled copper (EC Cu): Preparation of EC Cu was performed according to the procedure of Nilsson and co-workers with some modifications.[37,38] Copper foil was first electropolished in concentrated phosphoric acid as described above. Electrochemical oxidation-reduction cycling of the copper foil was then carried out in a 3 electrode system with another copper foil as the working electrode, Pt as the counter electrode and 0.1 M $KHCO_3$ solution containing 16 mM of KCl as the electrolyte. The electrolyte was first saturated with CO_2 and the potential was swept from open circuit voltage to 0.2 V vs Ag/AgCl and then to -1.2 V vs Ag/AgCl for 1 cycle at a rate of 20 mV s^{-1}. Sweeping to oxidative potentials generates a Cu_2O layer on the surface, which is then subsequently reduced back to metallic Cu at reductive potentials. The copper foil was then rinsed copiously with DI water and dried with a stream of nitrogen.

Preparation of reduced electrodeposited Cu(I) oxide films (EOD Cu): Preparation of EOD Cu was performed according to the procedure of Yeo and co-workers with some modifications.[62] Glass slides (75 x 25 x 1 mm) were first cleaned in a custom-made O_2 plasma system for 1 minute and subsequently sonicated in DI water for 10 minutes. The slides were then loaded into an electron beam evaporator where 40 nm of Ti (adhesion layer) and subsequently 100 nm of Cu were deposited. Cu_2O was then electrochemically deposited onto the Cu film (cathode) using a 2 electrode system with a Cu foil as the counter electrode (anode) and an aqueous solution containing 0.3 M $CuSO_4$, 3.2 M NaOH and 2.3 M lactic acid as the electrolyte. Electrodeposition was performed in a glass cell and the temperature was controlled with a water bath held at 60 °C with agitation created using a magnetic stirrer. A constant current density of -1.82 mA cm^{-2} was used for deposition and different thicknesses of Cu_2O were produced by varying the deposition time (50 s, 100 s, 200 s, and 300 s). The Cu_2O layer was then reduced electrochemically before electrolysis by applying a potential of -1.2 V vs Ag/AgCl until complete reduction had taken place.

Electrochemical measurements and product analysis: Procedures for these are identical to that described in section 3.2.

Investigation of the effects of CO_2 partial pressure: To study the effects of reduced CO_2 partial pressures on the selectivity and current density of Cu foil, 6 different mixtures of Ar and CO_2 were used (0, 0.2, 0.4, 0.6, 0.8 and 1.0 atm CO_2). For example, to obtain 0.6 atm of CO_2, a flowrate of 3 sccm of CO_2 and 2 sccm of Ar was selected and used to saturate the 0.1 M $CsHCO_3$ electrolyte in the electrochemical cell for at least 15 minutes. Besides changing the purge gas, all other experimental procedures were identical to those described above.

4.3 Results and discussion

Structural characterization: SEM images of the each of the four oxide-derived copper catalysts (OD Cu, OD NWs, EC Cu and EOD Cu) in their reduced state are shown in Figure 4.1. For OD NWs, the length and density of the nanowire array can be tuned by varying the length of the chemical treatment step. The OD NWs shown in Figure 4.1 were treated for 150 s and will be referred to as OD NWs 150s. Similarly, the thickness of the oxide layer for EOD Cu can be adjusted by changing the electrodeposition time. The EOD Cu shown in Figure 4.1 was prepared by electrodepositing Cu_2O for 100 s and will be referred to as EOD Cu 100s.

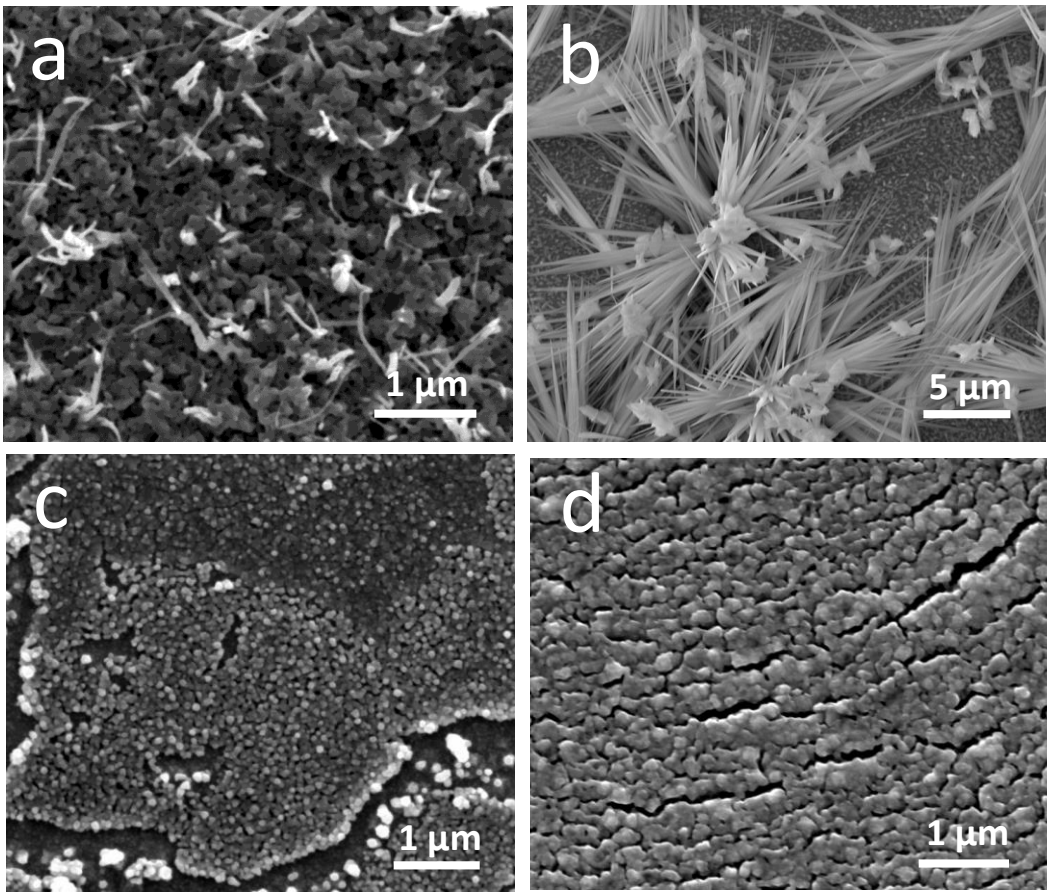

Figure 4.1 SEM images of oxide-derived catalysts after reduction: (a) OD Cu; (b) OD NWs 150s; (c) EC Cu and (d) EOD Cu 100s. Note the larger scale bar for OD NWs.

Oxide-derived nanocrystalline copper (OD Cu), Figure 4.1a, consists of a porous and aggregated structure made up of nanocrystalline copper grains with nanowire-like appendages protruding from the surface. Oxide-derived Cu nanowires (OD NWs 150s), Figure 4.1b, presents a morphology consisting of long and dense nanowires emanating from nucleation sites on the surface. Electrochemically cycled copper (EC Cu), Figure 4.1c, consists of large islands of agglomerated round nanoparticles which are interconnected and appear nanocrystalline. Reduced

electrochemically deposited copper oxide (EOD Cu 100s), Figure 4.1d, also consists of agglomerated round nanoparticles and the morphology appears to be the most uniform compared to the other catalysts.

Overview of CO_2 reduction measurements: The activity of the catalysts (including Cu foil as control) was tested in 0.1 M $KHCO_3$ (K^+ electrolyte) and 0.1 M $CsHCO_3$ (Cs^+ electrolyte). Previous reports have shown that optimal C-C coupling activity occurs in the range from ~ -0.7 V to -1.0 V vs RHE and we therefore chose to test the catalysts in this applied voltage range.[6,61,62,64,76] All catalysts were tested for 70 min at -0.7, -0.8, -0.9 and -1.0 V vs RHE. For each catalyst, cation and applied voltage condition, the analysis was performed 3 times to insure the reproducibility and fidelity of the data.

Role of electrolyte cation on C-C coupling: For EOD Cu and OD NWs, the processing conditions allows for some control over the morphology. We used the conditions which produced the highest C_{2+} selectivity (EOD 100s and OD NWs 150s) for the comparison with the other two preparations. Figure 4.2 summarizes the C_{2+} selectivity of the 4 oxide-derived Cu catalysts at each of the applied potentials in both the K^+ electrolyte and Cs^+ electrolyte (solid blue and green bars). Current density is shown by points referenced to the right hand axis.

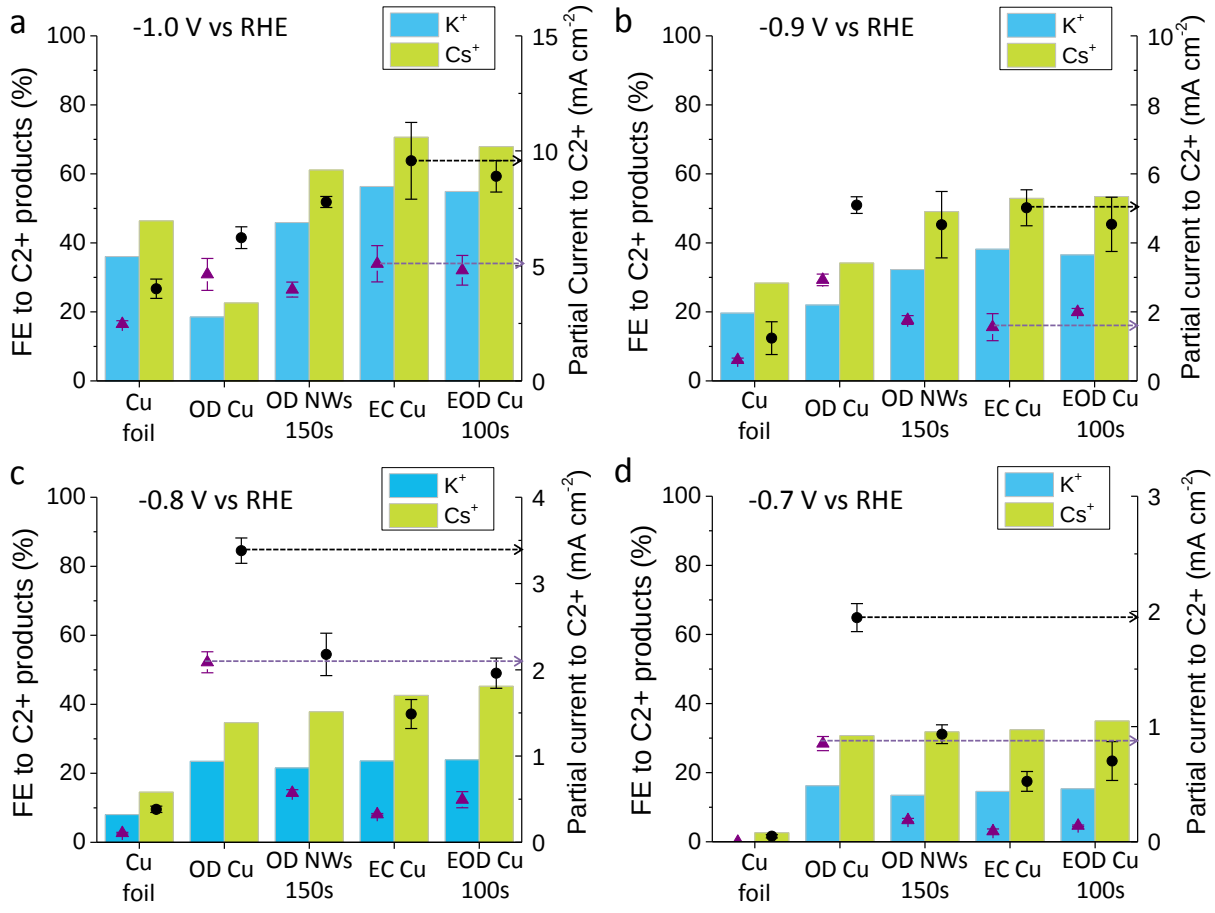

Figure 4.2 Faradaic efficiencies and partial current densities towards C_{2+} products for catalysts tested in both K^+ electrolyte and Cs^+ electrolyte: (a) -1.0 V vs RHE (b) -0.9 V vs RHE; (c) -0.8 V

vs RHE (d) -0.7 V vs RHE. Purple triangles and black circles correspond to partial current density values to C_{2+} products for samples tested in K^+ electrolyte and Cs^+ electrolyte respectively. Bar graphs correspond to faradaic efficiency values (blue, K^+ electrolyte; green, Cs^+ electrolyte).

The most striking observation in Figure 4.2 is that for all of the catalysts (including Cu foil), higher selectivity and partial current densities toward C_{2+} products can be attained using a Cs^+ electrolyte compared to a K^+ electrolyte at all applied potentials. Also, it appears that the selectivity for production of C_{2+} products for most of the catalysts peaks at -1.0 V vs. RHE regardless of the cation used, which is in agreement with previous reports.[6,61,62] The increase in C_{2+} selectivity for Cu foil with the larger cation is also consistent with prior reports;[71,73] it is interesting that increases are also seen for the nanostructured Cu electrocatalysts. Focusing on Figure 4.2a, which contains the data for a bias of -1.0 vs. RHE, the C_{2+} product selectivity is highest for EC Cu at 70.6% (±2.24), followed by EOD Cu 100s at 68.5% (±5.00), OD NWs at 61.1% (±6.18), Cu foil at 46.4% (±1.18) and finally OD Cu at only 22.6% (±1.50).

Regardless of the cation used, nearly all variants of oxide-derived catalysts perform better at all potentials than the Cu foil control sample, which is also consistent with previous studies of oxide-derived copper.[31,37,38,61,62] The exception is OD Cu operated at -1.0 V, which has a lower selectivity; we believe this is due to mass transport limitations due to its inherent high surface area, which will be discussed in more detail below. Again, with the exception of OD Cu, the selectivity towards C_{2+} products decreases at less negative applied potentials. At -0.9 V and -0.8 V vs. RHE, EC Cu and EOD Cu 100s remain the best performers and boast a C_{2+} selectivity of >50% and >40% at these two potentials. At the lowest tested overpotential of -0.7 V vs. RHE, the C_{2+} selectivity in Cs^+ electrolyte of all the oxide-derived catalysts remains relatively high, >30%. This contrasts with copper foil which has a very low FE for C_{2+} products in Cs^+ electrolyte and appears not to yield any C_{2+} products in K+. Intriguingly, at -0.7 V vs. RHE, the C_{2+} selectivity for all the oxide-derived catalysts seem to converge at ~30% in Cs^+ electrolyte and ~15% in K^+ electrolyte.

Another benefit of enhancing the selectivity towards C_{2+} products is the suppression of C_1 products. From -0.7 V to -1.0 V, use of Cs^+ appears to suppress the formation of C_1 products such as CO, $HCOO^-$ and CH_4. At a potential of -1.0 V on EC Cu for example, only 3.25% selectivity towards C_1 products was observed with Cs^+ electrolyte compared to 12.0% with K^+ electrolyte at the same potential. Similar trends were observed for all other oxide-derived catalysts. The most pronounced suppression of C_1 products was observed with OD Cu at -1.0 V in Cs^+ electrolyte as only 0.46% selectivity to C_1 products was observed.

Product distribution with Cs^+ electrolyte: Next, we look in detail at the product distributions as a function of applied potential with Cs^+ electrolyte for the different oxide-derived catalysts as shown in Figure 4.3. At the potential of -1.0 V, EC Cu exhibits the lowest selectivity to hydrogen evolution at 23.7%, followed by EOD Cu 100s at 25.0%, OD NWs 150s at 34.8%, Cu foil at 30.3% and finally OD Cu at 74.6%. The selectivity to hydrogen increases at decreased overpotentials (OD Cu is an exception), which follows the trend of the Cu foil control, Fig. 3e. A characteristic of oxide-derived catalysts is the suppression of the reaction pathway towards methane compared to Cu foil; this effect is more pronounced with the use of a Cs^+ electrolyte. For example, at -1.0 V vs. RHE, Cu foil exhibits a selectivity of 9.74% towards methane whereas this value is <3% for all variants of oxide-derived copper. Looking at the distribution of C_{2+} products, it appears that ethylene and ethanol are the most dominant. For example, EC Cu has a selectivity of 45.0% and

17.5% for ethylene and ethanol, respectively, at -1.0 V. For the same catalyst and potential, only 0.93% selectivity towards methane was observed.

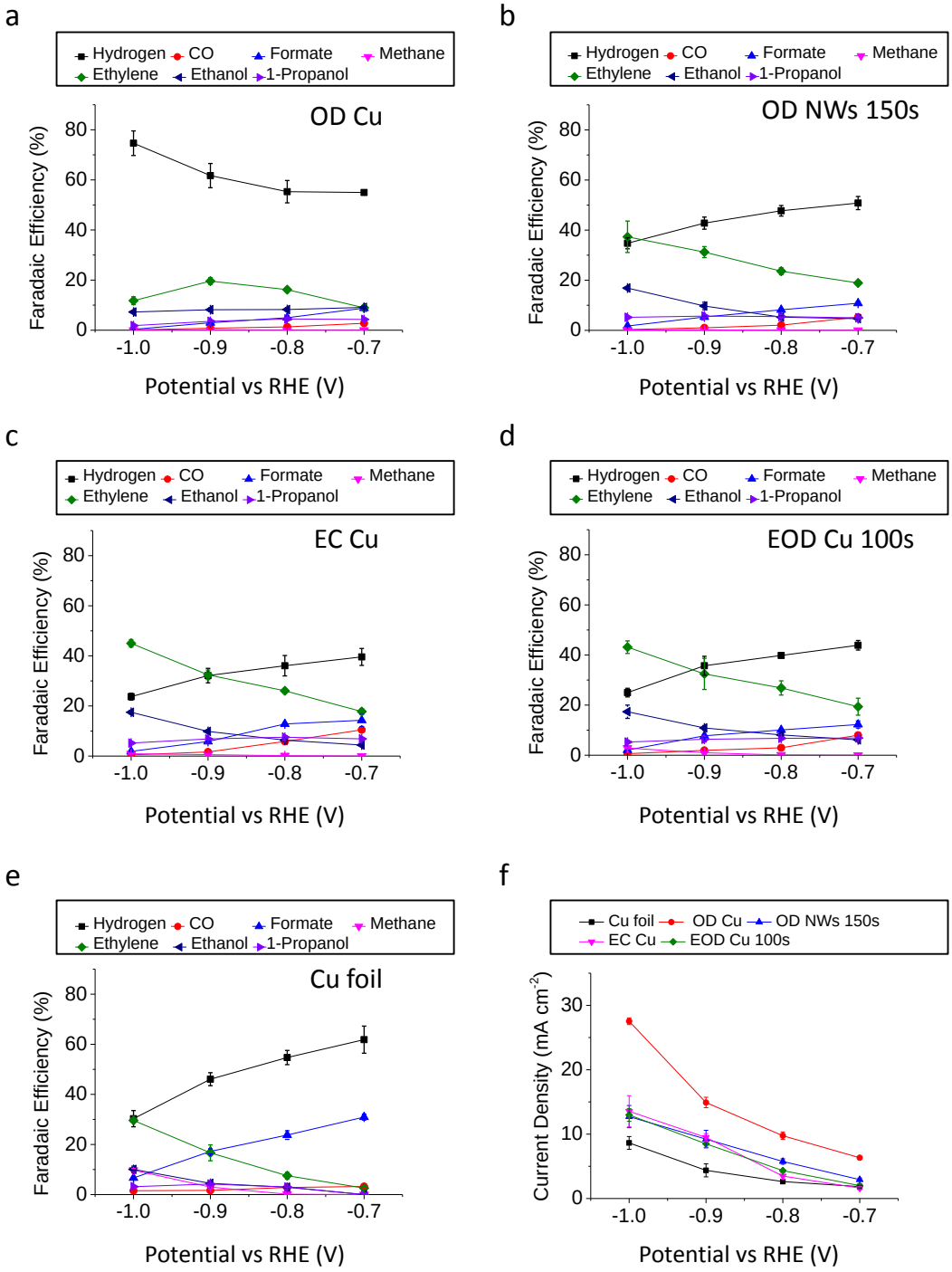

Figure 4.3 Faradaic efficiencies of major CO2R products from -0.7 V to -1.0 V vs RHE in 0.1 M $CsHCO_3$ for: (a) OD Cu; (b) OD NWs 150s; (c) EC Cu, (d) EOD Cu 100s and (e) Cu foil. Current densities from -0.7 V to -1.0 V vs RHE for each catalyst are shown in (f). More detailed faradaic efficiency and current density data are available in the supporting information.

For all catalysts and potentials, it appears that whenever high ethylene selectivity is observed, high ethanol selectivity is observed as well. This is consistent with measurements made by Jaramillo and co-workers on Cu foil,[6] which suggest that C_2 products follow similar initial reaction pathways, although it is not yet entirely clear what determines their branching ratios.[77] Intriguingly, the selectivity towards minor products such as 1-propanol, allyl alcohol and propionaldehyde seems to be lowest at -1.0 V. The maximum selectivity for these products occurs at less negative applied potentials, -0.9 V or -0.8 V (depending on catalyst), which is qualitatively consistent with results from Jaramillo and co-workers on Cu foil in 0.1 M $KHCO_3$.[6] For example, with EC Cu at -0.7 V, the selectivity to 1-propanol is 6.87%, which makes up 21.2% of the total C_{2+} being produced. On the other hand at -1.0 V, 1-propanol only makes up 7.37% of the total C_{2+} composition. Ethylene and ethanol make up 88.5% of total C_{2+} products at -1.0 V; this suggests that at higher overpotentials C-C coupling reaction pathways favor ethylene and ethanol over other minor products.

Finally, the composition of the C_{2+} products as a function of potential for all catalysts in Cs^+ electrolyte and K^+ electrolyte was also determined and it appears that changing the cation enhances all C-C coupled products equally, with no significant change of the C_{2+} product composition. This suggests that the larger Cs^+ cation enhances the initial C-C coupling step (which explains the suppression of methane) but has little effect on the subsequent steps of the reaction pathways.

Comparison of oxide-derived catalyst activity for CO_2R: The careful benchmarking of the CO_2R activity of the oxide-derived Cu catalysts not only allows a quantitative comparison of their activities but also enables insight into how they produce enhanced C_{2+} product yields. A number of factors including surface facet orientation and grain boundaries are believed to affect the selectivity of copper catalysts towards C_{2+} products. For example, the Cu (100) surface has been shown to have particularly high selectivity towards ethylene, whereas the Cu (111) surface has been shown to favor methane formation.[59,78] Kanan and coworkers have shown that grain boundaries are highly active sites for C-C coupling and removal of these sites result in loss of selectivity towards C_{2+} products.[79] Also, work by Yeo and coworkers has shown that having a smaller crystallite size and therefore more grain boundaries appear to increase the selectivity towards ethylene.[80] Indeed from the SEM images, it appears that the samples are mostly composed of nanocrystalline, agglomerated particles suggesting a higher density of grain boundaries compared to polycrystalline copper.

The high density of grain boundaries and absence of a preferred orientation would lead to a prediction of similar selectivity towards C_{2+} products for the catalysts compared in this study. Indeed, the selectivity towards C_{2+} products is very similar at the lowest applied potential of -0.7 V. However at higher overpotentials, the selectivity of the catalysts diverges. Notably, OD Cu produces mostly hydrogen at -1.0 V vs. RHE while the other catalysts produce >60% C_{2+} products. We hypothesized that the reason for this difference is that at very negative applied potentials, higher surface area leads to a mass transfer bottleneck for the CO_2 reactant. However at less negative applied potentials, the current density is much lower and thus depletion of CO_2 and the associated concentration polarization effects at the catalyst surface are less severe.[81] To test this hypothesis we performed a series of experiments using morphology tuning afforded by the EOD Cu synthesis method.

Role of surface area: EOD Cu samples were made with different electrodeposition times: EOD Cu 50s, EOD Cu 200s and EOD Cu 300s, with a longer deposition time leading to a thicker Cu_2O

layer. After reduction to the metallic state, the roughness factor (RF) was measured. As expected, increasing the electrodeposition time for EOD Cu increases the RF. A range of about a factor of two was obtained: 12.8, 17.0, 20.9 and 24.0 for 50s, 100s, 200s and 300s respectively. The H_2, C_{2+} and C_1 FEs and current densities obtained in Cs^+ electrolyte for this set of samples are shown in Figure 4.4.

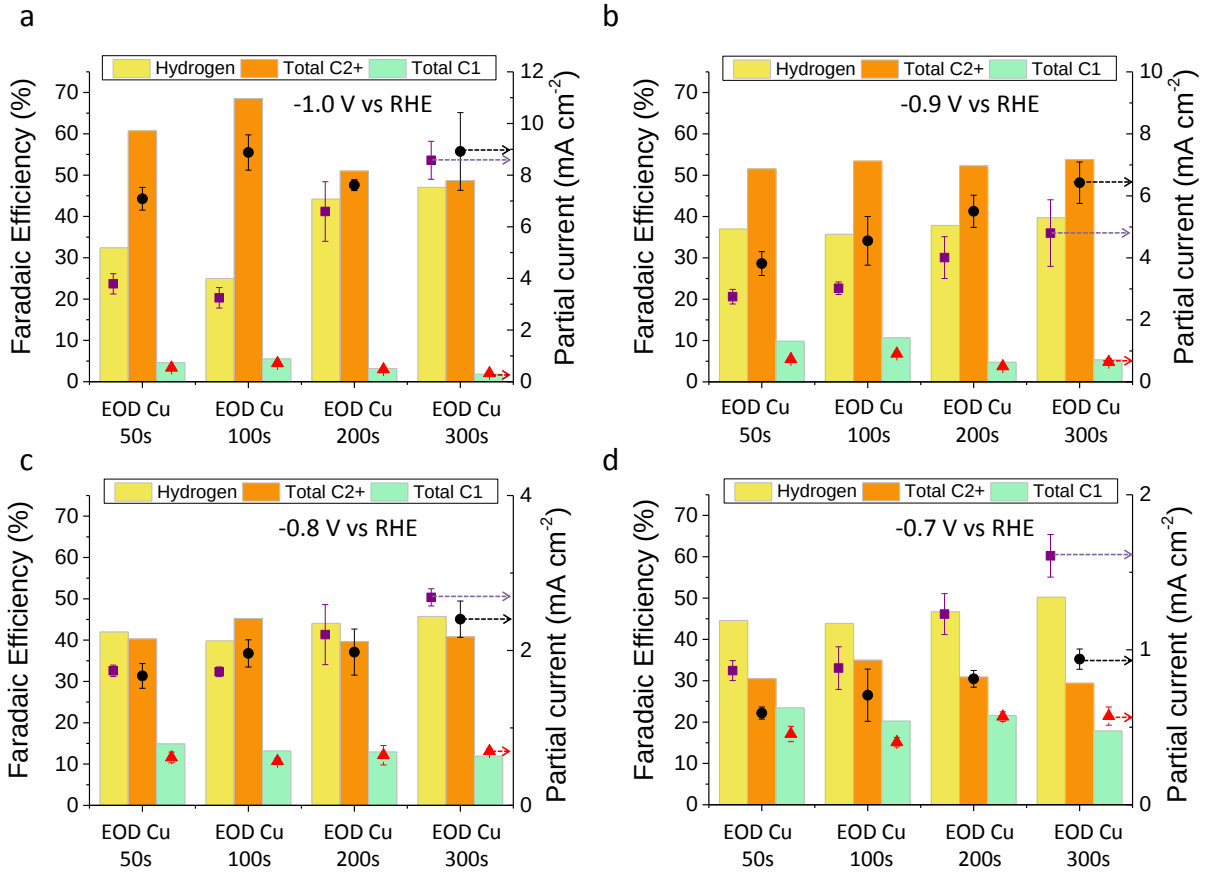

Figure 4.4 Faradaic efficiencies and geometric partial currents towards H_2, C_{2+} products and C_1 products for different thicknesses of electrodeposited Cu oxide layer tested in Cs^+ electrolyte at different applied potentials: (a) -1.0 V vs RHE (b) -0.9 V vs RHE; (c) -0.8 V vs RHE (d) -0.7 V vs RHE. Purple squares, black circles and red triangles correspond to H_2, C_{2+} and C_1 partial current density values respectively. Bar graphs correspond to faradaic efficiency values of H_2 (yellow), C_{2+} products (orange) and C_1 products (green).

For the smaller overpotentials, the EOD Cu electrocatalysts have similar product distributions, independent of their roughness factor. However, at the most negative applied potential of -1.0 V, where the current density and consumption of CO_2 is the highest, it is apparent that there is an optimum RF where selectivity and partial current density to C_{2+} products is highest, which corresponds to that of EOD Cu 100s. On the other hand, at this same potential at -1.0 V, selectivity and partial current density towards C_1 products decrease with increasing RF (Figure 4.4). These trends seem to be consistent with results from Yeo and coworkers in K^+ electrolyte, where they

also observed an optimal RF for enhancing C_{2+} products and suppressing hydrogen as well as a decrease in C_1 products with increasing RF.[62] At lower potentials, the C_{2+} selectivity for all samples appears to be similar, although the partial current density increases with higher RF samples due to their higher surface area (roughness factor). Interestingly, in going from -1.0 V to -0.9 V, the selectivity to hydrogen for the higher RF samples (200s and 300s) actually decreases, which is opposite to what was observed for the thinner samples (50s and 100s).

Relationship between selectivity, CO_2 mass transport and local pH: A consistent explanation of the observation of an optimal RF for maximizing C-C coupling (within a given synthesis scheme) can be provided by considering the competing effects of local pH and CO_2 concentration. CO_2 reduction consumes hydrogen ions from water and releases hydroxide anions, leading to an increase in the pH near the cathode surface. The higher geometrical current densities for the high surface area catalysts magnify this effect.[33,61–63]

The effect of pH on the product distribution for both CO_2 and CO reduction on Cu electrodes has been studied experimentally. Koper and coworkers[82,83] and Nilsson and coworkers[38] have shown that at high pH, C-C coupling of CO occurs at lower overpotentials on the RHE scale than at low pH. In this case, both sets of investigators demonstrate that ethylene formation occurs at lower onset potentials on the RHE scale in more basic (pH 13) as compared to neutral (pH 7) conditions. These observations are relevant because the reduction of CO_2 to ethylene proceeds via the formation of CO. It is also notable that if the experimental results are represented on the SHE scale there is no effect of pH, indicating that the C-C bond formation does not involve change transfer.[84] Recent theoretical work by Goddard and co-workers also suggests that at high pH, pathways to CH_4 are blocked kinetically and are therefore suppressed.[85] C-C bond formation is unaffected by pH and consequently the kinetically dominant pathway at high pH is CO-CO coupling, the first step along the path to ethylene.[85]

During CO_2R, depending on the catalyst morphology, mass transfer conditions and buffering capacity of the electrolyte, the surface pH can rise above the bulk pH, as has been shown previously by simulation.[81,86] Indeed, this rise in surface pH has been proposed to be the reason for high C_{2+} product selectivity on high surface area copper electrodes.[41,61–63] However, the OH^- anions that are generated can concurrently react with CO_2 to form HCO_3^- and CO_3^{2-} anion and thereby reduce the CO_2 concentration at the cathode.[4,81,86] Therefore, if the pH at the cathode surface is too large, the concentration of CO_2 at the cathode is lowered, which leads to an inhibition in the rate of CO_2R. We note here that the approach to equilibrium is highly dependent on the kinetics of the reaction of CO_2 and OH^- anions to form HCO_3^- and CO_3^{2-} anions.

The trade-off between increasing surface pH, which can contribute to the net enhancement in the rate of C-C coupling, and decreasing CO_2 concentration suggests that there should be an optimal value of the RF for the oxide-derived catalysts to perform optimally. If the RF is too high, then the electroactive surfaces will be in an environment where dissolved CO_2 is depleted and H_2O is the only available reactant. In the other words, we can impede transport slightly by using a thicker structure, resulting in a higher pH that can help increase selectivity. However, care must be taken not to exceed an certain optimal thickness value as CO_2 transport limitations can come into play, leading to lower selectivity. This scenario appears to be occurring on OD Cu (RF = 103) as hydrogen evolution dominates its activity at -1.0 V vs RHE (Fig 4.3a). Also, in contrast to the other electrocatalysts, hydrogen selectivity decreases with more positive applied overpotential; this is due to the reduction in current density (see Fig. 4.3f), which in turn reduces the deleterious

effect of CO_2 mass transport limitations. We propose that this is the reason that similar product selectivity is exhibited by all oxide-derived samples at -0.7 V (Figure 4.1), where mass transport limitations are expected to have a less significant. Similarly, we observe this effect to be less significant for EOD Cu 200s and EOD Cu 300s, which have RF values of 20.9 and 24.0 respectively. The optimum RF value would therefore be able to induce a high local pH, but not so high as to lead to CO_2 mass transport limitations.

As a result of this analysis, we hypothesized that for catalysts with optimum RF values, reducing the CO_2 concentration should reduce the selectivity towards C_{2+} products and increase the hydrogen selectivity. On the other hand, increasing the CO_2 supply for catalysts with high RF values would be expected to improve selectivity towards C_{2+} products and decrease the hydrogen selectivity. To investigate the first idea, we tested EOD Cu 100s at -1.0 V vs RHE at lower partial pressures of CO_2: 0.8 and 0.6 atm, balanced to 1 atm with Ar. As shown in Figure 4.5, lowering the CO_2 partial pressure from 1.0 to 0.6 atm does indeed result in a decrease in C_{2+} selectivity from 68.5% to 56.2%. Furthermore, the hydrogen selectivity increases from 25.0% to 37.1%.

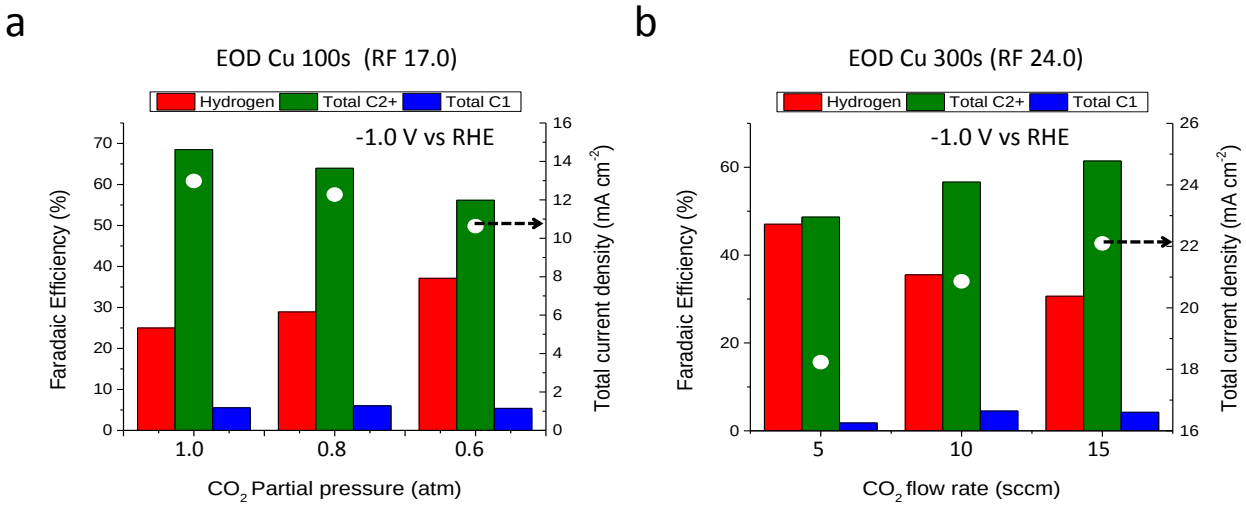

Figure 4.5 Faradaic efficiencies and partial current densities towards H_2, C_{2+} products and C_1 products at -1.0 V vs RHE for: (a) EOD Cu 100s with different CO_2 partial pressures and (b) EOD Cu 300s with different flow rates of CO_2. A lower CO_2 partial pressure results in a lower concentration of dissolved CO_2, while a higher flow rate results in a smaller mass-transfer boundary layer thickness. White circles correspond to total current density values. Bar graphs correspond to faradaic efficiency values.

To increase the CO_2 supply for high RF catalysts, the thickness of the mass-transfer boundary layer can be reduced by increasing the CO_2 flow rate convection to the electrochemical cell. The performance of EOD Cu 300s was measured at flow rates of 10 and 15 sccm for a potential of -1.0 V vs RHE (all experiments reported thus far were carried out at a flow rate of 5 sccm). As shown in Figure 4.5b, decreasing the mass-transfer boundary layer thickness causes the C_{2+} selectivity to increase from 48.7% at 5 sccm to 61.4% at 15 sccm. At the same time the hydrogen selectivity decreases from 47.0% at 5 sccm to 30.7% at 15 sccm. The current density and hydrogen selectivity were not affected by increasing the flow rate because the catalyst was not limited by the availability of CO_2 at 5 sccm. However, at the higher flow rates a small increase in C_1

selectivity and a small decrease in C_2 selectivity were observed, which we attribute to the decreased mass-transfer boundary layer thickness somewhat mitigating the rise in the local pH. As discussed above, theoretical studies suggest that the increase in pH will suppress the formation of CH_4 relative to C_{2+} products.[85]

Numerical modeling of oxide-derived catalysts: The explanations for our experimental observations have been based on the competition between the local pH rise which aids C-C coupling and depletion of CO_2 which can reduce C_{2+} selectivity. To gain a deeper insight into these effects, we calculated the average surface pH as well as the average CO_2 concentration at the surface of the catalysts using an approach similar to that described by Gupta et al.[86]

In this model, the catalyst is assumed to be flat regardless of its true morphology. However, we note that a highly porous/textured surface should impede mass transport more than a flat surface, resulting in a higher pH and lower CO_2 concentration than calculated. Furthermore, these conditions would possibly result in non-uniform surface conditions across all the electroactive areas due to differences in the porosity/texturing on the nanoscale. Also, migration effects were not included because previous simulations indicated that this effect was not significant.

Although a model including these effects would allow for the most accurate calculations of the exact surface conditions, this would be beyond the scope of the present work because the non-uniform nature of our catalysts adds a layer of complexity on this problem. The flat surface assumption would be a reasonable approximation as this allows us to qualitatively compare catalysts from one another, which is the most critical component for optimization of C_{2+} product selectivity.

Table 4.1 summarizes all the possible equilibrium reactions that occur involving H^+, OH^-, HCO_3^-, CO_3^{2-}, H_2O and dissolved CO_2. Table 4.2 shows the diffusion coefficients of the relevant species involved in CO_2 reduction. Table 4.3 shows the number of electrons and carbon dioxide molecules consumed as well as number of hydroxide ions created when one molecule of a particular product is created. Equations 1 to 8 are the partial differential equations and boundary conditions used to model the system.

Table 4.1: Reactions governing the acid-base equilibria during CO_2R. Equations for the equilibrium constants as well as their values are also shown in the table. Note: We do not take into dissolved H_2CO_3 into consideration because this value is very small compared to dissolved CO_2. Furthermore, we only consider the dominant reactions relevant in basic conditions.

Reaction	Equilibrium constant	Values
$CO_2(g) \leftrightarrow CO_2(aq)$	$K_H = \frac{[CO_2(aq)]}{[CO_2(g)]}$ $(Henry's\ Law)$	3.35×10^{-2} M atm^{-1}

$CO_2(aq) + OH^-(aq) \leftrightarrow HCO_3^-(aq)$	$K_1 = \frac{k_{1f}}{k_{1r}} = \frac{[HCO_3^-]}{[CO_2(aq)][OH^-]}$	$K_1 = 4.44 \times 10^7\ M^{-1}$ $k_{1f} = 5.93 \times 10^3\ M^{-1}\ s^{-1}$ $k_{1r} = 1.34x10^{-4}\ s^{-1}$
$HCO_3^-(aq) + OH^-(aq) \leftrightarrow CO_3^{2-}(aq) + H_2O(l)$	$K_2 = \frac{k_{2f}}{k_{2r}} = \frac{[CO_3^{2-}]}{[HCO_3^-][OH^-]}$	$K_2 = 4.66x10^3\ M^{-1}$ $k_{2f} = 1.00x10^8\ M^{-1}\ s^{-1}$ $k_{2r} = 2.15x10^4\ s^{-1}$

Table 4.2: Diffusion coefficients for CO_2R relevant species at 25 °C in water.[86]

Species	CO_2	HCO_3^-	CO_3^{2-}	OH^-
Diffusion coefficient ($m^2\ s^{-1}$)	1.91×10^{-9}	9.23×10^{-10}	1.19×10^{-9}	5.27×10^{-9}

Table 4.3: CO_2/electrons consumed and OH^- generated for various products of CO_2R[6]

Product	CO_2 consumed	Electrons consumed	OH^- generated	Electrons per CO_2	OH^- per CO_2
Hydrogen	0	$2e^-$	2	N/A	N/A
Carbon monoxide	1	$2e^-$	2	2	2
Formate	1	$2e^-$	1	2	1
Methane	1	$8e^-$	8	8	8
Ethylene	2	$12e^-$	12	6	6
Ethanol	2	$12e^-$	12	6	6
1-Propanol	3	$18e^-$	18	6	6

Consider the CO_2 reaction diffusion system in basic conditions and with no migration, we can write a system consisting of 4 partial differential equations[86]:

$$\frac{\partial[CO_2]}{\partial t} = D_{CO_2}\frac{\partial^2[CO_2]}{\partial x^2} - k_{1f}[CO_2][OH^-] + k_{1r}[HCO_3^-] \quad (1)$$

$$\frac{\partial[HCO_3^-]}{\partial t} = D_{HCO_3^-}\frac{\partial^2[HCO_3^-]}{\partial x^2} + k_{1f}[CO_2][OH^-] - k_{1r}[HCO_3^-] - k_{2f}[HCO_3^-][OH^-] + k_{2r}[CO_3^{2-}] \quad (2)$$

$$\frac{\partial[CO_3^{2-}]}{\partial t} = D_{CO_3^{2-}}\frac{\partial^2[CO_3^{2-}]}{\partial x^2} + k_{2f}[HCO_3^-][OH^-] - k_{2r}[CO_3^{2-}] \quad (3)$$

$$\frac{\partial[OH^-]}{\partial t} = D_{OH^-}\frac{\partial^2[OH^-]}{\partial x^2} - k_{1f}[CO_2][OH^-] + k_{1r}[HCO_3^-] - k_{2f}[HCO_3^-][OH^-] + k_{2r}[CO_3^{2-}] \quad (4)$$

Now, we have the following boundary conditions at the electrode surface (x=0)[86]:

$$D_{CO2}\frac{d[CO_2(aq)]}{\partial x} = Rate\ of\ consumption\ of\ CO_2 \quad (5)$$

$$D_{HCO_3^-}\frac{d[HCO_3^-(aq)]}{\partial x} = 0 \quad (6)$$

$$D_{CO_3^{2-}}\frac{d[CO_3^{2-}(aq)]}{\partial x} = 0 \quad (7)$$

$$D_{CO2}\frac{d[OH^-]}{\partial x} = Rate\ of\ OH^-\ generation \quad (8)$$

At x =δ, the concentration of all the species is set to be identical to that of the bulk. This serves as our final set of boundary conditions. These equations were then solved using COMSOL Multiphysics 5.1 to obtain information regarding the pH as well as CO_2 concentration in the mass-transfer boundary layer.

The experimental rate of CO_2 consumption and OH^- generation for each oxide-derived catalyst at each potential can be calculated based on the geometric current density and product distribution. This information is used as an input to the model. The kinetics of the reaction of OH^- with CO_2 or with bicarbonate anions are described by the forward and reverse rate coefficients for these reactions. The mass-transfer boundary layer thickness used in the model was determined experimentally by measuring the limiting current density of the reduction of $Fe(CN)_4^{3-}$ under identical hydrodynamic conditions and is about 100 µm.

The average surface CO_2 concentration and average surface pH were calculated for OD Cu, EC Cu, OD NWs (75s to 600s) and EOD Cu (50s to 300s) at -1.0 V and -0.7 V vs RHE (from Figure 4.2) and the results together with their respective experimental C_{2+} selectivity are shown in Figure 4.6. For all cases, the experimentally determined geometric current densities and the respective product distribution were used to calculate the CO_2 consumption rate and OH^- generation rate as inputs to the model.

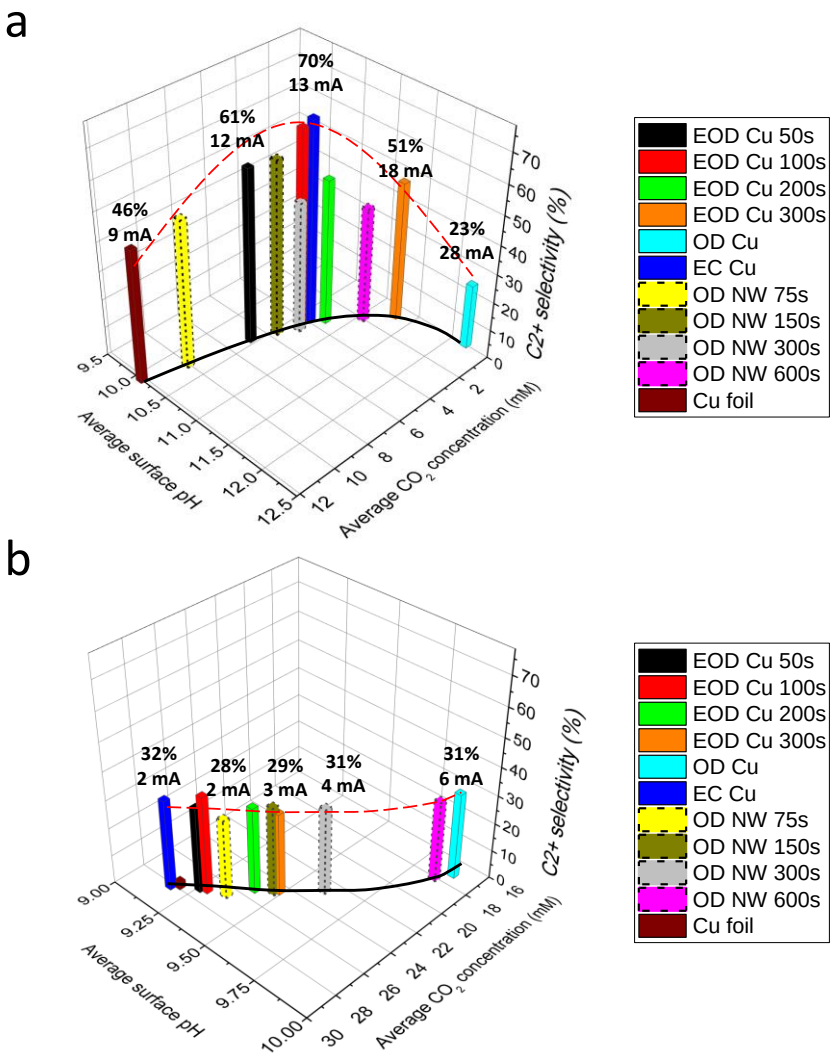

Figure 4.6 Numerical simulation results of the average CO_2 concentration and average surface pH of the various oxide derived catalysts for: (a) oxide-derived catalysts at -1.0 V vs RHE and (b)

oxide-derived catalysts at -0.7 V vs RHE. Average surface pH and average CO_2 concentrations are represented on the horizontal axes. C_{2+} selectivity is represented on the vertical axis. The bars representing the OD NWs system have dashed borders. The relationship between CO_2 concentration and pH is represented by the black curve. The red dashed curve is a guide to eye representing the C_{2+} selectivity of the various catalysts. The C_{2+} selectivity as well as the current density (given in mA per 1 cm^2 geometric area) is given at selected locations.

The solid black curve in Figure 4.6a illustrates the calculated relationship between the average CO_2 concentration and the pH near the cathode surface. The variation in the current density is also shown for selected locations on this curve, with the surface pH increasing and CO_2 concentration decreasing with increasing current density. The height of the bars gives the C_{2+} product selectivity and the red dashed curve, drawn as a guide for the eye, represents the variation in C_{2+} product selectivity as a function of the cathode surface pH and CO_2 concentration. For an applied voltage of -1 V vs RHE, a maximum in the C_{2+} product selectivity is observed peak for a pH of ~ 10.6 and a CO_2 surface concentration of ~ 4.1 mM, corresponding to a current density of ~13.3 mA/cm^2. Catalysts having a high surface pH have lower average CO_2 concentrations, corresponding to high current densities, and vice versa. Catalysts lying on the right side of the curve experience CO_2 depletion (EOD Cu 300s, OD NWs 600s and OD Cu) and have low C_{2+} selectivities. For example, OD Cu, which has the highest RF of 103 is completely depleted of CO_2 at -1.0 V vs RHE, which explains why it has the highest hydrogen selectivity of 74.6% as well as the lowest C_{2+} selectivity of 22.6%. Similarly, EOD Cu 300s and OD NWs 600s have low C_{2+} selectivities (48.7% and 40.8%, respectively) and high hydrogen selectivities (47.0% and 55.8%, respectively). The catalysts with highest C_{2+} selectivity (EC Cu and EOD Cu 100s) appear in the middle of this curve, and are characterized by similar average pH (~10.6), average CO_2 concentration (~4.09 mM), and C_{2+} selectivity (~69%). These catalysts have an optimum RF for their morphology, leading to a higher pH and thus more C-C coupling relative to the formation of CH_4, but not so high as to result in a significant depletion of CO_2 near the cathode. The left side of the curve represents catalysts which have lower RF values, resulting in a lower pH rise and therefore lower selectivity towards C_{2+} products.

A similar set of results are shown in Fig. 4.6b for an applied voltage of -0.7 V vs RHE. Notice that in this case, the variations in the pH and CO_2 concentration near the catalyst surface differ less significantly from those in the bulk electrolyte (pH = 6.8 and CO_2 concentration = 33 mM) due to the lower current densities observed at this applied potential. Furthermore, none of the catalysts appear to experience CO_2 depletion conditions and differences in pH between all the catalysts are less drastic, as are also the current densities. This would explain why the C_{2+} selectivity for all catalysts converges to a very similar value of ~30%. Only Cu foil is an outlier, exhibiting the lowest C_{2+} selectivity and this is likely due to a lower concentration of grain boundaries (active sites for C-C coupling) relative to what occurs for the OD Cu catalysts.[32,79,80]

In summary, we find that at lower applied overpotentials (viz., -0.7 V vs RHE), where the effects of CO_2 mass transfer to the cathode are minimal, there is relatively little effect of pH and local CO_2 concentration on the selectivity to C_{2+} products. At higher applied overpotentials (viz., -1.0 V vs RHE), where the extent of mass transfer limitation becomes significant, we observe that there is an optimal range of pH and CO_2 concentration for achieving a high C_{2+} selectivity. In this range the pH is elevated relative to that in the bulk electrolyte but the rates of CO_2 conversion to HCO_3^-

and CO_3^{2-} anions are not sufficiently high to draw down the CO_2 concentration to a point where it negatively affects the C_{2+} product selectivity. In this regime, the C_{2+} product selectivity may also be enhanced by the suppression of the kinetics to C_1 products at high pH.

4.4 Conclusions

The catalytic activity of four different variants of oxide-derived copper for electrochemical CO_2 reduction at -0.7 V to -1.0 V vs RHE for two different cations in the electrolyte (Cs^+ and K^+) were compared. We find that use of the larger cation increases selectivity towards C_2 and C_3 (C_{2+}) products at all potentials for all catalysts including the Cu foil control. On the best performing oxide-derived catalyst, up to ~70% selectivity towards C_{2+} products was observed with only ~3% selectivity towards C_1 products at -1.0 V vs RHE. To our knowledge, this is the highest C_{2+} selectivity reported for CO_2 electroreduction in water under ambient conditions of 1 atm and room temperature. For the same conditions in K^+ electrolyte, the selectivity towards C_{2+} products was only 56%, which demonstrates the merits of combining a Cs^+ electrolyte with an oxide-derived catalyst. We also found that there is an optimum roughness factor for the oxide-derived layer to balance the benefits of having a high local pH but still maintaining high concentration of the reactant species (dissolved CO_2). Finally, electrochemical transport modeling illustrates the relationship between catalyst roughness and CO_2 depletion and its effects on C_{2+} product selectivity. The present study shows that high C_{2+} product selectivity can be achieved by using a $CsHCO_3$ as the electrolyte together with oxide-derived Cu catalysts with a modest roughness factor.

Chapter 5: Stability of residual oxides in oxide-derived Cu catalysts for electrochemical CO_2 reduction investigated with ^{18}O labeling

5.1 Introduction

Electrochemical reduction of CO_2 (CO_2R) into chemical fuels and feedstock, powered by renewable electrical energy has been proposed as a strategy to mitigate rising greenhouse gas emissions. [4,28,56] Two main challenges in this area of research are improving the product selectivity and reducing the overpotentials required to drive CO_2R.[2,4,6] "Oxide-derived" Cu catalysts have attracted much attention because they exhibit higher selectivity towards potentially valuable multi-carbon products (e.g. ethanol and ethylene) with lower overpotential requirements.[31,61–63,87–90]

"Oxide-derived" Cu catalysts are formed by oxidizing Cu and subsequently reducing it. Recently, it has been proposed that residual oxides are responsible for their remarkable catalytic properties.[88,89,91] Using *ex-situ* energy dispersive X-ray spectroscopy (EDS), Cuenya and co-workers reported that a large fraction of the initial oxide can be resistant to reduction even under strongly reducing potentials typically used for CO_2R.[88,89] They proposed that the presence of Cu^+ on the surface was important for the formation of C_2/C_3 products.[89] Nilsson and co-workers studied an "Oxide-derived" Cu catalyst with ambient pressure X-ray photoelectron spectroscopy (XPS) and electron energy loss spectroscopy (EELS) and they found a small amount of oxygen residing in the subsurface, possibly modifying the electronic structure of the catalyst and creating active sites with higher CO binding energy.[92]

First principles calculations performed by Goddard and co-workers found that the presence of oxygen in the subsurface would generate a mix of Cu^+ and Cu^0 on the surface. These could then work with adsorbed H_2O and aid in CO_2 activation by forming chemisorbed CO_2, which is the first step of CO_2R.[93] In a separate report, they investigated a partially reduced copper oxide matrix consisting of a mix of Cu^0 and Cu^+ regions.[94] They showed that Cu^+ and Cu^0 regions could act synergistically to promote CO dimerization and suppress C_1 pathways, thereby boosting catalyst selectivity.

However, a few aspects of this emerging picture of the role of residual oxides in controlling the activity of "Oxide-derived" Cu are puzzling. (1) Cu nanomaterials have been shown to readily oxidize, which could create difficulties in performing accurate *ex-situ* quantification of the oxygen content.[95,96] (2) Moisture and oxygen are known to cause corrosion (oxidation) of Cu and exposure to both is difficult to avoid. Corrosion might also be exacerbated in a porous, high surface area material such as "Oxide-derived" Cu. (3) "Oxide-derived" Cu possesses a high density of grain boundaries, which are known to accelerate the oxidation process by serving as nucleation sites and as pathways where diffusion can occur at a faster rate.[97–101] It is therefore possible that upon removal of a reducing potential, Cu rapidly reoxidizes and as a result, the O content characterized *ex-situ* would not be representative of the actual case during CO_2R.

To address these concerns, we employed ^{18}O isotope labeling in order to confirm the presence/absence of residual oxides in "Oxide-derived" Cu during CO_2R. ^{18}O enriched "Oxide-derived" Cu catalysts were synthesized by oxidation/reduction cycling in $H_2{}^{18}O$ following the procedure of Nilsson and co-workers (see experimental section for full details).[37] These "Oxide-derived" Cu catalysts (EC18 Cu) were then tested for CO_2R for various times and the residual ^{18}O

content was analyzed *ex-situ* using secondary ion-mass spectrometry (SIMS). This *ex-situ* method allows us to determine what the "*in-situ"* oxygen content of the catalyst is during operation as any subsequent reoxidation of the catalyst would not result in ^{18}O enrichment above the natural isotopic abundance of 0.2 atomic %.

5.2 Experimental

Materials

Potassium carbonate (99.995% metals basis), potassium chloride (≥99.99% trace metals basis), $H_2{}^{18}O$ (97 atom % ^{18}O) and nitric acid (70%) were purchased from Sigma-Aldrich. Copper slugs (99.9999% metals basis) for e-beam evaporation were purchased from Alfa Aesar. Titanium pellets (99.999%) for e-beam evaporation were purchased from Kurt J. Lesker Company. Silicon wafers were purchased from Silicon Valley Microelectronics, Inc. Selemion AMV anionic exchange membranes were purchased from Asahi Glass Co., Ltd. All chemicals were used without further purification. Carbon dioxide (99.995%), nitrogen (99.999%), argon (99.999%) and hydrogen (99.999%) were purchased from Praxair. Hydrogen, argon, nitrogen and carbon dioxide gas purifiers purchased from Valco Instruments Co. Inc were used on the gas feeds to the electrochemical cell and gas chromatograph. 18.2 MΩ deionized (DI) water was produced by a Millipore system.

Fabrication of Cu films

Si wafers were used as the substrate onto which Cu films were deposited using e-beam evaporation (Angstrom NEXDEP 006). Firstly, a 10 nm Ti adhesion layer was deposited, followed by a 1 μm thick Cu layer. The wafer was then cut into 2cm by 2cm pieces for use as electrodes for CO_2R. Samples were kept in a N_2 glove box when not in use.

Synthesis of electrochemically cycled (EC Cu) catalysts

Here, we synthesize "Oxide-derived" Cu catalysts through the electrochemical cycling method with a halide anion according to the procedure described by Nilsson and co-workers with some modifications.[37] Similar to the previous chapter we shall term this variant of "Oxide-derived" Cu as EC Cu. In this procedure, electrochemical oxidation and reduction are used to create the catalyst. The electrolyte used was 0.1 M $KHCO_3$ and 32 mM KCl in $H_2{}^{18}O/H_2{}^{16}O$ (where appropriate). The potential was swept from open circuit potential to 0.2 V vs Ag/AgCl at 20 mV s^{-1} to electrochemically oxidize, thereby generating Cu_2O from Cu^0. The potential is then swept from 0.2 V to -1.2 V vs Ag/AgCl at the same sweep rate, reducing Cu_2O to Cu^0. The oxidation and reduction cycle was only carried out once in this work, and the 1 μm thick Cu film fabricated via e-beam evaporation was used as the working electrode. See Figure 5.1 for a CV scan recorded during the electrochemical oxidation and reduction process. Samples were kept in a N_2 glove box when not in use. In addition samples prepared with $H_2{}^{18}O$ are termed as EC18 Cu and samples prepared with $H_2{}^{16}O$ are termed as EC16 Cu.

Preparation of electrolyte, electrochemical measurements and product analysis

Preparation of electrolytes, electrochemical measurements and product analysis was performed according to similar procedures as reported previously.[102] Faradaic efficiency and current density data for Cu foil as reported in Figure 5.1 were taken from data reported previously.[102]

Secondary ion mass spectrometry (SIMS)

SIMS measurements were carried out by Evans Analytical Group (EAG) Laboratories. All samples were washed copiously with DI water to remove any residual electrolyte and then dried with a N_2 stream. Samples were then transferred as soon as possible into a N_2 glove box so as to minimize exposure to air. Each sample was then sealed in a N_2 filled container (performed in a glove box) and subsequently packed and sent to EAG Laboratories for SIMS measurements. The SIMS analytical instrument used was a PHI ADEPT 1010 Quadrapole utilizing Cs^+ bombardment. Ion implanted metallic Cu standards were used for quantification. Error in concentration may be up to 3x in composition varying from standard. The steepness of the profile tails may be compromised by the roughness/morphology of the catalyst.

Materials characterization

Scanning electron microscopy images were taken on a FEI Quanta 200 FEG scanning electron microscope using an accelerating voltage of 15 kV. X-ray diffraction patterns were obtained using a Rigaku Smartlab x-ray diffractometer. X-ray photoelectron spectroscopy (XPS) was performed using a Kratos Axis Ultra DLD system using a monochromatized Al Kα source (hν = 1486.6 eV). A takeoff angle of 0º relative to the surface normal was used to sample the maximum surface depth. XPS analysis was performed with CasaXPS software. Energy calibration was referenced to the C1s peak at 284.8 eV.

5.3 Results and discussion

Figure 5.1 shows the electrochemical oxidation and reduction process used to generate EC18 Cu by sweeping to an anodic potential and then to a cathodic potential in an electrolyte consisting of 0.1 M $KHCO_3$ and 32 mM of KCl in $H_2{}^{18}O$. Working electrodes were 1 µm thick Cu films deposited on Si, and oxidation results in formation of $Cu_2{}^{18}O$ nanocubes on the surface (Figure 5.2). Reduction results in loss of the cubical morphology and formation of a porous oxide-derived layer (roughness factor ~22) (Figure 5.2), which is approximately 100 nm thick.

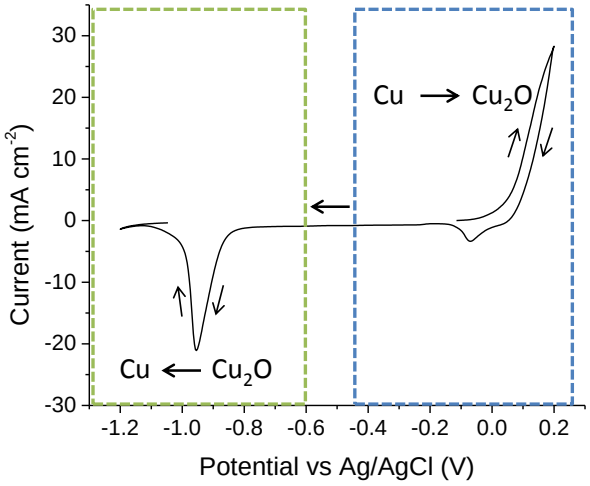

Figure 5.1. Electrochemical oxidation and reduction procedure for generating OD18 Cu. The blue box highlights the oxidation stage and the green box highlights the reduction stage.

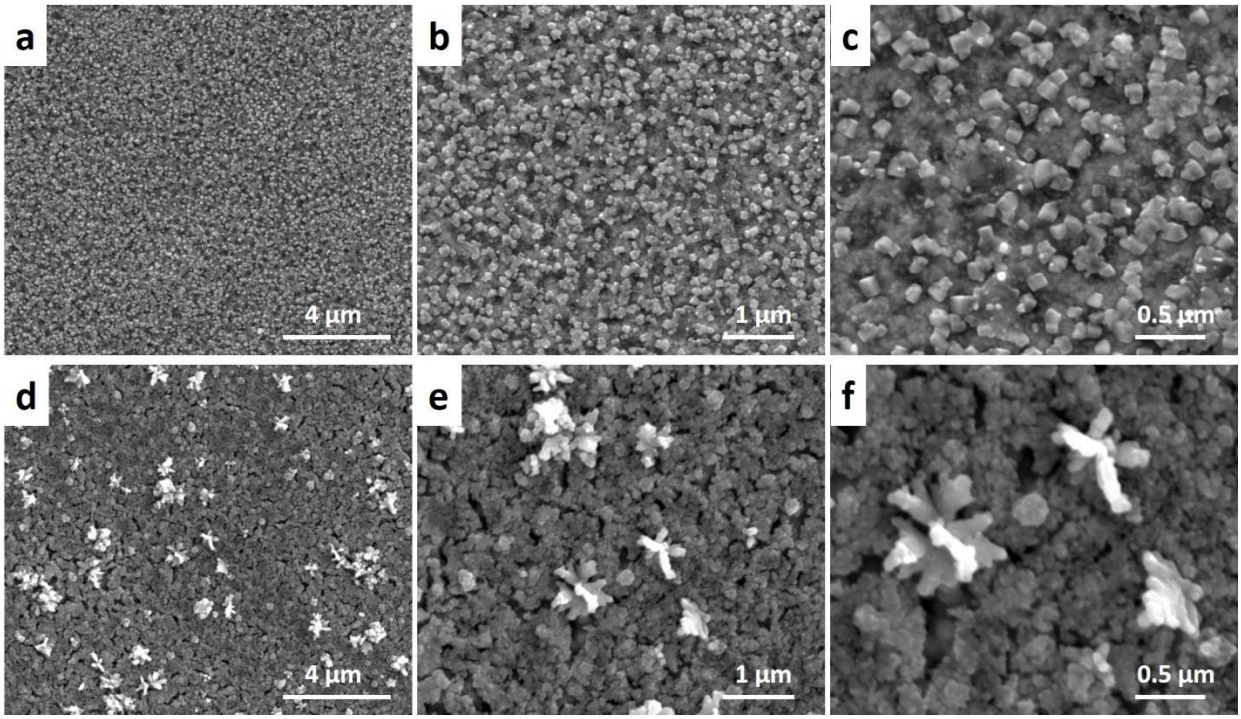

Figure 5.2 (a), (b) and (c) are SEM images of Cu_2O with different degrees of magnification. These are prepared by electrochemical oxidation of Cu by sweeping the potential to 0.2 V vs Ag/AgCl at 20 mV s^{-1}. This results in formation of a cubical morphology on the surface. (d), (e) and (f) are SEM images of the OD Cu catalyst with different degrees of magnification. These are formed by electrochemical reduction of Cu_2O to Cu^0 at -1.2 V vs Ag/AgCl. The cubical morphology appears to be lost upon reduction and a highly porous surface is generated.

The product distributions obtained by operating EC18 Cu catalysts at -1.0 V vs RHE with CO_2 saturated 0.1 M $KHCO_3$ in $H_2{}^{16}O$ electrolyte for 70 mins are shown in Figure 5.3a along with results from the unmodified Cu film and a Cu foil. As expected, EC18 Cu has a higher selectivity towards C_2/C_3 products (60.1%) and lower selectivity towards C_1 products (6.5%) relative to planar Cu controls. During long-term testing (5 h) the gas product distribution was relatively stable, with an ethylene selectivity of ~34% throughout (Figure 5.3b).

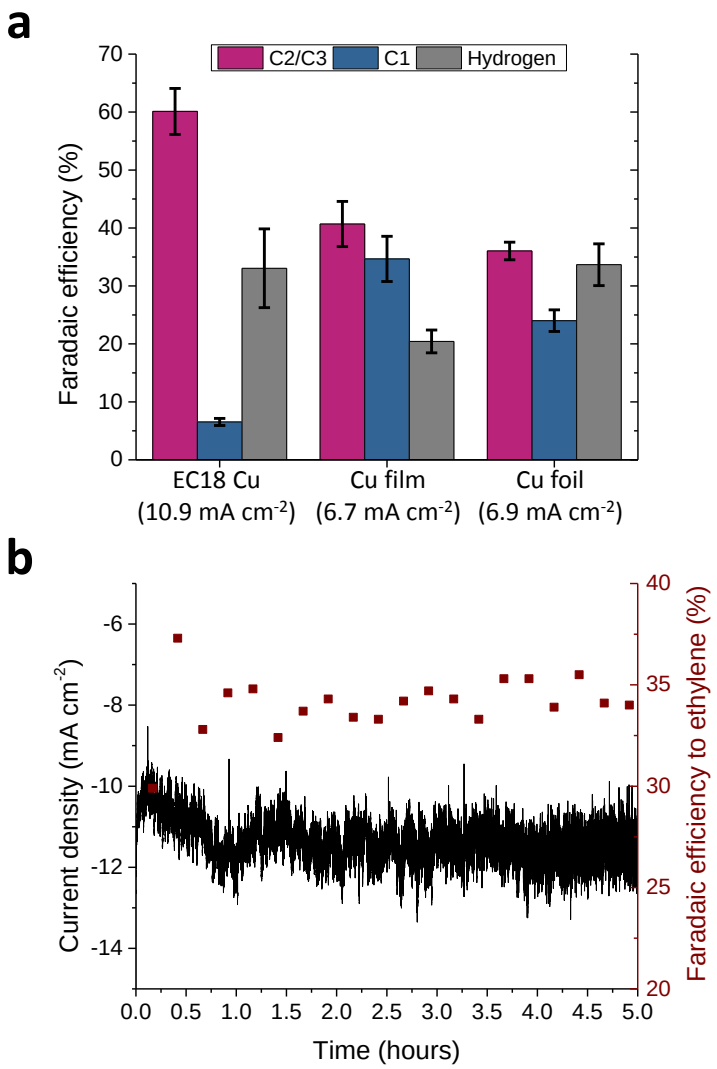

Figure 5.3 (a) Faradaic efficiency to C_2/C_3, C_1 and hydrogen for EC18 Cu, Cu film and Cu foil (70 min tests). Average current densities are given in parenthesis. (b) 5 h long CO_2R with EC18 Cu. Graph shows current density (black line) and faradaic efficiency to ethylene (red squares) vs time. Error bars are standard deviations from 3 repeat experiments.

Next, CO_2R was performed under identical conditions for 10 mins, 30 mins, 1 hr and 5 hrs with fresh samples of EC18 Cu. After CO_2R, the samples were rinsed with copious amounts of DI water, dried and then quickly stored in a N_2 glove box. The residual ^{18}O and ^{16}O contents of these samples, as well as a freshly prepared sample (0 mins) were determined *ex-situ* using SIMS (Figure 5.4). Also, a control sample was prepared by oxidation and reduction in $H_2{}^{16}O$ electrolyte and tested for CO_2R for 1 hr (EC16 Cu 1 hr).

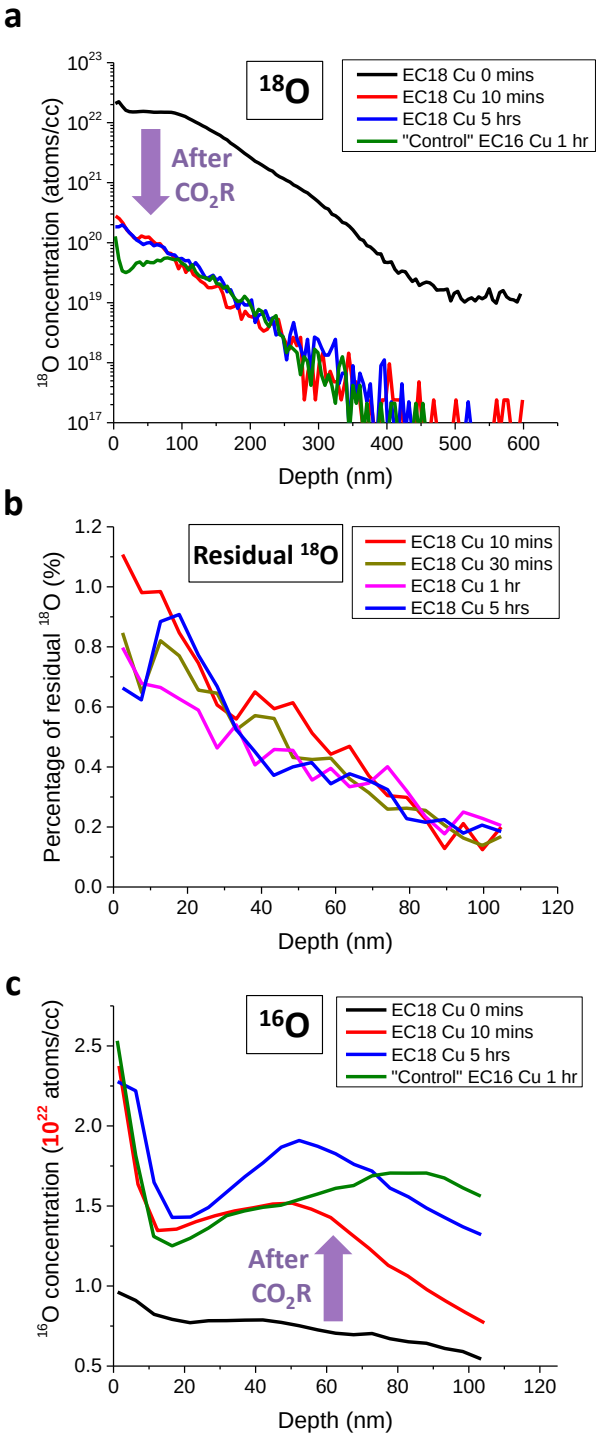

Figure 5.4. (a) ^{18}O and (c) ^{16}O content of EC18 catalysts with different CO_2R durations measured by SIMS. Note the different scales in (a) and (c). For ease of viewing, the results for 30 mins and 1 hour are omitted. (b) shows the percentage of ^{18}O that remains in EC18 Cu after CO_2R.

As seen from Figure 5.4a, the EC18 Cu 0 mins has ^{18}O content on the order of 10^{22} atoms/cc, which is on the same order of magnitude as the atomic density of Cu, showing successful incorporation of ^{18}O into the catalyst structure. However, after CO_2R has been carried out, the ^{18}O content drops drastically. Figure 5.4b shows the percentage of the initial ^{18}O that remains after CO_2R in the top ~100 nm layer (estimated thickness of the oxide-derived layer). Surprisingly, only <1% of the original ^{18}O remains after CO_2R and, in fact, the ^{18}O content drops to the same order of magnitude as the control sample, EC16 Cu 1 hr, which was not enriched with ^{18}O. (We note that the ^{18}O in the control sample is due to its natural abundance of 0.2 atomic %.) This means that the oxide layer is completely reduced, as would be expected since the applied potential typical of CO_2R is >1 V negative of the standard reduction potential of Cu_2O. There therefore cannot be a large concentration of oxygen remaining in the catalyst under CO_2R conditions.

Intriguingly even after CO_2R, the ^{16}O content in EC18 Cu does not change and actually increases (Figure 5.4c). In fact, ^{16}O contents after CO_2R are on the order of 10^{22} atoms/cc, suggesting that samples have been heavily oxidized. However, in our experimental process, care was taken to ensure that exposure to ambient air was as minimal as possible. We therefore considered the possibility that reoxidation of EC Cu occurs rapidly, as soon as the reducing potential is turned off. *In-situ* Raman spectroscopy measurements by Yeo and co-workers on Cu_2O films revealed that application of a potential of -0.99 V vs RHE resulted in loss of the characteristic Cu_2O Raman peaks, and they concluded that complete reduction to metallic Cu^0 had taken place.[62] Surprisingly, once the potential was removed, Cu_2O peaks began to appear again after 60 s and by 120 s had become very distinct; meaning that rapid reoxidation of Cu had taken place.

To further emphasize the rapid oxidation of EC Cu, a freshly prepared EC16 Cu sample was soaked in $H_2{}^{18}O$ (with 0.1 M $KHCO_3$) for 3 mins and then rinsed immediately with DI water. SIMS measurements revealed that the ^{18}O content in this sample (Figure 5.3, blue trace) indeed rises by an order of magnitude. To further investigate the reoxidation process, CO_2R was carried out on an OD16 Cu sample in $H_2{}^{18}O$ electrolyte (0.1 M $KHCO_3$) at -1.0 V vs RHE for 3 mins. This sample was then washed with DI water and the ^{18}O content in this sample was similarly analyzed *ex-situ* using SIMS (Figure 5.3, red trace). Startlingly, this sample showed a very high incorporation of ^{18}O, with concentrations on the order of ~10^{22} atoms/cc, meaning that a large degree of reoxidation had occurred. Taken together, all these results highlight the inaccuracy of *ex-situ* measurements of the oxygen content, since EC Cu can be rapidly reoxidized.

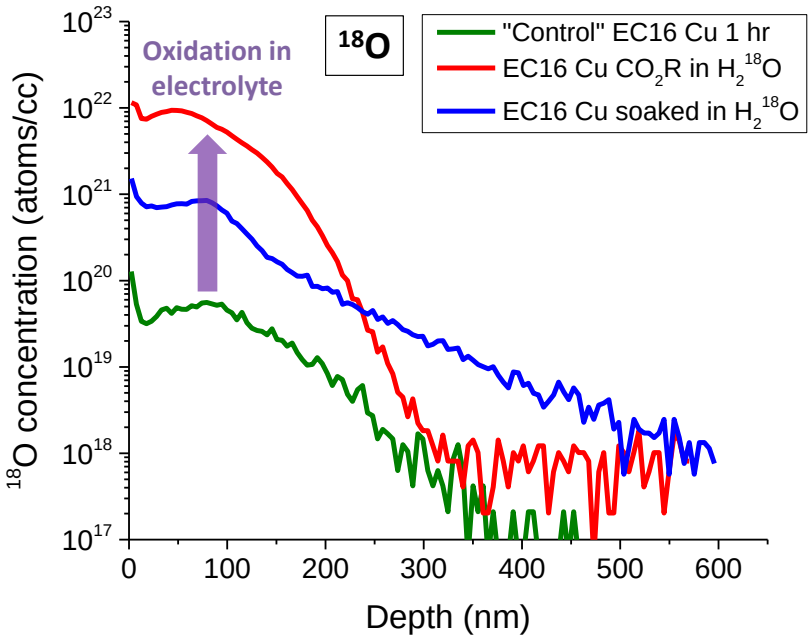

Figure 5.5. ^{18}O content in EC16 Cu 1 hr, EC16 Cu with CO_2R for 3 mins in $H_2{}^{18}O$ electrolyte and EC16 Cu that was soaked in $H_2{}^{18}O$ for 3 mins.

Finally, we consider the reasons for the rapid reoxidation of EC Cu. Firstly, Cu nanomaterials are known to be easily oxidized due to numerous highly reactive undercoordinated atoms on the surface.[96] Secondly, previous studies have shown that grain boundaries can act as nucleation sites for oxide growth as well as provide channels whereby diffusion can take place at a faster rate (compared to diffusion through the bulk lattice).[97–101] EC Cu has a high density of grain boundaries,[31,32,49] which could explain why OD Cu can reoxidize so quickly via exposure to ambient air and moisture (see Figure 5.5).

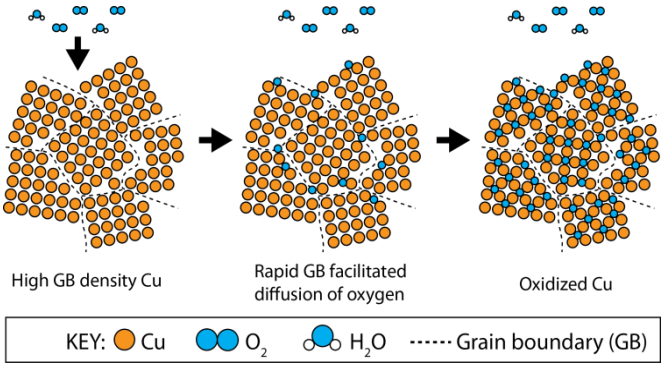

Figure 5.5. Rapid reoxidation of EC Cu occurs because oxygen diffusion and oxide nucleation can be facilitated by grain boundaries.

5.4 Conclusions

In conclusion, the stability of residual oxides was investigated by ^{18}O isotope labeling. ^{18}O enriched oxide-derived Cu catalysts were synthesized and CO_2R was performed with them. The residual ^{18}O content was then analyzed *ex-situ* with SIMS and it was found that only <1% of the original ^{18}O content remained in the samples. We therefore conclude that residual oxides are unstable in our oxide-derived Cu catalysts during CO_2R. We believe that the high C_2/C_3 product selectivity exhibited by these catalysts is more likely due to grain boundaries as previously proposed by Kanan and co-workers[49,79] or by the small amount of oxygen that remains below the surface (a combination of both is likely as well). We also show that these catalysts can rapidly reoxidize due, possibly, to the numerous grain boundaries present in the material. The rapid reoxidation process could compromise the accuracy of *ex-situ* methods for determining the true oxygen content of the catalyst during CO_2R conditions.

Chapter 6: Tunable and bifunctional micropatterned catalysts for control of oxygenate selectivity in electrochemical CO_2 reduction

6.1 Introduction

Electrochemical reduction of CO_2 (CO_2R) to chemical fuels and feedstocks via the use of renewable electrical energy is a potential way to mitigate rising atmospheric CO_2 emissions.[28,103–105] There has therefore been considerable interest in developing efficient and selective electrocatalysts to facilitate this chemical conversion process.[58,106–113] Of the electrocatalysts investigated to date for CO_2R in aqueous solution, Cu remains the only catalyst with significant faradaic yields of C_{2+} hydrocarbons and oxygenates.[4,6,57] However, selectivity towards a specific product such as ethylene or ethanol is not yet high enough to be relevant for practical implementation.[4,28] Therefore, enhancing the selectivity towards products with 2 or more carbons (C_2/C_3), which tend to be more valuable as feedstock and fuels[35] is an attractive technological target.[111,112]

Reduction of CO on Cu produces a similar product distribution as CO_2R[114], albeit with a much lower current density due to the lower solubility of CO in water (~1 mM vs. ~33 mM for CO_2 at 1 atm and 25 °C).[21,32,86] A number of first principles calculations, show that all known products of CO_2R on Cu, with the exception of formate, have CO as the primary intermediate.[42,85,115–119] It is thus reasonable to expect that changes in CO activity at the surface of a Cu electrode could affect the product distribution. In fact, very recently it has been predicted that "CO dimerization [could be accelerated]… by increasing the local concentration of CO by conjoining Cu with another element such as Ag or Au that can produce CO from CO_2," although a method for creating this situation was not specified.[119]

Here we posit that a sequential catalysis strategy can be used to tune the C_2 product distribution in aqueous CO_2R. To realize such a strategy in CO_2R, a system consisting of 2 sites can be envisioned whereby one site converts CO_2 to a stable intermediate, which then diffuses to a second site where it is further reduced to the desired product. More specifically, to produce the intermediate, we will use a metal such as Ag or Au, which produces CO with high selectivity. If this metal is placed in close proximity to Cu, the CO can diffuse or "cross-over" where it can react further, along with the CO_2 which is being reduced concurrently.

Sequential or cascade catalysis has shown previously in the CO_2 reduction literature. Sanford and co-workers used 3 homogeneous catalysts to thermally hydrogenate CO_2 selectively to methanol via formic acid and formate ester intermediates.[120] Jiang and co-workers used 3 enzymes co-located in micelles to convert CO_2 to methanol with NADHP as the reductant.[121] Very recently, Yeo and co-workers studied aqueous electrochemical CO_2 reduction on Zn-Cu composite nanoparticles and attributed the increased ethanol selectivity to "spillover" of CO generated from Zn sites onto Cu sites, where it was further reduced.[122]

The requisite length scale required to realize a sequential catalysis merits some discussion. The transport of the intermediate species between the different active sites competes with diffusion away from them. It is exactly this trade-off between inter-site transport and diffusion to the bulk which limits sequential catalysis in enzymatic systems to active site spacings of a few nm.[123] Similarly, although there are some exceptions,[124] the surface transport required for "spill-over" effects in multi-site heterogeneous catalysis also limits length scales to the nm scale.[125,126] While

we are not aware of an experimental measurement of CO surface diffusion under aqueous CO_2 conditions,[127–129] we will assume, based on measurements of surface diffusion rates of other adsorbed species,[130] that this process will also be constrained to the nanoscale.

Instead, we will show, both by simulations and experiment, that sequential catalysis can be affected on the micron scale, with diffusional transport of the intermediate CO in the liquid phase. This is possible due to the far higher density of catalytic sites (and corresponding molar fluxes) on the surface of a metal electrocatalyst, compared to, for example, enzymatic systems. Specifically, for a bifunctional system with a CO-producing metal (Ag or Cu) and Cu, we will show that CO transport and further conversion is possible for spacing up to fractions of the diffusion layer thickness, which is typically on the order of 100's of microns in electrochemical systems.[25] We emphasize that long range transport of active species from one electrode to another is not unprecedented in electrochemistry and is the operating principle of a rotating ring disk electrode.[25,131–133] We also note that interdigitated electrodes relying on diffusion of species from one electrode to another have been successfully employed for electroanalysis purposes.[134,135] However, in these cases, a one electrode is used to reduce a species and the second is used to oxidize the intermediate.

The sequential catalysis concept is realized in two micropatterned systems. The first consists interdigitated lines of Au and Cu on an insulating SiO_2 substrate. The Au lines are electronically isolated from the Cu lines, which allows for the independent actuation of just one set of lines or both at the same time. The Au lines generate CO for crossover, while the Cu lines reduce the CO and also the externally supplied CO_2 to further reduced products. The ratio of Au and Cu can be adjusted by varying the width of the Au lines, while keeping the width of Cu lines constant, allowing for a systematic study. Having a larger ratio of Au to Cu should result in higher CO availability for crossover per active Cu site present. Our approach, in which both sets of lines are used synergistically in two successive reduction steps is a new concept, which to the best of our knowledge does not have a precedent in the electrocatalysis literature.

In the second system, Cu consisting of 2 different shapes and sizes are patterned onto a Ag substrate; the exposed Ag generates CO for crossover. We will show that these bimetallic microfabricated catalysts allow for the tuning of the CO_2R product distribution. Lower areal coverages of Cu favor C_2/C_3 oxygenates, whereas higher areal coverages favor ethylene, allowing for tuning of the oxygenates to ethylene ratio from 0.59 to 2.39 (while maintaining C_2/C_3 product selectivity at >60% faradaic efficiency). Additionally, typically minor oxygenate products such as acetaldehyde and acetate produced on Cu are greatly enhanced on these systems as a result.

In these systems, we will show that majority of the CO generated from Au/Ag is able to diffuse towards Cu where it is further reduced as evidenced by significantly low CO partial current densities, even at large Au/Ag coverages. Finally, we will also demonstrate that generating the CO locally in close proximity to the Cu effects a catalytic outcome that is different from simply using a gas feed mixture of CO_2/CO at ambient pressure. This is because a non-equilibrium state is established on the surface, whereby a high local concentration of CO can exist without reducing the bulk CO_2 concentration.

6.2 Experimental

Materials. Cesium carbonate (99.995% metals basis), potassium phosphate monobasic (99.99% metals basis), potassium phosphate dibasic (99.95% metals basis), nitric acid (70%), sulfuric acid

(99.999% metals basis), glyoxal solution (40 wt.% in water) and glycolaldehyde dimer were purchased from Sigma-Aldrich. Copper foil (0.1 mm thick 99.9999% metals basis), silver foil (0.1 mm thick 99.99% metals basis) and copper (II) sulfate hydrate (99.999% metals basis) were purchased from Alfa Aesar. Phosphoric acid (85.0-87.0% assay) was purchased from J.T. Baker. Copper sputtering target (99.999%), silver sputtering target (99.99%), carbon sputtering target (99.999%), gold pellets (99.99%) and titanium pellets (99.999%) were purchased from Kurt J. Lesker Company. Silicon wafers were purchased from University Wafer, Inc. Silicon wafers with 1 μm thick thermal oxide layer (SiO_2) were purchased from Silicon Valley Microelectronics, Inc. Selemion AMV anionic exchange membranes were purchased from Asahi Glass Co., Ltd. Acetone and isopropanol were purchased from BDH. Photolithography was carried out using positive photoresist (Shipley Microposit S1818) and development of the photoresist was performed using MF-26A developer. All chemicals were used without further purification. Photolithography masks (chrome/quartz) were purchased from Photo Sciences, Inc. Conductive copper tape was purchased from 3M. Carbon dioxide (99.995%), nitrogen (99.999%), argon (99.999%) and hydrogen (99.999%) were purchased from Praxair. Hydrogen, argon, nitrogen and carbon dioxide gas purifiers purchased from Valco Instruments Co. Inc were used on the gas feeds to the electrochemical cell and gas chromatograph. 18.2 MΩ deionized (DI) water was produced by a Millipore system.

Fabrication of interdigitated AuCu devices. Silicon wafers with 1 μm thick thermal oxide layer (SiO_2 substrates) were broken into semi-rectangular pieces of at least 2.5 cm by 2.5 cm, with one such piece sufficient to fabricate a single AuCu device. This piece was first spin-coated with S1818 positive photoresist and subsequently soft-baked for 90 seconds on a hot plate heated to a temperature of 100 °C. Patterning was then carried out with a photolithography mask with the appropriate design and an aligner equipped with an UV lamp. The exposed photoresist was then developed in MFA-26A developer for 60 seconds, rinsed copiously with DI water and then dried with a stream of nitrogen. Next, 4 nm of Ti (adhesion layer) followed by 100 nm of Au was deposited using e-beam evaporation (Angstrom NEXDEP 006). Lift-off was then carried out by sonicating in acetone, followed by rinsing in isopropanol. The two sets of lines were ensured to be electronically insulated from each other (non-shorting) by connecting a multimeter to the top and bottom contact and checking the resistance. Devices were only deemed to be successfully fabricated if there was no reading on the multimeter even after contact was made. Separate pieces of copper tape were then pasted onto the top and bottom contact for ease of electrical connection. Cu was then subsequently deposited on only one set of lines by electrodeposition using a custom-made compression type electrochemical cell with an o-ring to limit the electrodeposition area to 1.767 cm^2. The Cu deposition solution used was 500 mM $CuSO_4$ solution adjusted to pH 1 with H_2SO_4. The working electrode lead on the potentiostat was connected to the set of lines where copper deposition is desired and the counter electode lead was connected to the other set of lines. It is important to use the other set of lines as the counter electrode as this significantly decreases any unwanted deposition of copper onto the surface. To fabricate the 55%, 21%, 11% and 3% AuCu device, a constant cathodic current density of 1, 0.82, 0.66 and 0.3 mA cm^{-2} respectively was applied for 8 minutes. After deposition was complete, the device was rinsed and soaked in DI water for 5 minutes and later dried with a stream of nitrogen.

Fabrication of lithographically patterned Cu lines/discs on Au or Ag substrates. 8 nm of Ti (adhesion layer) followed by 200 nm of Au or Ag was deposited onto a Si substrate via reactive sputtering using an AJA International ATC Orion 5 sputtering system. The rest of the fabrication,

which involves photolithography, metal deposition and lift-off is identical to that of the AuCu device. In this case however, 30 nm of Cu was deposited onto the substrate for all samples. Samples with a carbon interlayer in between the Ag substrate and Cu were fabricated similarly, with the exception of the deposition of 30 nm of carbon via sputtering followed by the 30 nm Cu layer.

6.3 Results and discussion

Microfabrication of bimetallic cathodes. Two micropatterned systems were fabricated; the first consists of interdigitated lines of Au and Cu on an insulating SiO_2 substrate. The Au lines are electronically isolated from the Cu lines, which allows for the independent actuation of just one set of lines or both at the same time. The Au lines generate CO for crossover, while the Cu lines reduce the CO and also the externally supplied CO_2 to further reduced products. The ratio of Au and Cu can be adjusted by varying the width of the Au lines, while keeping the width of Cu lines constant, allowing for a systematic study. Having a larger ratio of Au to Cu should result in higher CO availability for crossover per active Cu site present. Importantly in such a system, there are no exposed metal-metal interfaces or alloying between the metals. We note that interdigitated electrodes relying on diffusion of species from one electrode to another have been successfully employed for electroanalysis purposes.[134,135] Our approach, in which both sets of lines are used synergistically in two successive reduction steps is a new concept, which to the best of our knowledge does not have a precedent in the electrocatalysis literature.

In the second system, Cu consisting of 2 different shapes and sizes was patterned onto a Ag substrate; the exposed Ag generates CO for crossover. We will show that these catalysts allow for the tuning of the product distribution of Cu. Lower areal coverages of Cu favor C_2/C_3 oxygenates, whereas higher areal coverages favor ethylene, allowing for tuning of the oxygenates to ethylene ratio from 0.59 to 2.39. Finally, we will also demonstrate that generating the CO locally in close proximity to the Cu effects a catalytic outcome that is different from simply using a gas feed mixture of CO_2/CO at ambient pressure. This is because a non-equilibrium state is established on the surface, whereby a high local concentration of CO can exist without reducing the bulk CO_2 concentration. This is observed to result in a higher selectivity towards oxygenates vs ethylene.

Simulations of intermediate species transport. To develop our design for our interdigitated AuCu device system, we simulated the transport of CO from Au lines to Cu lines as well as to the edge of the diffusion layer. Four different devices were modeled, in which Au and Cu lines have the same spacings apart (26 μm) and same width of Cu lines (4.2 μm), but different widths of the Au lines (3.5, 16.25, 35.0 and 147.5 μm). Such an arrangement yields 4 different Cu compositions (by geometric area), which are 55%, 21%, 11% and 3% respectively. For a X% device, X% refers to the ratio of the geometric area of the Cu lines to the total metal area (total metal area = Cu area + Au area). Thus, the 55% AuCu device has the highest Cu coverage, but the lowest Au coverage. On the other hand, the 3% AuCu device has the lowest Cu coverage, but the highest Au coverage. In each case, a CO molar flux of 1.6×10^{-8} mol cm^{-2} s^{-1} was fixed on the Au. As the CO consumption rate on the Cu is not known *a priori*, a boundary condition of zero CO concentration was set on the surface of Cu (ideal sink). Figures 6.1a and 6.1b show the modeling schematic and CO concentration profile, respectively, for the 55% AuCu device. Figure 6.1c shows the percentage of CO consumed and the CO consumption rate for the 4 different AuCu devices based on the modeling results. From the results, it is clear that a significant fraction of the CO generated on the Au is available for further reduction on the Cu and that the devices will allow for control of the flux.

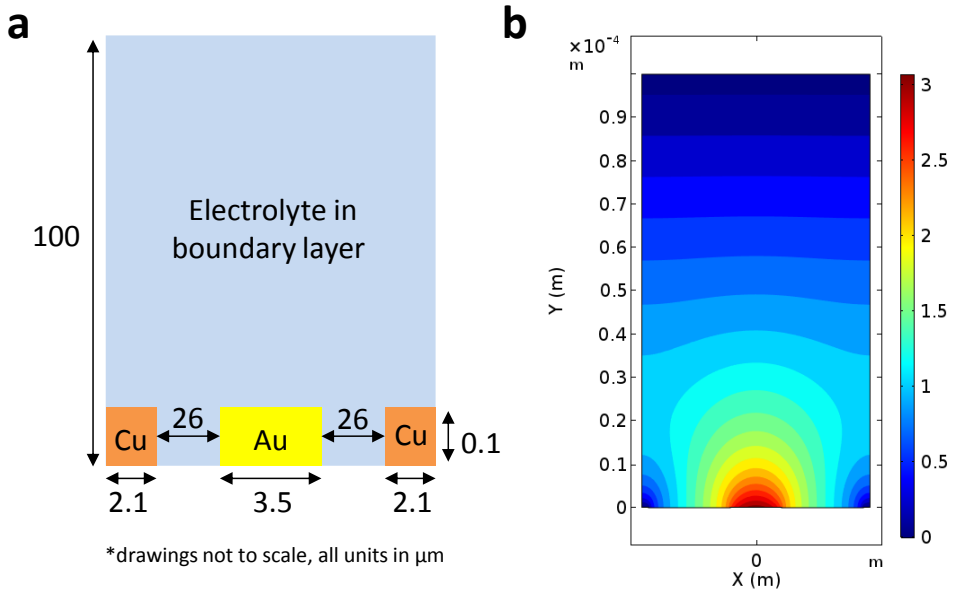

c

AuCu device	Percentage of CO consumed (%)	CO flux to Cu (mol cm^{-2} s^{-1})
55%	62.1	8.28 x 10^{-9}
21%	55.3	3.42 x 10^{-8}
11%	47.2	6.29 x 10^{-8}
3%	22.7	1.28 x 10^{-7}

Figure 6.1. (a) Modeling schematic of CO diffusion transport for the 55% AuCu device. Drawing is not to scale and all units are given in µm. (b) Diffusion profiles of CO from Au lines to Cu lines on the 21% AuCu device. CO concentration values are in mM. (c) Summary of percentage of CO from Au that is consumed on Cu and CO flux to Cu for the 4 different AuCu devices assuming a perfect sink (see text).

The modeling results show that in some cases, the concentration of CO near the surface exceeds the solubility limit of 1 mM (Figure 6.1b). Bubble formation, which could reduce the CO crossover and potentially block surface catalytic would be a potential concern. However, supersaturation of a gas on the surface of an electrode from which it is produced is a well-known effect.[136–140] Notably, smooth electrode surfaces of the type we will employ here have been shown to suppress bubble nucleation, allowing for a high degree of supersaturation.

Microfabricated bifunctional cathode with independent actuation. Four AuCu device systems were fabricated by photolithography with Cu and Au lines on an insulating SiO_2 substrate (see experimental section for fabrication details). Figure 6.2a shows a schematic of the AuCu device, with the design parameters for the 4 different devices in a table. Figures 6.2b and 6.2c show the SEM and EDX images for the 21% AuCu device. As the lines in this device are electronically isolated, either or both can be actuated via an external circuit with on/off switches (Figure 6.2a).

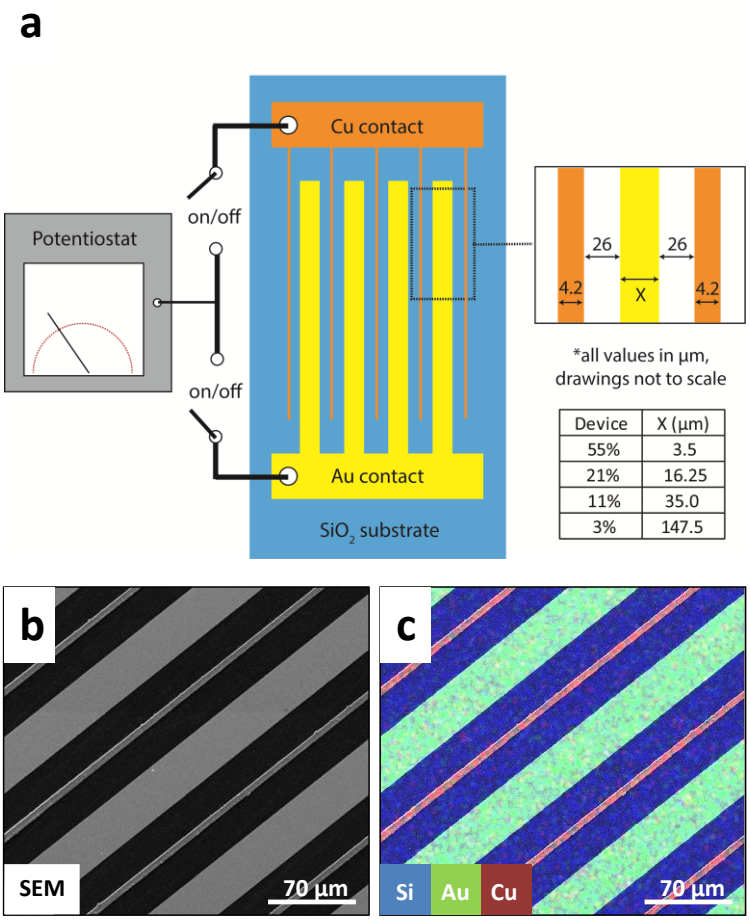

Figure 6.2. (a) Schematic of the interdigitated AuCu device, showing the design parameters for the 4 different devices in a table. Externally connected on/off switches linked to a potentiostat can be turned on and off to actuate both Au and Cu lines, Au only or Cu only. (b) SEM and (c) EDX images of the 11% AuCu device with Si in blue, Au in green and Cu in red. Note: for a X% device, X% refers to the ratio of the geometric area of the Cu lines to the total metal area.

Firstly, we show that the Au and Cu lines can be actuated independently. Unless otherwise stated, electrochemical evaluations were performed at -1.0 V vs RHE in CO_2 saturated 0.1 M $CsHCO_3$ electrolyte. Figure 6.3a shows the product distribution when only the Au lines are actuated. The CO faradaic efficiency was ~53%, with hydrogen making up majority of the rest of the products (~39%). A small amount of hydrocarbons (~2%) was observed in all cases, which is attributed to small amounts of Cu contamination on the Au lines as a result of the deposition process. Figure 6.3b shows that when only the Cu lines are actuated at -1.0 V vs RHE the product distribution is qualitatively similar to that of the Cu foil reference with a faradiac efficiency to oxygenates of about 20%. Note that although formate is an oxygenate, we will not classify it as an oxygenate in our analysis because this product cannot be derived from CO.[7] Thus, for the entirety of the manuscript, we will refer to C_2/C_3 oxygenates solely as "oxygenates" and these include glyoxal, glycolaldehyde, acetate, ethylene glycol, acetaldehyde, ethanol, hydroxyacetone, allyl alcohol, propionaldehyde and propanol.

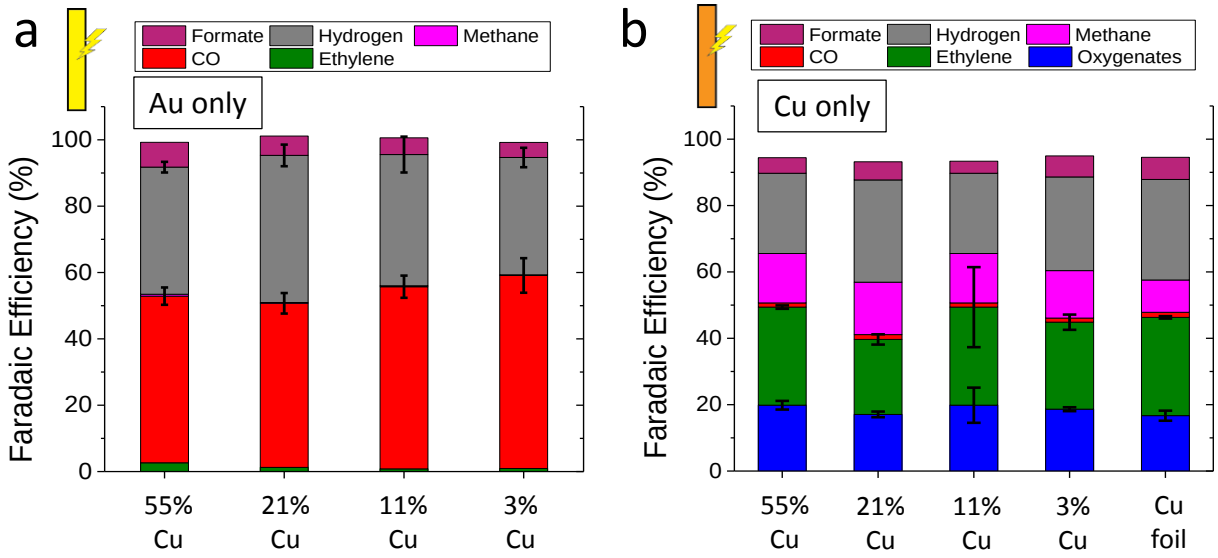

Figure 6.3. Faradaic efficiency plots for the 4 different AuCu devices when: (a) only Au lines are actuated and (b) when only Cu lines are actuated. In (b), Cu foil data is shown as a reference. For a X% device, X% refers to the ratio of the geometric area of the Cu lines to the total metal area. Errors bars are given for CO and H_2 in (a) and ethylene and oxygenates in (b). Error bars are standard deviations for replicate experiments, typically 3.

To study the effect of CO crossover, both the Au and Cu lines were actuated at the same time (Figure 6.4a and 6.4b); there are 2 main effects. Firstly, the partial current density to CO (Figure 6.4c) drops significantly when both Au and Cu are actuated compared to when only Au is actuated, showing that CO is consumed by the Cu lines. Secondly, analysis of the oxygenates to ethylene ratio (in terms of faradaic efficiency) shows a steady increase with decreasing Cu coverage, from a value of 0.67 for the 55% device to 1.18 for the 3% device (Figure 6.4d). Comparatively, when only Cu is actuated, the oxygenates to ethylene ratio for all the devices is a lower value of ~0.71.

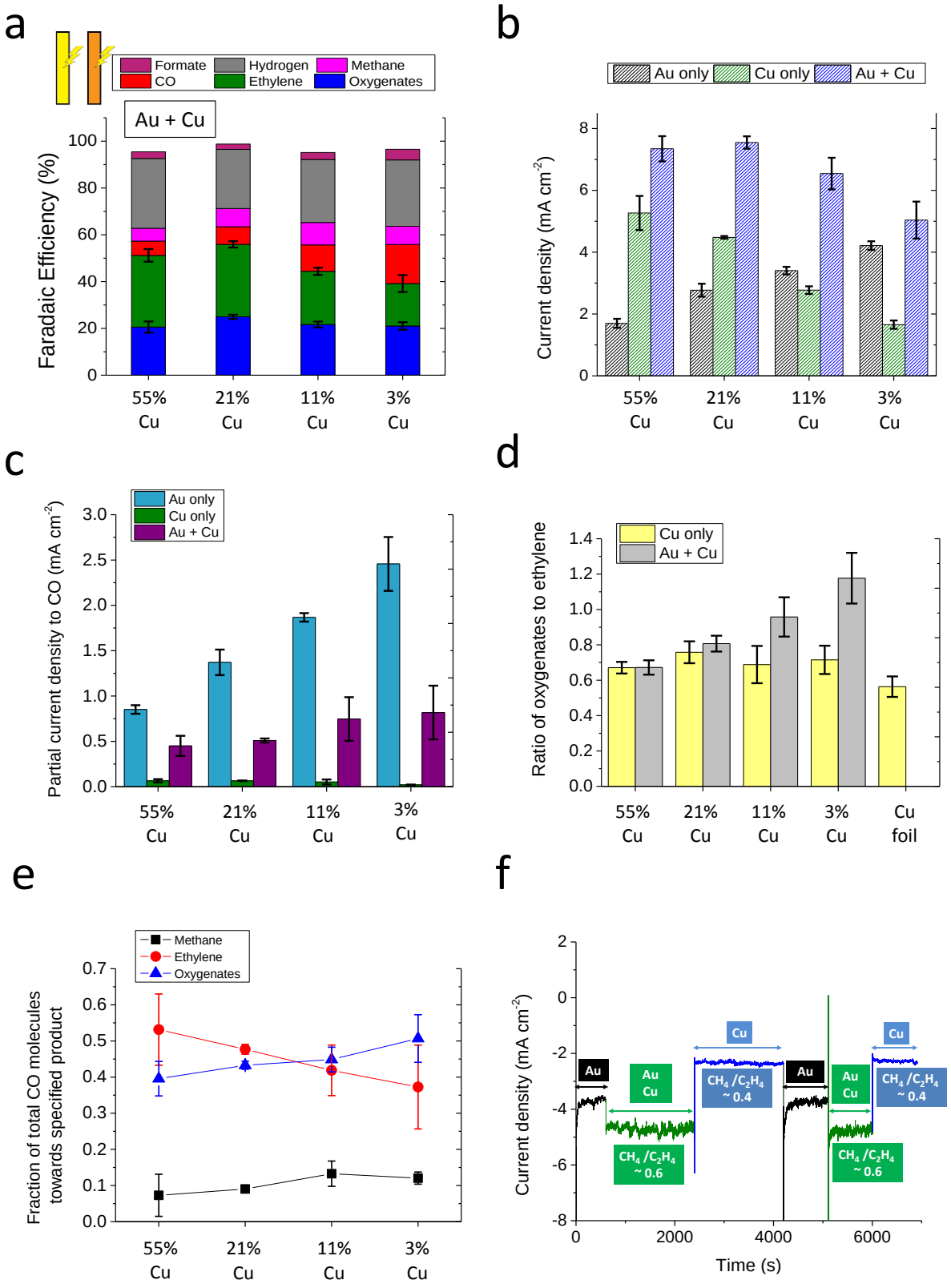

Figure 6.4. (a) Faradaic efficiency plots for the 4 different AuCu devices when both Au+Cu lines are actuated. Error bars are shown for oxygenates and ethylene. (b) Total current densities and (c)

partial current densities to CO for the Au only, Cu only and Au+Cu case. (d) Ratio of oxygenates to ethylene (in terms of faradaic efficiency) for the 4 AuCu devices for both cases when only Cu is actuated and when both Au and Cu are actuated. (e) Fraction of total CO molecules going towards methane, ethylene or oxygenates. (f) Current density profile when different sets of lines are actuated for the 3% AuCu device. Black: Au only, blue: Cu only and green: Au and Cu. When Au lines are actuated, an observable increase in the methane to ethylene ratio is observed, as would be expected from (e). Note: where appropriate, Cu foil data is shown as a reference. Also, for a X% device, X% refers to the ratio of the geometric area of the Cu lines to the total metal area. Error bars are standard deviations for replicate experiments, typically 3.

Microfabricated bifunctional electrode with reduced spacing. We hypothesized that CO crossover could be further enhanced if Cu were patterned directly onto a Ag substrate due to increased proximity between Cu and the CO source. Cu lines of 8.6 μm width of varying spacings were fabricated onto a Ag substrate (Figure 6.5a), which yields catalysts with 18.2, 25.6, 51.8 and 77.2% areal coverage of Cu. A control sample was fabricated as well, in which 100% of the Ag surface was coated with Cu. Figures 6.5b and 6.5c reveal a trend similar to that of the AuCu devices; a lower areal coverage of Cu results in higher oxygenate to ethylene ratios. Going from 77.2% Cu to 18.2% Cu, this ratio increases from 0.72 to 1.15 and the faradaic efficiency to oxygenates can be tuned from 21.3% to 28.8%. For the case where 100% of the Ag substrate is covered by Cu (100% Cu), the oxygenates to ethylene ratio (0.59) is very similar to that of Cu foil reference (0.56), as expected. Also, as the Cu areal coverage decreases, the faradaic efficiency to hydrogen goes down as well, with a value of only 16.0% for 18.2% Cu. Also, the faradaic efficiency to CO is observed to go up with lower Cu coverage, indirectly indicating a larger molar flux of CO available to Cu.

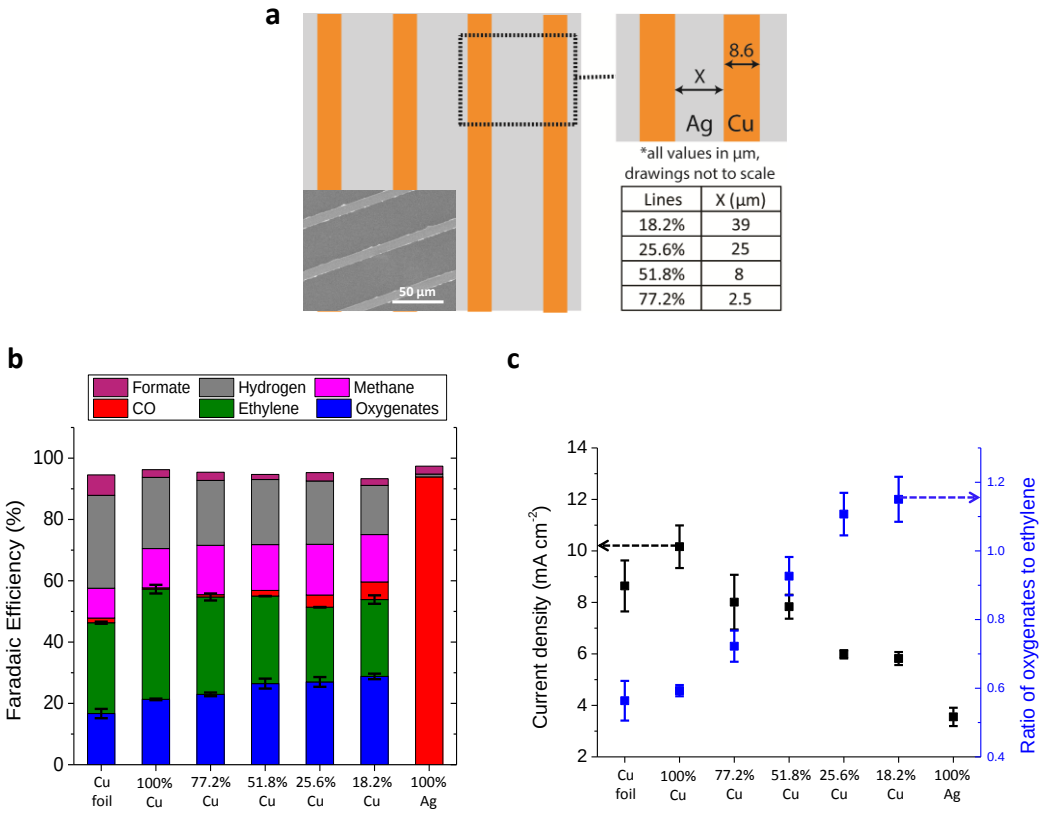

Figure 6.5. (a) Schematic of the Cu lines on Ag substrate system, with design parameters shown in a table. Inset shows a SEM image of 18.2% Cu lines on Ag. (b) Faradaic efficiency for Cu lines on Ag system as a function of Cu areal coverage. 100% Ag refers to the Ag substrate. Error bars for oxygenates and ethylene are given. (c) Current density (black) and ratio of oxygenates to ethylene (blue) as a function of Cu areal coverage. Error bars are standard deviations for replicate experiments, typically 3.

To further increase the oxygenate to ethylene ratio in the Cu on Ag system, we hypothesized that CO crossover could be made more facile by shrinking the dimensions of the Cu. Furthermore, the trends observed in Figures 6.5b and 6.5c suggest that further tunability in the oxygenate to ethylene selectivity could be made by going to even lower areal coverages of Cu. To this end, 1.6 μm Cu dots were fabricated in a hexagonal pattern with 4 different nearest neighbor distances (see Figure 6a/b) to achieve 4 different Cu areal coverages (2.4, 4.3, 7.8 and 18.8%). As expected, even higher oxygenate to ethylene ratios were obtained (Figure 6c and 6d), with samples possessing a lower Cu areal coverage having a higher ratio. With this system, the ratio of oxygenates to ethylene can be tuned from 1.25 with 18.8% Cu all the way to 2.39 with 2.4% Cu and the faradaic efficiency to oxygenates can now be increased all the way to 41.3%. Interestingly for the 2.4% Cu case, the faradaic efficiency for oxygenates (41.3%) is even higher than that for methane and ethylene combined (26.1%). Furthermore, the faradaic efficiency to hydrogen was only 5.14%, although faradaic efficiency to CO was at 22.2%. In general, it is observed that lower Cu coverages result in lower faradaic efficiencies to hydrogen and is likely due to Ag substrate producing minimal amounts of hydrogen at this potential (Figure 6.6c).

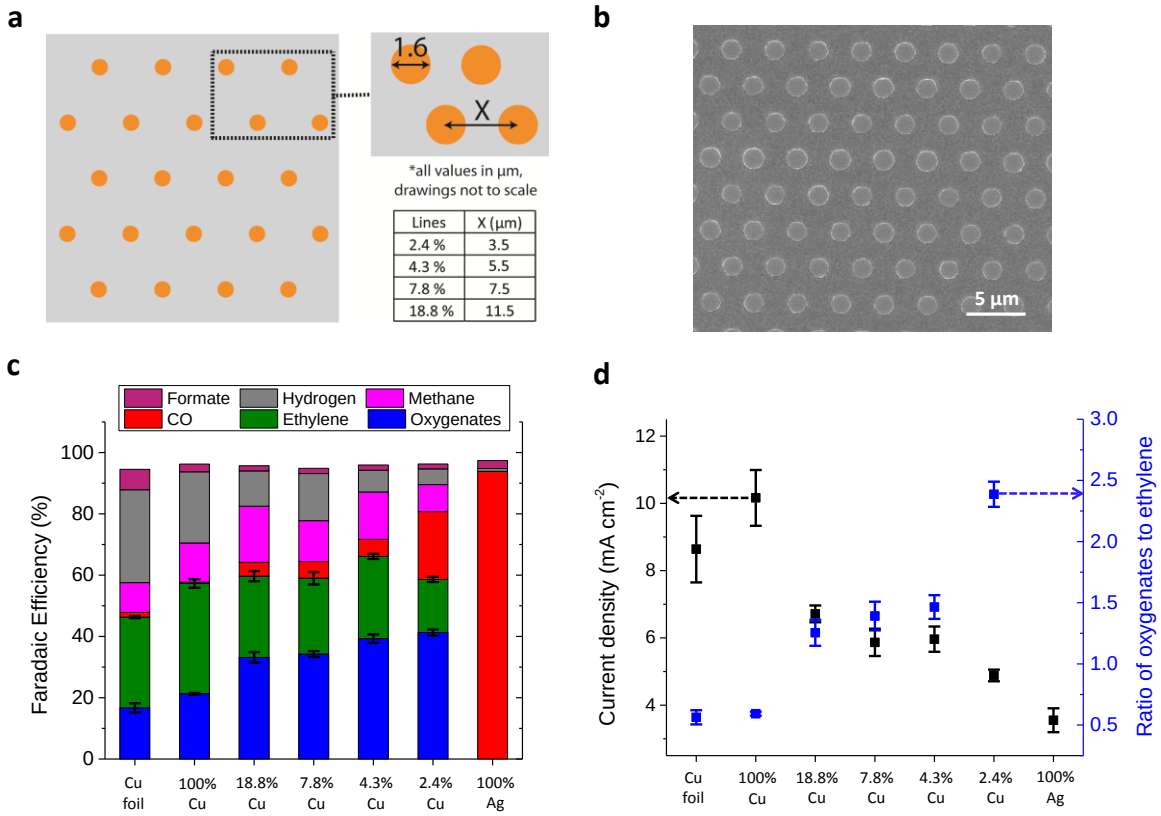

Figure 6.6. (a) Schematic of the Cu dots on Ag substrate system, with design parameters shown in a table. (b) SEM image of 18.8% Cu dots on Ag. Faradaic efficiency towards various products for Cu dots on Ag system as a function of Cu areal coverage. 100% Ag refers to the Ag substrate. Error bars for oxygenates and ethylene are given. (c) Current density (black) and ratio of oxygenates to ethylene (blue) as a function of Cu areal coverage. Error bars are standard deviations for replicate experiments, typically 3.

Figure 6.7a shows the fraction of total CO molecules going to methane, ethylene and oxygenates for the Cu dots/lines system. This figure highlights the considerable tunability of our catalyst system; the fraction of CO molecules going to oxygenates can be varied from 0.33 to 0.67 and the fraction to ethylene from 0.53 to 0.24. The fraction towards methane appears relatively constant, however slight decreases are observed at lower Cu coverages. In Figure 6.7b, the breakdown of the oxygenates into their various components for the Cu dots/lines catalyst systems is plotted. Interestingly, the oxygenates with the largest increases in faradaic efficiency with lower Cu coverage are acetaldehyde and acetate. The 2.4% Cu dots system exhibits a faradaic efficiency of 14.4% to acetaldehyde and 6.8% to acetate. Comparatively, on Cu foil and 100% Cu, these 2 products are only generated in minor amounts (~0.6% for acetaldehyde and ~0.7% for acetate). To the best of our knowledge, acetaldehyde has never been reported at an FE above 0.4%.[6] On the other hand, the faradaic efficiency towards ethanol and propanol remain relatively constant with Cu coverage. Analysis of the molar flux towards acetaldehyde and acetate reveals the large increases in the production rates of these products with lower Cu areal coverages (Figure 6.7c).

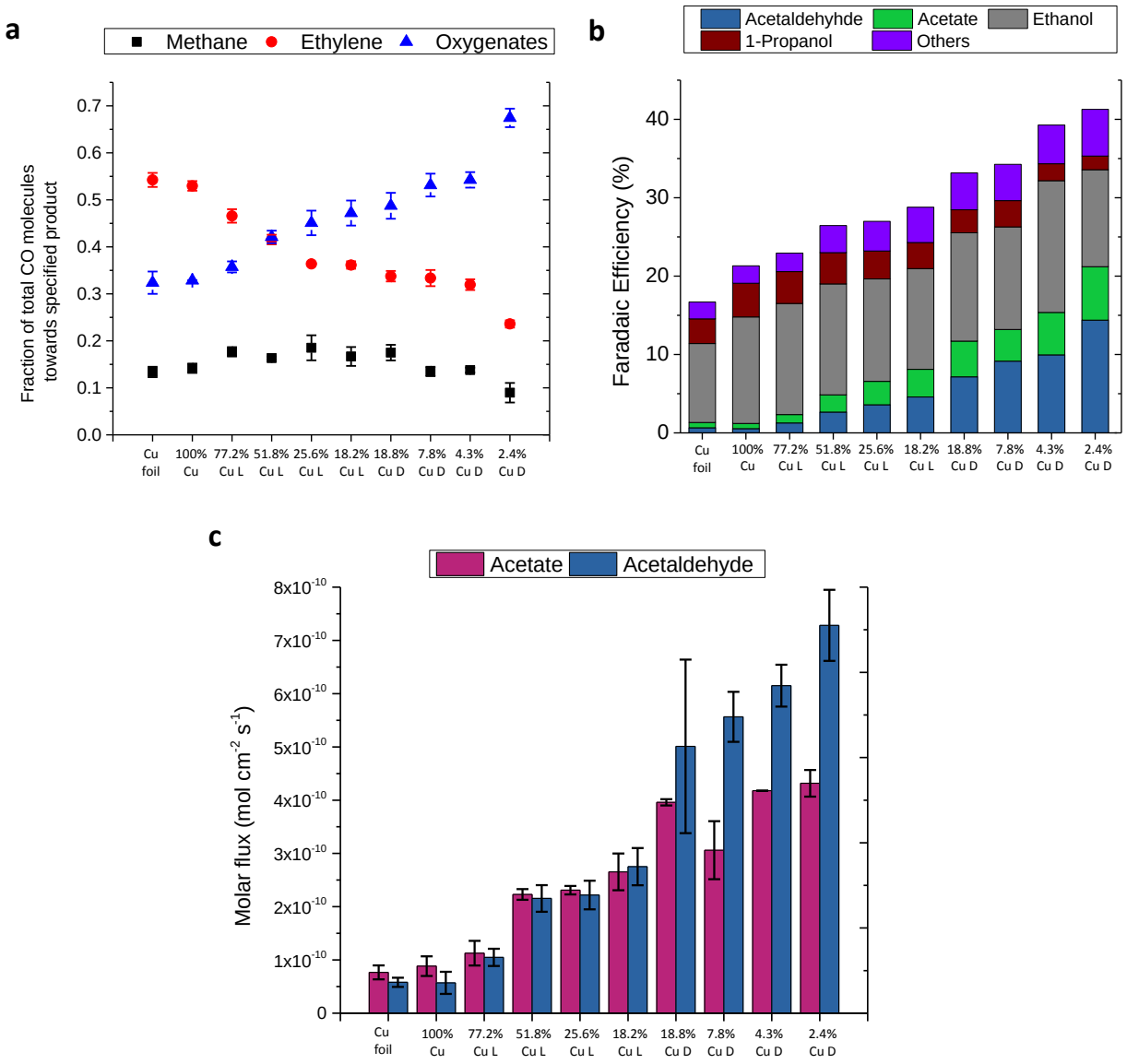

Figure 6.7. (a) Fraction of total CO molecules going towards methane (black), ethylene (red) and oxygenates (blue). (b) Breakdown of the oxygenates into their various components for the Cu dots/lines on Ag substrate. (c) Molar flux towards acetate and acetaldehyde. D refers to dots and L refers to lines.

Mechanism for enhanced oxygenate selectivity. Finally, we consider the mechanism causing increased oxygenate production from CO crossover. One mechanism suggested by Yeo and co-workers for their Cu-Zn system is that CO desorbs from Zn to form nonadsorbed CO, which then diffuses to Cu and inserts itself in between Cu and $*CH_2$ to form $*COCH_2$, which then leads to acetaldehyde and finally to ethanol[122]. This pathway is based on a mechanism previously proposed by Hori and co-workers.[114] However theoretical calculations, for example those by Goddard and co-workers, have shown that $*CH_2$ is an intermediate that leads exclusively to methane.[116,117,119] If $*CH_2$ is involved in the pathway to oxygenates, there should be a reduction of the fraction of methane with increasing CO crossover (decreasing Cu coverage). However, the methane fraction

remains relatively constant with Cu coverage (Figure 6.7a), which means that the $*CH_2$ intermediate cannot be an intermediate for oxygenate formation via CO crossover. Instead, the data suggests that CO crossover to oxygenates and ethylene formation compete with each other.

Contemporary theoretical mechanistic understanding of reaction pathways suggests that formation of C-C coupled products should take place between two *CO or between *CO and *COH/*CHO.[85,116,117,119] For example, based on work by Goddard and co-workers[85], there appear to be 4 different pathways that *CO molecule can take, each leading to different outcomes. The first is the CHO pathway which leads to C_1 products (methane/methanol). A COH pathway is also possible, in which *CO converts into *COH, which can be further reduced into C_1 products. Alternatively, *COH can couple with a *CO and this leads to C_2/C_3 products (CO-COH pathway). Finally, two *CO can form a dimer (CO-CO pathway), which leads exclusively to C_2/C_3 products.

Considering the two possible means of forming C_2/C_3 products, it is not immediately obvious how additional CO from Au or Ag could cause a change in the ethylene to oxygenate ratio. Moreover, in previous work by Hori and co-workers as well as Jaramillo and co-workers on Cu, it appears that oxygenates such as ethanol trend similarly with ethylene, which means that these products should be produced via similar pathways.[4,6] In particular, Koper and co-workers suggest one possible pathway in which ethylene and ethanol start from the same intermediates and only branch out at the final 3 electron transfer steps.[7,42] Therefore, anything that increases the oxygenate selectivity should in principle increase the ethylene selectivity as well.

One possibility to explain the increased oxygenate selectivity due to CO crossover is that this could induce a higher *CO coverage over Cu during CO_2R, due to the presence of a local source of CO in close proximity to the Cu regions. Theoretical calculations have suggested that the main surface species on Cu during CO_2R, surface sites of Cu are *CO and *H, with the coverage of each intermediate depending on the surface facet, strain, applied potential and partial pressure of CO.[118,119,141,142] According to Norskov and co-workers,[142] the *CO and H* coverage determine the CO dimerization rate and surface hydrogenation rate respectively. When a local source of CO is present, the chemical potential of CO on Cu can be raised, leading to a higher *CO coverage and a lower *H coverage.[142] A higher *CO coverage can result in a decrease in *CO binding energy,[142,143] which would shift Cu to the left along the theoretical activity volcano for CO_2R[144] and therefore induce a change in the catalytic properties of Cu. Furthermore, a lower *H coverage might result in a slower surface hydrogenation rate of CO dimers. A high *H coverage could be required to sustain hydrogenation of CO dimers all the way to ethylene, with a low *H coverage possibly favoring the formation of oxygenates instead.

Another possibility which is consistent with our experimental results is that nonadsorbed CO couples directly with adsorbed C_1 intermediates on Cu leading to oxygenates. Recently, calculations by Goddard and co-workers show that nonadsorbed CO can indeed couple directly with *CHO to form *CO-CHO.[119] Direct coupling of *CHO with a nonadsorbed CO species might have a different catalytic outcome versus coupling with an adsorbed CO intermediate (reminiscent of a Langmuir-Hishelwood vs an Eley-Rideal mechanism). In this case, direct coupling of nonadsorbed CO with *CHO might result in an oxygenate selective pathway that is competitive to ethylene formation. Interestingly in the same work, Goddard and co-workers proposed the use of Au or Ag as a local CO source to effect a change in CO dimerization of Cu, although the specific effect on the product distribution was not evaluated.[119]

6.4 Conclusions

In summary, we have shown unambiguously that CO generated by a nearby CO producing catalyst can crossover onto Cu resulting in increased oxygenate production. This is demonstrated with an interdigitated system of alternating Au and Cu lines which can be independently actuated; the oxygenate to ethylene ratio is ~0.71 when only Cu lines are actuated and 1.18 when both sets of lines are actuated. We postulate that this effect could be a result of an increase in *CO coverage on Cu or possibly due to direct coupling occurring between nonadsorbed CO and C_1 intermediates on Cu. These insights are then translated into a second system, in which Cu dots/lines of fixed dimensions are patterned directly onto a Ag substrate, allowing for the proximity between Cu and the CO producing catalyst to be significantly reduced. In such a system, we are able to systematically tune the product distribution of Cu and adjust the ratio of oxygenates to ethylene from 0.59 to 2.39.

Chapter 7: Future outlook

7.1 Improving catalyst selectivity

Despite much progress in the field in these recent years, the issue of selectivity remains an unanswered challenge. A catalyst in the literature exhibiting with >90% faradaic efficiency towards a specific C-C coupled product has yet to be reported. To achieve this, progress must be made to suppress the competing hydrogen evolution reaction. Also, much must be done to streamline the products into a specific product, with targets such as ethanol or propanol. Such products are highly desirable since they are already employed in our existing energy infrastructure. Catalyst selectivity is important because of down-stream product separation issues. Separation of various oxygenates such as ethanol as well as each other can become a time consuming and energy intensive process, which could defeat the entire purpose of developing CO_2 reduction as a viable green technology. For example, possible products such as ethanol and propanol mix very well with each other. If only one oxygenate product is produced, then this issue can be avoided entirely. However, on this note extracting products from the solvent (water) is of extreme importance but has been so far largely overlooked. More research has to be done in order to come up with energy efficient ways to solve this issue. If catalysts that can be engineered to give 2 products, a gaseous hydrocarbon such as ethylene and a liquid oxygenate such as ethanol could be ideal as well as product separation would less of an issue as these products would not mix. In addition, a catalyst, which generates predominantly acetaldehyde, could be good as well not only because it is a valuable commodity chemical, but also because it has a low boiling point, which makes it easy to extract from aqueous solutions.

7.2 Improving catalyst activity

Besides selectivity, improving catalyst activity is important as well. In order to improve the energy efficiency of CO_2 reduction, catalysts should operate with as low overpotential as possible. Thus far, most reports show that an overpotential approximately 1 V is required in order to generate products with an appreciable current density. A viable solution could be to turn to CO reduction instead. It has been shown that CO reduction with oxide-derived Cu catalysts can be performed selectively with very low overpotential.[32] At the same time, CO_2 reduction to generate CO can be done so very selectively (>90%) and at very low overpotential.[5,30,145] A future design of a CO_2 reduction can therefore be envisioned whereby CO_2 is first taken to CO in a first reactor and then further reduced to oxygenates in a second reactor.

7.3 Diffusion limitations

A major issue of CO_2 reduction in aqueous solutions is that the solubility limit of CO_2 in water is only 33mM. As mentioned in chapter 4, this leads to a cap on the maximum CO_2 reduction current that may be drawn, due to diffusion limitations. In the system that we employ, it was found that a maximum current density of 10-15 mA cm^{-2} could be supported, beyond which the hydrogen evolution reaction would be the dominant reaction. In order to alleviate this issue, there has been some research on the use of gas diffusion electrodes, in which current densities on the order of >100 mA cm^{-2} to ethylene have been reported.[146] In such a system, CO_2 is fed in the gas phase

across a catalyst layer made of porous carbon with copper nanoparticle catalysts. This catalyst layer is partially wet with electrolyte, generating numerous 3 phase interfaces in which CO_2 reduction occurs. Such a system has a number of advantages over the traditional system in which we employ. (1) Since CO_2 is in the gas phase, solubility limitations are lifted and the catalyst essentially has an unlimited supply of reactant to work on. (2) The electrolyte used can be made to be alkaline, which can help to suppress hydrogen evolution as well as promote C-C coupling. (3) The ability to use an alkaline electrolyte also means that lower overpotentials are required to drive the CO_2 reduction electrolyzer. Similar to the suggestion in 7.2, a 2-stage reactor system can also be envisioned here. The first reactor can take CO_2 to CO and the second reactor can take CO to reduced oxygenates. Since both systems are gas diffusion based, expected current densities with this integrated system would be very high.

7.4 Understanding mechanisms

Enabling the deterministic design of more selective and efficient catalysts requires understanding of the reaction mechanisms to predict how changes in the catalysts and electrolyte can modify the kinetics and products. Indeed, a number of theoretical papers have been published explaining how the experimentally observed changes in products depend on pH, applied potential, and presence of counter ions.[85,147–149] It is generally accepted that on various Cu surfaces, CO_2 reduces first to CO.[114,150] At low pH, CO can further reduce to *HCO or *OCH and then to *CH_2OH, leading to methane or methanol formation.[85,117] At pH> 7, CO can undergo C-C coupling to generate a *CO-CO dimer[42,84,85,117,119,142], which then forms *OC-COH[151]. Subsequent steps leading to ethylene and ethanol have been further studied in quantum mechanics (QM) based theory papers.[42,115,117–119,152] However, these proposed mechanisms often do not agree entirely, possibly due to differences in the assumptions made as well as differences in how the solvent is modeled (implicit/explicit vs vacuum). This highlights the huge complexity of CO_2 reduction and there remains much to be done, both experimentally and theoretically towards understanding these reaction mechanisms.

Chapter 8: References

(1) Perez, R.; Zweibel, K.; Hoff, T. E. Solar Power Generation in the US: Too Expensive, or a Bargain? *Energy Policy* **2011**, *39*, 7290–7297.

(2) Kuhl, K. P.; Hatsukade, T.; Cave, E. R.; Abram, D. N.; Kibsgaard, J.; Jaramillo, T. F. Electrocatalytic Conversion of Carbon Dioxide to Methane and Methanol on Transition Metal Surfaces. *J. Am. Chem. Soc.* **2014**, *136*, 14107–14113.

(3) Hori, Y.; Murata, A.; Takahashi, R. Formation of Hydrocarbons in the Electrochemical Reduction of Carbon Dioxide at a Copper Electrode in Aqueous Solution. *J. Chem. Soc. Faraday Trans. 1 Phys. Chem. Condens. Phases* **1989**, *85*, 2309.

(4) Hori, Y. Electrochemical CO2 Reduction on Metal Electrodes. In *Modern Aspects of Electrochemistry SE - 3*; Vayenas, C.; White, R.; Gamboa-Aldeco, M., Eds.; Modern Aspects of Electrochemistry; Springer New York: New York, NY, 2008; Vol. 42, pp. 89–189.

(5) Ma, M.; Trześniewski, B. J.; Xie, J.; Smith, W. A. Selective and Efficient Reduction of Carbon Dioxide to Carbon Monoxide on Oxide-Derived Nanostructured Silver Electrocatalysts. *Angew. Chemie Int. Ed.* **2016**, *55*, 9748–9752.

(6) Kuhl, K. P.; Cave, E. R.; Abram, D. N.; Jaramillo, T. F. New Insights into the Electrochemical Reduction of Carbon Dioxide on Metallic Copper Surfaces. *Energy Environ. Sci.* **2012**, *5*, 7050–7059.

(7) Kortlever, R.; Shen, J.; Schouten, K. J. P.; Calle-Vallejo, F.; Koper, M. T. M. Catalysts and Reaction Pathways for the Electrochemical Reduction of Carbon Dioxide. *J. Phys. Chem. Lett.* **2015**, *6*, 4073–4082.

(8) Kumar, B.; Asadi, M.; Pisasale, D.; Sinha-Ray, S.; Rosen, B. A.; Haasch, R.; Abiade, J.; Yarin, A. L.; Salehi-Khojin, A. Renewable and Metal-Free Carbon Nanofibre Catalysts for Carbon Dioxide Reduction. *Nat. Commun.* **2013**, *4*, 2819.

(9) Nakata, K.; Ozaki, T.; Terashima, C.; Fujishima, A.; Einaga, Y. High-Yield Electrochemical Production of Formaldehyde from CO2 and Seawater. *Angew. Chemie* **2014**, *126*, 890–893.

(10) Zhang, S.; Kang, P.; Ubnoske, S.; Brennaman, M. K.; Song, N.; House, R. L.; Glass, J. T.; Meyer, T. J. Polyethylenimine-Enhanced Electrocatalytic Reduction of CO2 to Formate at Nitrogen-Doped Carbon Nanomaterials. *J. Am. Chem. Soc.* **2014**, *136*, 7845–7848.

(11) Wu, J.; Yadav, R. M.; Liu, M.; Sharma, P. P.; Tiwary, C. S.; Ma, L.; Zou, X.; Zhou, X.-D.; Yakobson, B. I.; Lou, J.; *et al.* Achieving Highly Efficient, Selective, and Stable CO2 Reduction on Nitrogen-Doped Carbon Nanotubes. *ACS Nano* **2015**, 5364–5371.

(12) Azuma, M.; Hashimoto, K.; Hiramoto, M.; Watanabe, M.; Sakata, T. Electrochemical Reduction of Carbon Dioxide on Various Metal Electrodes in Low-Temperature Aqueous

KHCO3 Media. *J. Electrochem. Soc.* **1990**, *137*, 1772–1778.

(13) Banks, C. E.; Crossley, A.; Salter, C.; Wilkins, S. J.; Compton, R. G. Carbon Nanotubes Contain Metal Impurities Which Are Responsible for the "Electrocatalysis" Seen at Some Nanotube-Modified Electrodes. *Angew. Chemie Int. Ed.* **2006**, *45*, 2533–2537.

(14) Pumera, M.; Iwai, H. Multicomponent Metallic Impurities and Their Influence upon the Electrochemistry of Carbon Nanotubes. *J. Phys. Chem. C* **2009**, *113*, 4401–4405.

(15) Pumera, M. Carbon Nanotubes Contain Residual Metal Catalyst Nanoparticles Even after Washing with Nitric Acid at Elevated Temperature Because These Metal Nanoparticles Are Sheathed by Several Graphene Sheets. *Langmuir* **2007**, *23*, 6453–6458.

(16) Anik, Ü.; Çevik, S.; Pumera, M.; Anik, U.; Cevik, S.; Pumera, M. Effect of Nitric Acid "Washing" Procedure on Electrochemical Behavior of Carbon Nanotubes and Glassy Carbon μ-Particles. *Nanoscale Res. Lett.* **2010**, *5*, 846–852.

(17) Ambrosi, A.; Chee, S. Y.; Khezri, B.; Webster, R. D.; Sofer, Z.; Pumera, M. Metallic Impurities in Graphenes Prepared from Graphite Can Dramatically Influence Their Properties. *Angew. Chemie Int. Ed.* **2012**, *51*, 500–503.

(18) Ambrosi, A.; Chua, C. K.; Khezri, B.; Sofer, Z.; Webster, R. D.; Pumera, M. Chemically Reduced Graphene Contains Inherent Metallic Impurities Present in Parent Natural and Synthetic Graphite. *Proc. Natl. Acad. Sci.* **2012**, *109* , 12899–12904.

(19) Wong, C. H. A.; Sofer, Z.; Kube ova, M.; Ku era, J.; Mat jkova, S.; Pumera, M.; Kubešová, M.; Kučera, J.; Matějková, S.; Pumera, M. Synthetic Routes Contaminate Graphene Materials with a Whole Spectrum of Unanticipated Metallic Elements. *Proc. Natl. Acad. Sci.* **2014**, *111* , 13774–13779.

(20) Uk Son, S.; Kyu Park, I.; Park, J.; Hyeon, T. Synthesis of Cu2O Coated Cu Nanoparticles and Their Successful Applications to Ullmann-Type Amination Coupling Reactions of Aryl Chlorides. *Chem. Commun.* **2004**, 778–779.

(21) Zhong, H.; Fujii, K.; Nakano, Y.; Jin, F. Effect of CO 2 Bubbling into Aqueous Solutions Used for Electrochemical Reduction of CO 2 for Energy Conversion and Storage. *J. Phys. Chem. C* **2015**, *119*, 55–61.

(22) Machado, S. A. S.; Avaca, L. A. The Hydrogen Evolution Reaction on Nickel Surfaces Stabilized by H-Absorption. *Electrochim. Acta* **1994**, *39*, 1385–1391.

(23) Zou, X.; Zhang, Y. Noble Metal-Free Hydrogen Evolution Catalysts for Water Splitting. *Chem. Soc. Rev.* **2015**, *44*, 5148–5180.

(24) Hara, K.; Kudo, A.; Sakata, T. Electrochemical Reduction of Carbon Dioxide under High Pressure on Various Electrodes in an Aqueous Electrolyte. *J. Electroanal. Chem.* **1995**, *391*, 141–147.

(25) Bard, A. J. J.; Faulkner, L. R. R. *Electrochemical Methods: Fundamentals and Applications*; 2nd ed.; John Wiley: New York, 2001.

(26) Lim, D.-H.; Jo, J. H.; Shin, D. Y.; Wilcox, J.; Ham, H. C.; Nam, S. W. Carbon Dioxide Conversion into Hydrocarbon Fuels on Defective Graphene-Supported Cu Nanoparticles from First Principles. *Nanoscale* **2014**, *6*, 5087–5092.

(27) Liu, C.; He, H.; Zapol, P.; Curtiss, L. A. Computational Studies of Electrochemical CO2 Reduction on Subnanometer Transition Metal Clusters. *Phys. Chem. Chem. Phys.* **2014**, *16*, 26584–26599.

(28) Graves, C.; Ebbesen, S. D.; Mogensen, M.; Lackner, K. S. Sustainable Hydrocarbon Fuels by Recycling CO2 and H2O with Renewable or Nuclear Energy. *Renew. Sustain. Energy Rev.* **2011**, *15*, 1–23.

(29) Newman, J.; Hoertz, P. G.; Bonino, C. A.; Trainham, J. A. Review: An Economic Perspective on Liquid Solar Fuels. *J. Electrochem. Soc.* **2012**, *159*, A1722–A1729.

(30) Chen, Y.; Li, C. W.; Kanan, M. W. Aqueous CO2 Reduction at Very Low Overpotential on Oxide-Derived Au Nanoparticles. *J. Am. Chem. Soc.* **2012**, *134*, 19969–19972.

(31) Li, C. W.; Kanan, M. W. CO2 Reduction at Low Overpotential on Cu Electrodes Resulting from the Reduction of Thick Cu2O Films. *J. Am. Chem. Soc.* **2012**, *134*, 7231–7234.

(32) Li, C. W.; Ciston, J.; Kanan, M. W. Electroreduction of Carbon Monoxide to Liquid Fuel on Oxide-Derived Nanocrystalline Copper. *Nature* **2014**, *508*, 504–507.

(33) Kas, R.; Kortlever, R.; Yılmaz, H.; Koper, M. T. M.; Mul, G. Manipulating the Hydrocarbon Selectivity of Copper Nanoparticles in CO2 Electroreduction by Process Conditions. *ChemElectroChem* **2014**, *2*, 354–358.

(34) Finiels, A.; Fajula, F.; Hulea, V. Nickel-Based Solid Catalysts for Ethylene Oligomerization - a Review. *Catal. Sci. Technol.* **2014**, *4*, 2412–2426.

(35) Singh, M. R. R.; Clark, E. L. L.; Bell, A. T. T. Thermodynamic and Achievable Efficiencies for Solar-Driven Electrochemical Reduction of Carbon Dioxide to Transportation Fuels. *Proc. Natl. Acad. Sci.* **2015**, *112* , E6111–E6118.

(36) Chen, C. S.; Handoko, A. D.; Wan, J. H.; Ma, L.; Ren, D.; Yeo, B. S. Stable and Selective Electrochemical Reduction of Carbon Dioxide to Ethylene on Copper Mesocrystals. *Catal. Sci. Technol.* **2015**, *5*, 161–168.

(37) Roberts, F. S.; Kuhl, K. P.; Nilsson, A. High Selectivity for Ethylene from Carbon Dioxide Reduction over Copper Nanocube Electrocatalysts. *Angew. Chemie* **2015**, *127*, 5268–5271.

(38) Roberts, F. S.; Kuhl, K. P.; Nilsson, A. Electroreduction of Carbon Monoxide Over a Copper Nanocube Catalyst: Surface Structure and pH Dependence on Selectivity. *ChemCatChem* **2016**, 1119–1124.

(39) Liu, H.; Zhou, Y.; Kulinich, S. A.; Li, J.-J.; Han, L.-L.; Qiao, S.-Z.; Du, X.-W. Scalable Synthesis of Hollow Cu2O Nanocubes with Unique Optical Properties via a Simple Hydrolysis-Based Approach. *J. Mater. Chem. A* **2013**, *1*, 302–307.

(40) Louie, M. W.; Bell, A. T. An Investigation of Thin-Film Ni–Fe Oxide Catalysts for the Electrochemical Evolution of Oxygen. *J. Am. Chem. Soc.* **2013**, *135*, 12329–12337.

(41) Tang, W.; Peterson, A. A.; Varela, A. S.; Jovanov, Z. P.; Bech, L.; Durand, W. J.; Dahl, S.; Norskov, J. K.; Chorkendorff, I. The Importance of Surface Morphology in Controlling the Selectivity of Polycrystalline Copper for CO2 Electroreduction. *Phys. Chem. Chem. Phys.* **2012**, *14*, 76–81.

(42) Calle-Vallejo, F.; Koper, M. T. M. Theoretical Considerations on the Electroreduction of CO to C2 Species on Cu(100) Electrodes. *Angew. Chemie Int. Ed.* **2013**, *52*, 7282–7285.

(43) Ning, W.; Xia, C.; Xiaolan, C.; Yanjun, X.; Lin, G. Porous Cuprite Films: Facile Solution Deposition and Their Application for Nitrite Sensing. *Analyst* **2010**, *135*, 2106–2110.

(44) Mao, Y.; He, J.; Sun, X.; Li, W.; Lu, X.; Gan, J.; Liu, Z.; Gong, L.; Chen, J.; Liu, P.; *et al.* Electrochemical Synthesis of Hierarchical Cu2O Stars with Enhanced Photoelectrochemical Properties. *Electrochim. Acta* **2012**, *62*, 1–7.

(45) Niaura, G. Surface-Enhanced Raman Spectroscopic Observation of Two Kinds of Adsorbed OH− Ions at Copper Electrode. *Electrochim. Acta* **2000**, *45*, 3507–3519.

(46) Wang, Z.; Pischedda, V.; Saxena, S. K.; Lazor, P. X-Ray Diffraction and Raman Spectroscopic Study of Nanocrystalline CuO under Pressures. *Solid State Commun.* **2002**, *121*, 275–279.

(47) Xu, J. F.; Ji, W.; Shen, Z. X.; Li, W. S.; Tang, S. H.; Ye, X. R.; Jia, D. Z.; Xin, X. Q. Raman Spectra of CuO Nanocrystals. *J. Raman Spectrosc.* **1999**, *30*, 413–415.

(48) Feng, X.; Jiang, K.; Fan, S.; Kanan, M. W. Grain-Boundary-Dependent CO2 Electroreduction Activity. *J. Am. Chem. Soc.* **2015**, *137*, 4606–4609.

(49) Verdaguer-Casadevall, A.; Li, C. W.; Johansson, T. P.; Scott, S. B.; McKeown, J. T.; Kumar, M.; Stephens, I. E. L.; Kanan, M. W.; Chorkendorff, I. Probing the Active Surface Sites for CO Reduction on Oxide-Derived Copper Electrocatalysts. *J. Am. Chem. Soc.* **2015**, *137*, 9808–9811.

(50) Bianchi, G.; Longhi, P. Copper in Sea-Water, Potential-pH Diagrams. *Corros. Sci.* **1973**, *13*, 853–864.

(51) Lee, H. P.; Nobe, K. Kinetics and Mechanisms of Cu Electrodissolution in Chloride Media. *J. Electrochem. Soc.* **1986**, *133* , 2035–2043.

(52) Yeow, C. W.; Hibbert, D. B.; Hibbert D B. Galvanostatic Pulse Plating of Copper and Copper (I) Halides from Acid Copper (II) Halide Solutions. *J. Electrochem. Soc.* **1983**, *130* , 786–790.

(53) Cotton, F. A.; Wilkinson, G.; Murillo, C. a.; Bochmann, M. Advanced Inorganic Chemistry, 6th Edition. *Wiley-Interscience: New York*, 1999, 1–1376.

(54) Shibasaki, M.; Kanai, M. Copper(I) Fluoride and Copper(II) Fluoride. In *Encyclopedia of*

Reagents for Organic Synthesis; John Wiley & Sons, Ltd, 2001.

(55) Haendler, H. M.; Towle, L. H.; Bennett, E. F.; Patterson, W. L. The Reaction of Fluorine with Copper and Some of Its Compounds. Some Properties of Copper(II) Fluoride1. *J. Am. Chem. Soc.* **1954**, *76*, 2178–2179.

(56) Jones, J.-P.; Prakash, G. K. S.; Olah, G. A. Electrochemical CO2 Reduction: Recent Advances and Current Trends. *Isr. J. Chem.* **2014**, *54*, 1451–1466.

(57) Gattrell, M.; Gupta, N.; Co, A. A Review of the Aqueous Electrochemical Reduction of {CO2} to Hydrocarbons at Copper. *J. Electroanal. Chem.* **2006**, *594*, 1–19.

(58) Qiao, J.; Liu, Y.; Hong, F.; Zhang, J. A Review of Catalysts for the Electroreduction of Carbon Dioxide to Produce Low-Carbon Fuels. *Chem. Soc. Rev.* **2014**, *43*, 631–675.

(59) Hori, Y.; Takahashi, I.; Koga, O.; Hoshi, N. Electrochemical Reduction of Carbon Dioxide at Various Series of Copper Single Crystal Electrodes. *J. Mol. Catal. A Chem.* **2003**, *199*, 39–47.

(60) Kim, D.; Resasco, J.; Yu, Y.; Asiri, A. M.; Yang, P. Synergistic Geometric and Electronic Effects for Electrochemical Reduction of Carbon Dioxide Using Gold-Copper Bimetallic Nanoparticles. *Nat. Commun.* **2014**, *5*, 4948.

(61) Ma, M.; Djanashvili, K.; Smith, W. A. Controllable Hydrocarbon Formation from the Electrochemical Reduction of CO2 over Cu Nanowire Arrays. *Angew. Chemie Int. Ed.* **2016**, *55*, 6680–6684.

(62) Ren, D.; Deng, Y.; Handoko, A. D.; Chen, C. S.; Malkhandi, S.; Yeo, B. S. Selective Electrochemical Reduction of Carbon Dioxide to Ethylene and Ethanol on Copper(I) Oxide Catalysts. *ACS Catal.* **2015**, *5*, 2814–2821.

(63) Kas, R.; Kortlever, R.; Milbrat, A.; Koper, M. T. M.; Mul, G.; Baltrusaitis, J. Electrochemical CO2 Reduction on Cu2O-Derived Copper Nanoparticles: Controlling the Catalytic Selectivity of Hydrocarbons. *Phys. Chem. Chem. Phys.* **2014**, *16*, 12194–12201.

(64) Mistry, H.; Varela, A. S.; Bonifacio, C. S.; Zegkinoglou, I.; Sinev, I.; Choi, Y.-W.; Kisslinger, K.; Stach, E. A.; Yang, J. C.; Strasser, P.; *et al.* Highly Selective Plasma-Activated Copper Catalysts for Carbon Dioxide Reduction to Ethylene. *Nat. Commun.* **2016**, *7*, 12123.

(65) Raciti, D.; Livi, K. J.; Wang, C. Highly Dense Cu Nanowires for Low-Overpotential CO2 Reduction. *Nano Lett.* **2015**, *15*, 6829–6835.

(66) Schreier, M.; Curvat, L.; Giordano, F.; Steier, L.; Abate, A.; Zakeeruddin, S. M.; Luo, J.; Mayer, M. T.; Grätzel, M. Efficient Photosynthesis of Carbon Monoxide from CO_2 Using Perovskite Photovoltaics. *Nat. Commun.* **2015**, *6*, 7326.

(67) Hsieh, Y.-C.; Senanayake, S. D.; Zhang, Y.; Xu, W.; Polyansky, D. E. Effect of Chloride Anions on the Synthesis and Enhanced Catalytic Activity of Silver Nanocoral Electrodes for CO_2 Electroreduction. *ACS Catal.* **2015**, *5*, 5349–5356.

(68) Koh, J. H.; Jeon, H. S.; Jee, M. S.; Nursanto, E. B.; Lee, H.; Hwang, Y. J.; Min, B. K. Oxygen Plasma Induced Hierarchically Structured Gold Electrocatalyst for Selective Reduction of Carbon Dioxide to Carbon Monoxide. *J. Phys. Chem. C* **2015**, *119*, 883–889.

(69) Jee, M. S.; Jeon, H. S.; Kim, C.; Lee, H.; Koh, J. H.; Cho, J.; Min, B. K.; Hwang, Y. J. Enhancement in Carbon Dioxide Activity and Stability on Nanostructured Silver Electrode and the Role of Oxygen. *Appl. Catal. B Environ.* **2016**, *180*, 372–378.

(70) Lobaccaro, P.; Singh, M. R.; Clark, E. L.; Kwon, Y.; Bell, A. T.; Ager, J. W. Effects of Temperature and Gas-Liquid Mass Transfer on the Operation of Small Electrochemical Cells for the Quantitative Evaluation of CO2 Reduction Electrocatalysts. *Phys. Chem. Chem. Phys.* **2016**, *18*, 26777–26785.

(71) Singh, M. R.; Kwon, Y.; Lum, Y.; Ager, J. W.; Bell, A. T. Hydrolysis of Electrolyte Cations Enhances the Electrochemical Reduction of CO2 over Ag and Cu. *J. Am. Chem. Soc.* **2016**, *138*, 13006–13012.

(72) Thorson, M. R.; Siil, K. I.; Kenis, P. J. a. Effect of Cations on the Electrochemical Conversion of CO2 to CO. *J. Electrochem. Soc.* **2013**, *160*, F69–F74.

(73) Murata, A.; Hori, Y. *Product Selectivity Affected by Cationic Species in Electrochemical Reduction of CO2 and CO at a Cu Electrode.*; 1991; Vol. 64, pp. 123–127.

(74) Hori, Y.; Suzuki, S. Electrolytic Reduction of Carbon Dioxide at Mercury Electrode in Aqueous Solutions. *Bulletin of the Chemical Society of Japan*, 1982, *55*, 660–665.

(75) Pocker, Y.; Bjorkquist, D. W. Stopped-Flow Studies of Carbon Dioxide Hydration and Bicarbonate Dehydration in Water and Water-d2. Acid-Base and Metal Ion Catalysis. *J. Am. Chem. Soc.* **1977**, *99*, 6537–6543.

(76) Dutta, A.; Rahaman, M.; Luedi, N. C.; Mohos, M.; Broekmann, P. Morphology Matters: Tuning the Product Distribution of CO2 Electroreduction on Oxide-Derived Cu Foam Catalysts. *ACS Catal.* **2016**, *6*, 3804–3814.

(77) Schouten, K. J. P.; Kwon, Y.; van der Ham, C. J. M.; Qin, Z.; Koper, M. T. M. A New Mechanism for the Selectivity to C1 and C2 Species in the Electrochemical Reduction of Carbon Dioxide on Copper Electrodes. *Chem. Sci.* **2011**, *2*, 1902.

(78) Hori, Y.; Wakebe, H.; Tsukamoto, T.; Koga, O. Adsorption of CO Accompanied with Simultaneous Charge Transfer on Copper Single Crystal Electrodes Related with Electrochemical Reduction of CO2 to Hydrocarbons. *Surf. Sci.* **1995**, *335*, 258–263.

(79) Feng, X.; Jiang, K.; Fan, S.; Kanan, M. W. A Direct Grain-Boundary-Activity Correlation for CO Electroreduction on Cu Nanoparticles. *ACS Cent. Sci.* **2016**, *2*, 169–174.

(80) Handoko, A. D.; Ong, C. W.; Huang, Y.; Lee, Z. G.; Lin, L.; Panetti, G. B.; Yeo, B. S. Mechanistic Insights into the Selective Electroreduction of Carbon Dioxide to Ethylene on Cu2O-Derived Copper Catalysts. *J. Phys. Chem. C* **2016**, *120*, 20058–20067.

(81) Singh, M. R.; Clark, E. L.; Bell, A. T. Effects of Electrolyte, Catalyst, and Membrane

Composition and Operating Conditions on the Performance of Solar-Driven Electrochemical Reduction of Carbon Dioxide. *Phys. Chem. Chem. Phys.* **2015**, *17*, 18924–18936.

(82) Schouten, K. J. P.; Qin, Z.; Gallent, E. P.; Koper, M. T. M. Two Pathways for the Formation of Ethylene in CO Reduction on Single-Crystal Copper Electrodes. *J. Am. Chem. Soc.* **2012**, *134*, 9864–9867.

(83) Schouten, K. J. P.; Pérez Gallent, E.; Koper, M. T. M. The Influence of pH on the Reduction of CO and to Hydrocarbons on Copper Electrodes. *J. Electroanal. Chem.* **2014**, *716*, 53–57.

(84) Goodpaster, J. D.; Bell, A. T.; Head-Gordon, M. Identification of Possible Pathways for C–C Bond Formation during Electrochemical Reduction of CO2: New Theoretical Insights from an Improved Electrochemical Model. *J. Phys. Chem. Lett.* **2016**, *7*, 1471–1477.

(85) Xiao, H.; Cheng, T.; Goddard, W. A.; Sundararaman, R. Mechanistic Explanation of the pH Dependence and Onset Potentials for Hydrocarbon Products from Electrochemical Reduction of CO on Cu (111). *J. Am. Chem. Soc.* **2016**, *138*, 483–486.

(86) Gupta, N.; Gattrell, M.; MacDougall, B. Calculation for the Cathode Surface Concentrations in the Electrochemical Reduction of CO2 in KHCO3 Solutions. *J. Appl. Electrochem.* **2006**, *36*, 161–172.

(87) Lum, Y.; Yue, B.; Lobaccaro, P.; Bell, A. T.; Ager, J. W. Optimizing C-C Coupling on Oxide-Derived Copper Catalysts for Electrochemical CO 2 Reduction. *J. Phys. Chem. C* **2017**, *121*, 14191–14203.

(88) Gao, D.; Zegkinoglou, I.; Divins, N. J.; Scholten, F.; Sinev, I.; Grosse, P.; Roldan Cuenya, B. Plasma-Activated Copper Nanocube Catalysts for Efficient Carbon Dioxide Electroreduction to Hydrocarbons and Alcohols. *ACS Nano* **2017**, *11*, 4825–4831.

(89) Mistry, H.; Varela, A. S. A. S.; Bonifacio, C. S. C. S.; Zegkinoglou, I.; Sinev, I.; Choi, Y.-W. Y.-W.; Kisslinger, K.; Stach, E. A. E. A.; Yang, J. C. J. C.; Strasser, P.; *et al.* Highly Selective Plasma-Activated Copper Catalysts for Carbon Dioxide Reduction to Ethylene. *Nat. Commun.* **2016**, *7*, 12123.

(90) Lee, S.; Kim, D.; Lee, J. Electrocatalytic Production of C3-C4 Compounds by Conversion of CO2 on a Chloride-Induced Bi-Phasic Cu2O-Cu Catalyst. *Angew. Chemie* **2015**, *127*, 14914–14918.

(91) Lee, C. H.; Kanan, M. W. Controlling H+ vs CO2 Reduction Selectivity on Pb Electrodes. *ACS Catal.* **2015**, *5*, 465–469.

(92) Eilert, A.; Cavalca, F.; Roberts, F. S.; Osterwalder, J.; Liu, C.; Favaro, M.; Crumlin, E. J.; Ogasawara, H.; Friebel, D.; Pettersson, L. G. M.; *et al.* Subsurface Oxygen in Oxide-Derived Copper Electrocatalysts for Carbon Dioxide Reduction. *J. Phys. Chem. Lett.* **2017**, *8*, 285–290.

(93) Favaro, M.; Xiao, H.; Cheng, T.; Goddard, W. A.; Yano, J.; Crumlin, E. J. Subsurface Oxide Plays a Critical Role in CO_2 Activation by Cu(111) Surfaces to Form Chemisorbed CO_2,

the First Step in Reduction of CO_2. *Proc. Natl. Acad. Sci. U. S. A.* **2017**, *114*, 6706–6711.

(94) Xiao, H.; Goddard, W. A.; Cheng, T.; Liu, Y. Cu Metal Embedded in Oxidized Matrix Catalyst to Promote CO 2 Activation and CO Dimerization for Electrochemical Reduction of CO 2. *Proc. Natl. Acad. Sci.* **2017**, 201702405.

(95) Platzman, I.; Brener, R.; Haick, H.; Tannenbaum, R. Oxidation of Polycrystalline Copper Thin Films at Ambient Conditions. *J. Phys. Chem. C* **2008**, *112*, 1101–1108.

(96) Xu, L.; Yang, Y.; Hu, Z.-W.; Yu, S.-H. Comparison Study on the Stability of Copper Nanowires and Their Oxidation Kinetics in Gas and Liquid. *ACS Nano* **2016**, *10*, 3823–3834.

(97) Matsnnaga, S.; Homma, T. Influence on the Oxidation Kinetics of Metals by Control of the Structure of Oxide Scales. *Oxid. Met.* **1976**, *10*, 361–376.

(98) Gattinoni, C.; Michaelides, A. Atomistic Details of Oxide Surfaces and Surface Oxidation: The Example of Copper and Its Oxides. *Surf. Sci. Rep.* **2015**, *70*, 424–447.

(99) Fujita, K.; Ando, D.; Uchikoshi, M.; Mimura, K.; Isshiki, M. New Model for Low-Temperature Oxidation of Copper Single Crystal. *Appl. Surf. Sci.* **2013**, *276*, 347–358.

(100) Zhu, Q.; Zou, L.; Zhou, G.; Saidi, W. A.; Yang, J. C. Early and Transient Stages of Cu Oxidation: Atomistic Insights from Theoretical Simulations and in Situ Experiments. *Surf. Sci.* **2016**, *652*, 98–113.

(101) Paul, A.; Laurila, T.; Vuorinen, V.; Divinski, S. V. Short-Circuit Diffusion - Thermodynamics, Diffusion and the Kirkendall Effect in Solids. In; Paul, A.; Laurila, T.; Vuorinen, V.; Divinski, S. V, Eds.; Springer International Publishing: Cham, 2014; pp. 429–491.

(102) Lum, Y.; Yue, B.; Lobaccaro, P.; Bell, A. T.; Ager, J. W. Optimizing C–C Coupling on Oxide-Derived Copper Catalysts for Electrochemical CO2 Reduction. *J. Phys. Chem. C* **2017**, *121*, 14191–14203.

(103) Goeppert, A.; Czaun, M.; Jones, J.-P.; Surya Prakash, G. K.; Olah, G. A. Recycling of Carbon Dioxide to Methanol and Derived Products – Closing the Loop. *Chem. Soc. Rev.* **2014**, *43*, 7995–8048.

(104) Kim, D.; Sakimoto, K. K.; Hong, D.; Yang, P. Artificial Photosynthesis for Sustainable Fuel and Chemical Production. *Angew. Chemie Int. Ed.* **2015**, *54*, 3259–3266.

(105) Chu, S.; Cui, Y.; Liu, N. The Path towards Sustainable Energy. *Nat Mater* **2017**, *16*, 16–22.

(106) Montoya, J. H. H.; Seitz, L. C. C.; Chakthranont, P.; Vojvodic, A.; Jaramillo, T. F. F.; Norskov, J. K.; Nørskov, J. K. Materials for Solar Fuels and Chemicals. *Nat Mater* **2017**, *16*, 70–81.

(107) Lu, Q.; Rosen, J.; Jiao, F. Nanostructured Metallic Electrocatalysts for Carbon Dioxide Reduction. *ChemCatChem* **2015**, *7*, 38–47.

(108) Mistry, H.; Varela, A. S.; Kühl, S.; Strasser, P.; Cuenya, B. R. Nanostructured Electrocatalysts with Tunable Activity and Selectivity. *Nat. Rev. Mater.* **2016**, *1*, 16009.

(109) Kumar, B.; Brian, J. P.; Atla, V.; Kumari, S.; Bertram, K. A.; White, R. T.; Spurgeon, J. M. New Trends in the Development of Heterogeneous Catalysts for Electrochemical CO2 Reduction. *Catal. Today* **2016**, *270*, 19–30.

(110) Zhu, D. D.; Liu, J. L.; Qiao, S. Z. Recent Advances in Inorganic Heterogeneous Electrocatalysts for Reduction of Carbon Dioxide. *Adv. Mater.* **2016**, *28*, 3423–3452.

(111) Yang, K. D.; Lee, C. W.; Jin, K.; Im, S. W.; Nam, K. T. Current Status and Bioinspired Perspective of Electrochemical Conversion of CO 2 to a Long-Chain Hydrocarbon. *J. Phys. Chem. Lett.* **2017**, *8*, 538–545.

(112) Khezri, B.; Fisher, A. C.; Pumera, M. CO 2 Reduction: The Quest for Electrocatalytic Materials. *J. Mater. Chem. A* **2017**, *5*, 8230–8246.

(113) Larrazábal, G. O.; Martín, A. J.; Pérez-Ramírez, J. Building Blocks for High Performance in Electrocatalytic CO 2 Reduction: Materials, Optimization Strategies, and Device Engineering. *J. Phys. Chem. Lett.* **2017**, *8*, 3933–3944.

(114) Hori, Y.; Takahashi, R.; Yoshinami, Y.; Murata, A. Electrochemical Reduction of CO at a Copper Electrode. *J. Phys. Chem. B* **1997**, *101*, 7075–7081.

(115) Nie, X.; Esopi, M. R.; Janik, M. J.; Asthagiri, A. Selectivity of CO2 Reduction on Copper Electrodes: The Role of the Kinetics of Elementary Steps. *Angew. Chemie Int. Ed.* **2013**, *52*, 2459–2462.

(116) Cheng, T.; Xiao, H.; Goddard, W. A. Free-Energy Barriers and Reaction Mechanisms for the Electrochemical Reduction of CO on the Cu(100) Surface, Including Multiple Layers of Explicit Solvent at pH 0. *J. Phys. Chem. Lett.* **2015**, *6*, 4767–4773.

(117) Xiao, H.; Cheng, T.; Goddard, W. A. Atomistic Mechanisms Underlying Selectivities in C 1 and C 2 Products from Electrochemical Reduction of CO on Cu(111). *J. Am. Chem. Soc.* **2017**, *139*, 130–136.

(118) Luo, W.; Nie, X.; Janik, M. J.; Asthagiri, A. Facet Dependence of CO2 Reduction Paths on Cu Electrodes. *ACS Catal.* **2016**, *6*, 219–229.

(119) Cheng, T.; Xiao, H.; Goddard, W. A. Full Atomistic Reaction Mechanism with Kinetics for CO Reduction on Cu(100) from Ab Initio Molecular Dynamics Free-Energy Calculations at 298 K. *Proc. Natl. Acad. Sci.* **2017**, *114* , 1795–1800.

(120) Huff, C. A.; Sanford, M. S. Cascade Catalysis for the Homogeneous Hydrogenation of CO 2 to Methanol. *J. Am. Chem. Soc.* **2011**, *133*, 18122–18125.

(121) Wang, X.; Li, Z.; Shi, J.; Wu, H.; Jiang, Z.; Zhang, W.; Song, X.; Ai, Q. Bioinspired Approach to Multienzyme Cascade System Construction for Efficient Carbon Dioxide Reduction. *ACS Catal.* **2014**, *4*, 962–972.

(122) Ren, D.; Ang, B. S.-H.; Yeo, B. S. Tuning the Selectivity of Carbon Dioxide Electroreduction toward Ethanol on Oxide-Derived CuxZn Catalysts. *ACS Catal.* **2016**, *6*, 8239–8247.

(123) Wheeldon, I.; Minteer, S. D.; Banta, S.; Barton, S. C.; Atanassov, P.; Sigman, M. Substrate Channelling as an Approach to Cascade Reactions. *Nat. Chem.* **2016**, *8*, 299–309.

(124) Esposito, D. V. V; Levin, I.; Moffat, T. P. P.; Talin, A. A. A. H2 Evolution at Si-Based Metal-Insulator-Semiconductor Photoelectrodes Enhanced by Inversion Channel Charge Collection and H Spillover. *Nat. Mater.* **2013**, *12*, 562–568.

(125) Grunes, J.; Zhu, J.; Anderson, E. A.; Somorjai, G. A. Ethylene Hydrogenation over Platinum Nanoparticle Array Model Catalysts Fabricated by Electron Beam Lithography: Determination of Active Metal Surface Area. *J. Phys. Chem. B* **2002**, *106*, 11463–11468.

(126) Wickman, B. B.; Seidel, Y. E.; Jusys, Z.; Kasemo, B.; Behm, R. J. J. Fabrication of Pt/Ru Nanoparticle Pair Arrays with Controlled Separation and Their Electrocatalytic Properties. *ACS Nano* **2011**, *5*, 2547–2558.

(127) Koper, M. T. M.; Lukkien, J. J.; Jansen, A. P. J.; van Santen, R. A. Lattice Gas Model for CO Electrooxidation on Pt−Ru Bimetallic Surfaces. *J. Phys. Chem. B* **1999**, *103*, 5522–5529.

(128) Koper, M. T. M.; Jansen, a. P. J.; van Santen, R. a.; Lukkien, J. J.; Hilbers, P. a. J. Monte Carlo Simulations of a Simple Model for the Electrocatalytic CO Oxidation on Platinum. *J. Chem. Phys.* **1998**, *109*, 6051–6062.

(129) Korzeniewski, C.; Kardash, D. Use of a Dynamic Monte Carlo Simulation in the Study of Nucleation-and-Growth Models for CO Electrochemical Oxidation. *J. Phys. Chem. B* **2001**, *105*, 8663–8671.

(130) Ionita, P.; Volkov, A.; Jeschke, G.; Chechik, V. Lateral Diffusion of Thiol Ligands on the Surface of Au Nanoparticles: An Electron Paramagnetic Resonance Study. *Anal. Chem.* **2008**, *80*, 95–106.

(131) Das, R. K.; Wang, Y.; Vasilyeva, S. V; Donoghue, E.; Pucher, I.; Kamenov, G.; Cheng, H.-P.; Rinzler, A. G. Extraordinary Hydrogen Evolution and Oxidation Reaction Activity from Carbon Nanotubes and Graphitic Carbons. *ACS Nano* **2014**, *8*, 8447–8456.

(132) Herranz, J.; Garsuch, A.; Gasteiger, H. A. Using Rotating Ring Disc Electrode Voltammetry to Quantify the Superoxide Radical Stability of Aprotic Li-Air Battery Electrolytes. *J. Phys. Chem. C* **2012**, *116*, 19084–19094.

(133) Sankarasubramanian, S.; Seo, J.; Mizuno, F.; Singh, N.; Prakash, J. Rotating Ring-Disc Electrode Investigation of the Aprotic Superoxide Radical Electrochemistry on Multi-Crystalline Surfaces and Correlation with Density Functional Theory Modeling: Implications for Lithium-Air Cells. *J. Electrochem. Soc.* **2016**, *163*, A2377–A2384.

(134) Niwa, O. Electroanalysis with Interdigitated Array Microelectrodes. *Electroanalysis*, 1995, *7*, 606–613.

(135) Ojima, H.; Umedal, M.; Mohamedi, M.; Uchida, I. Electrochemical Detection of Protons Produced in an Electrode Reaction Using Interdigitated Microarray Electrodes. *Electroanalysis* **2003**, *15*, 1677–1681.

(136) Sakuma, G.; Fukunaka, Y.; Matsushima, H. Nucleation and Growth of Electrolytic Gas Bubbles under Microgravity. *Int. J. Hydrogen Energy* **2014**, *39*, 7638–7645.

(137) Jones, S. Bubble Nucleation from Gas Cavities — a Review. *Adv. Colloid Interface Sci.* **1999**, *80*, 27–50.

(138) Fernández, D.; Maurer, P.; Martine, M.; Coey, J. M. D.; Möbius, M. E. Bubble Formation at a Gas-Evolving Microelectrode. *Langmuir* **2014**, *30*, 13065–13074.

(139) Kadyk, T.; Bruce, D.; Eikerling, M. How to Enhance Gas Removal from Porous Electrodes? *Sci. Rep.* **2016**, *6*, 38780.

(140) Brussieux, C.; Viers, P.; Roustan, H.; Rakib, M. Controlled Electrochemical Gas Bubble Release from Electrodes Entirely and Partially Covered with Hydrophobic Materials. *Electrochim. Acta* **2011**, *56*, 7194–7201.

(141) Akhade, S. A.; Luo, W.; Nie, X.; Bernstein, N. J.; Asthagiri, A.; Janik, M. J. Poisoning Effect of Adsorbed CO during CO2 Electroreduction on Late Transition Metals. *Phys. Chem. Chem. Phys.* **2014**, *16*, 20429–20435.

(142) Sandberg, R. B.; Montoya, J. H.; Chan, K.; Nørskov, J. K. CO-CO Coupling on Cu Facets: Coverage, Strain and Field Effects. *Surf. Sci.* **2016**, *654*, 56–62.

(143) Huang, Y.; Handoko, A. D.; Hirunsit, P.; Yeo, B. S. Electrochemical Reduction of CO2 Using Copper Single-Crystal Surfaces: Effects of CO* Coverage on the Selective Formation of Ethylene. *ACS Catal.* **2017**, *7*, 1749–1756.

(144) Shi, C.; Hansen, H. A.; Lausche, A. C.; Norskov, J. K. Trends in Electrochemical CO2 Reduction Activity for Open and Close-Packed Metal Surfaces. *Phys. Chem. Chem. Phys.* **2014**, *16*, 4720–4727.

(145) Lu, Q.; Rosen, J.; Zhou, Y.; Hutchings, G. S.; Kimmel, Y. C.; Chen, J. G.; Jiao, F. A Selective and Efficient Electrocatalyst for Carbon Dioxide Reduction. *Nat. Commun.* **2014**, *5*, 3242.

(146) Ma, S.; Sadakiyo, M.; Luo, R.; Heima, M.; Yamauchi, M.; Kenis, P. J. A. One-Step Electrosynthesis of Ethylene and Ethanol from CO2in an Alkaline Electrolyzer. *J. Power Sources* **2016**, *301*, 219–228.

(147) Pérez-Gallent, E.; Marcandalli, G.; Figueiredo, M. C.; Calle-Vallejo, F.; Koper, M. T. M. Structure- and Potential-Dependent Cation Effects on CO Reduction at Copper Single-Crystal Electrodes. *J. Am. Chem. Soc.* **2017**, *139*, 16412–16419.

(148) Resasco, J.; Chen, L. D.; Clark, E.; Tsai, C.; Hahn, C.; Jaramillo, T. F.; Chan, K.; Bell, A. T. Promoter Effects of Alkali Metal Cations on the Electrochemical Reduction of Carbon Dioxide. *J. Am. Chem. Soc.* **2017**, *139*, 11277–11287.

(149) Resasco, J.; Lum, Y.; Clark, E.; Zeledon, J.; Bell, A. T. Effects of Anion Identity and Concentration on Electrochemical Reduction of CO2. *ChemElectroChem* n/a – n/a.

(150) Peterson, A. A.; Abild-Pedersen, F.; Studt, F.; Rossmeisl, J.; Nørskov, J. K.; Norskov, J. K. How Copper Catalyzes the Electroreduction of Carbon Dioxide into Hydrocarbon Fuels. *Energy Environ. Sci.* **2010**, *3*, 1311–1315.

(151) Pérez-Gallent, E.; Figueiredo, M. C.; Calle-Vallejo, F.; Koper, M. T. M. Spectroscopic Observation of a Hydrogenated CO Dimer Intermediate During CO Reduction on Cu(100) Electrodes. *Angew. Chemie - Int. Ed.* **2017**, *56*, 3621–3624.

(152) Garza, A. J.; Bell, A. T.; Head-Gordon, M. Mechanism of CO2 Reduction at Copper Surfaces: Pathways to C2 Products. *ACS Catal.* **2018**, *8*, 1490–1499.